DESIGN STUDY FOR A 250 MeV HIGH CURRENT CYCLOTRON

H. BLOSSER, D.A. JOHNSON, and F. MARTI

NSCL, MSU

Sept. 1996

Lockheed Martin Energy Systems
Subcontract 22X-SW033V

Table of Contents

DESIGN STUDY FOR A 250 MeV HIGH CURRENT CYCLOTRON

I. INTRODUCTION

The Hollifield Radioactive Ion Beam Facility (HRIBF) at Oak Ridge National Laboratory wishes to replace their present primary production (or "driver") cyclotron, ORIC with a 250 MeV cyclotron designed to produce beams of protons in the 100 to 200 microamp range. A number of accelerator configurations can be immediately posed as candidate systems to meet this functional specification; several of these fail to satisfy an additional characteristic desired by HRIBF, namely that the accelerator fit in Room C110 of the existing HRIBF building. A partial, somewhat arbitrary, list of likely accelerator configurations includes:

1) a Compact Superconducting Cyclotron (CSC) based on a 1993 MSU/NSCL study (MSUCL-874) of a 250 MeV cyclotron for medical use, with modifications to increase the beam current to the 100 to 200 microamp level.

2) an enlarged, lower field version of the MSUCL-874 accelerator system with the magnet excited by a Room Temperature main Coil (RTC) operating at a dissipation level of roughly 500 kilowatts.

3) a Separated Sector Cyclotron (SSC) similar to the 200 MeV cyclotron at the South African National Accelerator Center but with the field increased so that the accelerator will fit into room C110.

4) a Negative-Ion Cyclotron (NIC) similar to the central part of the 500 MeV cyclotron at the Triumf Laboratory in Vancouver, Canada but reduced in radius to give the desired maximum energy of 250 MeV and with the magnetic field in the hills of the magnetic increased to a higher value than used at Triumf as allowed by the reduced electric dissociation of the H^- ion at 250 MeV vs 500 MeV.

5) a room temperature linac (RTL) similar to the first stage of the LAMPF accelerator at Los Alamos or to the injector linac at FermiLab or at other large synchrotrons.

6) a superconducting linac (SCL) similar to structures under study at Los Alamos for use in a high current Linac system for the production of Tritium.

The last two of these options (the RTL and the SCL) seem clearly incompatible with the goal of fitting room C110, while the NIC and SSC options can be made to fit the room if the magnetic field details are pressed somewhat beyond the choices made in previous projects of this type. The CSC option involves a large step relative to the beam current regime in which cyclotrons of this type presently operate but is lowest in cost and fits room C110 with very comfortable margins. The SSC option in contrast is comfortably within

the established operating range of existing separated sector cyclotrons for both energy and intensity (although not actually identical to any of the existing SSC's) but is considerably more expensive (x4) and much more difficult to fit into room C110 (and the required injector cyclotron must be placed in an adjacent room). The RTC option is from one perspective an additional data point in a parameter search to establish the optimum magnetic field for a compact type cyclotron for the HRIBF application, with the additional optional feature of omitting the liquid helium system to gain operating simplicity.

The 250 MeV CSC option is somewhat higher in particle velocity than the 200 MeV/A, Q/A=0.5 operating range of the MSU K1200 or the 200 MeV, Q/A=1 design goal of the AGOR cyclotron; the shift in energy from 200 to 250 MeV requires a change from 3 to 4 sectors in the basic magnet symmetry but this is a detail of relatively minor significance, 4 sectors being viewed as an advantage by many, and especially by the group at Chalk River where a 4 sector K510 superconducting cyclotron has operated in the 50 MeV/A range since 1985. As noted above, the 200 microamp current and 50 kw beam power in a compact, high-field cyclotron are performance goals involving a large extrapolation from achieved operating values in superconducting cyclotrons; the MSU K1200 is being upgraded to achieve beam currents of 1 particle microamp at power levels of 4 kw, and operating tests of critical components indicate this to be a realistic goal -- the medical cyclotron at Harper Hospital accelerates 200 microamp beams of 50 MeV deuterons on a regular basis but at a reduced duty cycle so that average beam power is only 750 w and the internal target design means that no extraction system is involved. The previous cyclotron which most parallels the beam current requirement of the driver cyclotron project is in fact the room temperature cyclotron designed and constructed by the Philips Company as the original injector (the "Philips injector") for the PSI ring cyclotron. This cyclotron operated at 72 MeV in its injector mode and achieved currents of 215 microamps internal and 200 microamps external, i.e. an extracted beam power of 14 kilowatts and extraction efficiency of 93%. The CSC option which we present here then follows the philosophy of the PSI Phillips injector in that a multi-turn extraction system is used which allows the rf accelerating system to run at relatively low voltage -- carefully centered internal orbits and optimized precessional extraction will bring extraction losses to the 5 to 10% level, thereby bringing the radioactivity induced in the cyclotron to a level compatible with relatively simple remote handling devices (as discussed further in following sections).

The SSC option as noted above is much closer to the regime of presently operating cyclotrons than the the CSC machine but more expensive by approximately a factor of four, and with some difficulty relative to the requirement of fitting room C110. Comparing the HRIBF driver cyclotron design goals to achieved performance at existing cyclotrons, we note:

a) the fixed magnetic field "meson factory" cyclotrons at PSI and at Triumf operate at higher energy and higher or comparable current (1600 microamps at 590 MeV at PSI and 180 micropamps at 520 MeV at Triumf) and

b) the South African variable-energy SSC at Faure has accelerated protons to 220 MeV and at 66 MeV has achieved beam currents of 200 microamps (13.2 kw of external beam power).

The performance characteristics of the South African cyclotron closely match the HRIBF driver cyclotron goals, but there is a size incompatibility relative to the requirement of fitting room C110 -- an SSC to fit room C110 must then

be a modified version of the South African design using a higher magnetic field and a fixed frequency rf system to reduce the size of the main cyclotron -- space must also be provided in an adjacent (perhaps less heavily shielded) room to house the required injector cyclotron.

The strict time constraints set up by the present HRIBF study (sub-contract 22X-SW033V) require that a report be submitted at this time even though the work under the study is in an incomplete state. This report fulfills the formal requirements of the sub-contract in that it provides all information specifically required by the sub-contract, but, in a scientific sense, is a progress report, with many important elements of a fully developed study in an incomplete state at this time.

The primary accomplishments of the study thus far are 1) development of an SSC structure to fit Room C110 and 2) a computer study of the distribution of the radioactivity which will will be induced in a CSC structure by beam losses in the extraction process. The later work has involved development of a new computer code "SEPPEN" for the study of orbits which penetrate the septum of the extraction system electrostatic deflector. This work is leading to new insights into the details of beam losses in electrostatic deflectors, which should then lead to better optimized designs and predictable extraction losses in any cyclotron operating in the multi-turn extraction mode.

The present report mainly focuses on the CSC component of the HRIBF study since this option, because of the earlier NSCL study of such an accelerator for a cancer therapy application, has been able to be developed in considerably more detail at this point in time, particularly in the cost estimate area. (The CSC option has a strong advantage in being much less costly than any of the other accelerator options listed at the beginning, and the cost estimate is much more fully developed, the later being one of the major study endpoints stipulated by HRIBF in the study subcontract.)

Section II of this report briefly reviews the major technical features of the CSC structure as developed in MSUCL-874 and checks space charge limits to confirm beam current capability. Section III describes the orbit analysis procedure which has been selected/developed to analyze deflector performance. Section IV presents results of a first study of a trial deflector calculation with this procedure. Section V describes the steps which will be taken in future studies to fully optimize the extraction efficiency of the CSC structure in the multi-turn mode, and to improve the accuracy of the induced radioactivity calculations by including the effect of scattering in the septum. Section VI gives a basic overview of the SSC cyclotron developed in the present study and shows how either the CSC or the SSC cyclotrons might be located in Room C110. (A more complete account of results from the SSC study will be presented in a later separate report.) Section VII gives an analysis of the estimated cost the CSC system, and a preliminary comparative figure for the SSC system. Finally, Section VIII gives concluding summary comments and suggestions as to possible further development of the design concept for the future HRIBF driver accelerator.

II. PRIMARY FEATURES OF THE COMPACT SUPERCONDUCTING CYCLOTRON

The basic cyclotron structure developed in the 1993 study was well optimized and therefore provides a significantly advanced starting point for

the present study. In view of the extensive references to the MSUCL-874 study, Sections III & V of that report are attached to this report as an Appendix and references to Figures/Tables in that Appendix are made with an "A" inserted in the Figure number, viz. Fig. A-III.4, Table A-V.1, etc.

The main features of the CSC cyclotron are shown first of all in Figure II.1 which gives a perspective view of the cyclotron with the upper magnet cap raised to the "open" position used for maintenance; the Figure shows 1) a "pillbox" magnet 122" in diameter and 65" high, 2) a pair of intrinsically stable, wet-wound superconducting coils of 5"x4" cross section and 72" inner diameter, and 3) a 4 sector, dee-in-valley accelerating system. Figures A-III.1 and A-III.2 in the Appendix show these features in more detail giving respectively, a vertical section view and a median-plane, plan view of the proposed cyclotron. The calculated field of this magnet is shown in Figure A-III.4 and gives excellent equilibrium orbit characteristics as shown in Figure A-III.5.

As noted in a previous paragraph, the major specification change from the MSUCL-874 proton therapy cyclotron to the HRIBF driver cyclotron is in the desired beam current which is higher by a factor of 10,000 for the latter device. The desired current for the driver cyclotron is in fact much closer to the normal operating regime of proton cyclotrons and so does not present a difficulty on the scale of that inferred by simply noting the 10E4 factor relative to the proton therapy current. (An issue of some contention in reviews of the proton therapy project was in fact whether the systems provided for reducing beam current to the proton therapy value were sufficiently reliable to insure that patients would not be injured by sudden bursts of higher current.) Acknowledging the lack of relevance of the design beam current for the proton therapy project, the 200 microamp HRIBF beam specification is never-the-less the clear major technical advance involved in the CSC approach, requiring operation in a design regime not previously achieved in superconducting cyclotron external beams, and constituting therefore an aspect of the suggested system which must be quite carefully assessed.

A. Ion Source Output

The first issue to consider relative to the desired 200 microamp beam current is whether the internal ion source assumed in the design (see Figure A-III.8) has adequate output. This question can however be immediately affirmed on experimental grounds, since the ion source assumed in the proton study is a copy of the source used in the neutron therapy cyclotron in Detroit and this source regularly produces beams at the 200 microamp level. (The source operates CW even though the cyclotron rf is pulsed to reduce required electric power).

B. Beam Space Charge Limits

The effect of space charge forces on the accelerated beam are a next point of concern. There is first of all the axial space charge limit which is present in all cyclotrons -- in the approximation of fully overlapping turns this limit is set by the charge density in the accelerated beam (determined by the current, the energy gain per turn, the phase width and the height of the beam) relative to the strength of the axial restoring force (the strength of the magnetic axial force is indicated by the "NU Z" plot in Figure A-III.5 -- near the center this is augmented by electrical forces as shown in Figure A-III.7). Inferring a minimum Nu Z of 0.2 from Figures A-III.5 & A-III.7, using

500 keV/turn for the anticipated energy gain, +/- 10 degrees as the anticipated phase width, and +/- 2.5mm as the beam height and using the space charge limit for a smooth distribution of charge namely:

$$i_{lim} = \Delta z \nu_z^2 \omega_o \epsilon_o \frac{\Delta\Phi}{2\pi} \Delta V$$

gives a resulting value for the axial space charge limit of 11 milliamps i.e. very much higher than the current goal for the HRIBF driver accelerator. (The operation of the Detroit medical cyclotron is also a clear experimental confirmation of the adequacy of the basic cyclotron structure considered here with respect to axial space charge forces.)

Another beam current limit, the traditional limiting issue in "single-turn-extraction" cyclotrons, arises from the "longitudinal" space charge force which gives extra acceleration to particles at the leading edge of the beam pulse relative to particles at the trailing edge. This force then increases the energy spread associated with a particular turn so that the radial separation of turns disappears and 100% (or "single-turn") extraction can no longer be achieved. This single-turn extraction requirement is then typically a design dominating limit; in the situation of the CSC driver cyclotron this condition sets requirements (energy gain of about 1 MeV per turn and a flat-topping system to accept the broad phase width) which are incompatible with the overall small size of the accelerator. The alternative "multi-turn" extraction concept -- the approach used with great effectiveness in the PSI Philips injector -- is then the necessary choice for the CSC driver. This selection eliminates the turn separation requirement which obviates the relevance of the longitudinal space charge effect. For the CSC option multi-turn extraction is then the clear solution of choice to obtain 200 microamps of beam at 250 MeV.

Noting the above points, work on the CSC option for this study focuses on the behavior of the cyclotron when it is used in a broad-phase, multi-turn extraction mode. As noted above, this approach to the design of a high current cyclotron was pioneered by the Philips Corporation in the design and construction of the first PSI injector cyclotron. The design energy of this cyclotron was 72 MeV and it operated at currents up to 200 microamps with extraction efficiencies of up to 93% (Stambach 84). With this choice, extraction efficiency of course remains a central key characteristic in effectively meeting the HRIBF driver cyclotron requirements, since the residual radioactivity induced in the cyclotron by the fraction of the beam which is lost, is the major anticipated operating difficulty in such a cyclotron (as we discuss further in later paragraphs).

III. COMPUTING PLAN FOR EXTRACTION STUDIES

The critical features determining extraction efficiency in the multi-turn regime are the amplitude of the radial focusing oscillation in the accelerated beam and the alignment and thickness of the septum which separates the internal beam from the extracted orbit. Initially, the amplitude of the radial focusing oscillation is set by the phase space density of the beam at the exit of the ion source. Amplitudes used in this study are consistent with data from experiments on similar sources, but direct measurements of beam phenomena in a test cyclotron would be highly desirable (as discussed further in Section VI of this report). In a broad phase cyclotron, if the beam is

significantly off-center, the radial oscillation amplitude can be increased by the phenomenon of "precessional mixing" which effectively adds the magnitude of the centering error to the original incoherent oscillation. The Philips group then strongly stressed the importance of keeping the beam very accurately centered throughout the normal acceleration section of the magnet so that the Qr = 1 resonance at the edge of the field functions as an energy spectrometer and separates the continuum of energies in the broad phase beam into a set of peaks based on the precession cycle of the beam. The computing steps in the present study then consisted of:

1. Tracking the beam from the ion source thru detailed electric and magnetic field maps and adjusting the "centering coil" to achieve well centered orbits over a +/- 15 degree range of rf phase. In these runs, the range of rf phase was represented by a set of 7 starting times spaced at 5 degree intervals so as to cover a total rf phase range of 30 degrees.
2. The above family of 7 "central rays" (e.g. rays which start at a specified rf time directed straight ahead at 10 eV from the center of the ion source slit) were tracked thru the full cyclotron to the edge region where another coil (the "bump" coil) was adjusted to provide an approximately optimized precession amplitude.
3. Radial oscillations were added at 44.5 MEV, an intermediate point of the calculation where the influence of the centering coil had ended, and where detailed maps of the electric field could be replaced by a delta function gap approximation so that a much larger number of orbits could never-the-less be tracked in a reasonable time. In these computations the radial distribution of the beam relative to each of the 7 central ray phases was represented by 2 ellipses of 8 particles each, one with an average amplitude of 0.44 millimeters, the other with an average amplitude of 0.88 millimeters. This process then gave a total of 17 median plane rays at each of the 7 phases, (119 rays total).
4. Next, also at 44.5 MeV, an 8 point axial ellipse set to give an average axial amplitude of 1.6 millimeters was added to each of the 119 median plane rays. The median plane symmetry of the calculation makes 4 of the axial rays mirror images of the opposite 4, so that the total number of rays tracked was then 5x17x7 = 595. The orbit code used for this part of the calculation included higher order axial terms to 4th order in z.
5. A density histogram giving number of particles in specified radial bins vs radius was computed for the 595 orbit family and used to select a radius for the inner (toward the center of the cyclotron) edge of the deflector septum. With the septum radius selected, the density histogram was then replotted with each ray terminated at the deflector entrance, i.e. on the turn where its radius first exceeded the radius of the septum inner edge at the deflector entry angle.
6. At this point the energy and position coordinates of the family of orbits were transferred to a new special purpose, "Septum Penetration", code which contained precise (but somewhat simplified) geometric representations of the deflector septum, the outer tank wall of the cyclotron (including the deflector high voltage electrode), and of the inner structures at the ion source. For ions moving within the septum, an energy loss term was included based on dE/dx tables from detailed Monte Carlo calculations done with the program SRIM, but without including scattering. For simplicity, the Septum Penetration code includes axial motion only to first order in

z, since trajectories are typically short and higher order effects should therefore not have time to accumulate significantly.

7. When an ion penetrated either the outer tank wall or the central region electrodes, tracking was terminated and the location and energy recorded. Median plane graphs of either single orbits or of the complete family were plotted and a summary table showing energy and angular location (as a histogram of 10 degree bins) of the terminating point are printed. Locations at which beam is lost can then be used to approximately assess the distribution of induced radioactivity within the cyclotron as a basis for an initial concept for a remote handling system for removing the most activated components without excessive radiation exposure for workers.
8. Finally the group of rays which passed through the deflector aperture were tracked thru the remainder of the extraction system and plotted as an x envelope and a z envelope. In this calculation magnetic extraction elements, as shown in Figures A-III.14-16, were represented as combinations of pure dipoles and quadrupoles i.e. possible higher order multipoles were not included.

Results from these computational studies are described in the following subsection.

IV. CALCULATION RESULTS

For the purposes of these computations, centering of the beam was accomplished by adjusting the current in a 5 turn saddle coil (see Fig. A-III.9) located on the hill of each sector. The amplitude of the first harmonic component of the air core magnetic field produced by these "centering coils" is shown in Fig. II.2 (along with a similar plot for a similar set of coils in the valleys of the magnet at large radius, the "extraction coils"). The effect of the centering coils on the family of accelerated central rays is shown in Figures II.3,4,5,&6. Fig. II.3 first of all shows the behavior of the group of 7 central rays with the centering coils "off" and shows clearly a precessional amplitude of about 2.7mm for every phase. The other Figures (II.4, II.5, & II.6) all have the centering coils "on" and set to produce a magnetic first harmonic of 1.05 gauss at an azimuth of 183 degrees. Figure II.4 shows the "210 degree" central ray (i.e. a 10 ev particle moving straight ahead from the center of the source slit at an rf time of 210 degrees), the center point of the time distribution, and the centering coil first harmonic component of 1.05 gauss at an azimuth of 183 degrees leads to no detectable precession (i.e. centering error) in this ray. At the +/- 15 degree extremes of the time distribution (225 & 195 rf degrees respectively), a very small centering error of about 10 mils is just visible on the expanded scale of Figures II.5 & II.6. Taken together, the three Figures show both a very small overall centering error and a very small phase dependence in the residual error (about 0.7 mils per rf degree).

At this point in the study, a small discrepancy was noted in the optimization of the rf frequency, namely, that the ray which reached the extraction radius in the smallest number of turns (corresponding to the minimum energy spread) left the source at a time of 205 degrees rather than at 210 degrees, the ray which had been used to set the centering coil to the "no precession" condition. A loop back to correct this discrepancy would have involved repetition of a considerable amount of computation which appeared

incompatible with the schedule of the study program. The effect of correcting this discrepancy would moreover work to make the extraction efficiency slightly more favorable but since other comparable factors were also not optimized (also due to incompatibility with the strict time frame of the present study) it was deemed appropriate to bypass the small frequency mismatch by shifting the range of starting times by 5 degrees, to 190 thru 220 degrees. This then has the effect of slightly increasing the average centering error in the group since the best centered ray remains at 210 which is no longer the center of the phase group, and therefore reduces the calculated extraction efficiency by a small amount but not to a degree which significantly impacts conclusions of this study.

Using the revised 190 to 220 range of starting times, the extraction first harmonic (Figure II.2) was set to produce a first harmonic amplitude of 1.0 gauss at an azimuth of 275 degrees, which induces a precession amplitude corresponding to a radius gain on the final orbit approximately matching the 0.25" design aperture of the 1st electrostatic deflector. An 8-ray radial eigen-ellipse was then added to each central ray at an energy of 44.5 MeV (where both centering coil and bump coil were negligible so that one-sector ellipse parameters from the E.O. code could be used). The average amplitude of the ellipse was set at 35 mils (average turn width of 70 mils) and eight rays were distributed uniformly about the ellipse. Figures II.7, II.8, and II.9 show the behavior of three of these groups of rays in the radius interval beyond 30.2". These results establish that the precession loop is reasonably matched to the expected deflector aperture.

An undesirable feature of the precessing orbit families is the rather severe distortion of the radial ellipse for the 190 degree starting time, and the significant distortion for the 205 degree starting time, whereas the 220 degree starting time (fig. II.9) is well behaved. The distortion presumably reflects the shift of the beam to positive phase in the non-isochronous region at the edge of the field, so that the 190 and 205 degree groups pass through NuR=1 at a slower rate and therefore experience successively enhanced distortion. Modifying the magnetic field in the edge region of the magnet to reduce the phase slip in the transition region between the isochronous region and the NuR=0.8 extraction radius, would clearly reduce this unfavorable behavior but has been deferred for future study at this point.

The next step of the study augmented the family of rays by including a second 8-ray ellipse in each of the seven rf time groups, the second ellipse having an amplitude of 1/2 that of the outer ellipse. (Eight rays on each ellipse implies a higher density in phase space for the center part of the source aperture in accord with experimental observations.) Two eight point ellipses about each of seven central rays (one for each of the seven rf starting times) gives a total of 7x(1+8+8)=119 rays to track to the edge of the magnet. Results from this tracking were stored and in a separate program plotted as a histogram giving, at an azimuth of 60 degrees, the number of rays in each 5.55 mil radial interval; Figure II.10 is an example of such a histogram.

At this point an end-of-ray stop at the deflector entrance was added to the histogram routine to terminate each orbit at the point where its radius at an angle of 60 degrees first exceeded a preset value corresponding to the location of the inner edge of the deflector septum. The location of this stop is marked by a light vertical line in the histograms viz. at 31.949" for the

plot in Figure II.10. The cutoff divides the histogram into two distinct regions -- in the part of the histogram before the cutoff a given ray can be plotted an arbitrary number of times depending upon how many times it happens to pass through a specific radius interval, whereas beyond the cutoff, each ray appears only once, namely at its ending r value, so the integral of the bins beyond the dashed line must sum to the total number of rays in the data base, i.e. 119 for the family in Figure II.10.

Noting the reasonable match with the assumed deflector aperture for the median plane rays of Figure II.10, the family of rays was again expanded by adding an 8 point axial eigen-ellipse to each median plane ray with average axial amplitude of +/- 63 mils. Noting the median plane symmetry assumed for the computed magnetic field, the eight axial orbits reduce to four symmetric pairs so that the total family of tracked orbits increases to 7x(1+8+8)x5=595.

The new radial histogram including the axial orbits is shown in Fig. II.11. The axial motion (computed through fourth order terms in z including all coupling terms) notably makes no important change in the radial histogram, indicating that axial motion is well behaved. This is also indicated by Fig. II.12 which plots the maximum z value experienced by any ray in the ensemble at any azimuth versus radius; this "Zmax" distribution is likewise well behaved, the small increase in amplitude in the vicinity of 30" corresponding to the dip in NuZ at this radius (Fig A-III.5) and the step increase slightly beyond 31" corresponding to the coupling resonance NuR=2NuZ. (The smooth dependence of the R histogram with statistical fluctuations as the only perceptible structure prior to the first precession peak at 31.8" also indicates that the assortment of initial conditions for the 595 ray family smoothly covers the relevant interval of six dimensional phase space without bias favoring any particular sub element.)

Figure II.13 is a histogram showing energy distribution of the rays which have passed the 31.949 septum entry. The width of the distribution corresponds nicely to the expected "1/n" width of a centered system of orbits where n is the number of turns.

At this point the family of rays is transferred to the "Septum Penetration Code", the new program briefly described in the previous Subsection. This program tracks orbits in x,y coordinates (so that orbits can be tracked which fail to link the center of the cyclotron) and includes energy loss, but not scattering, based on a Monte Carlo calculation with the program SRIM [Zigler 95]. In the Septum Penetration Code numerical input tables give the radial position of the inner edge of the septum and of the outer tank wall; septum thickness is specified by a parameter. For the initial family of runs the table for the septum inner wall location was obtained by scanning the data table for the 119 ray median plane ensemble to pick up the maximum radius of the ensemble at each angle occupied by the septum. With this choice of septum location no median plane ray will hit the inner wall of the septum (and we assumed, incorrectly, that no axial ray would go to larger radius than the median plane rays). Table II.2 is a summary of the results from the septum penetration code for the 595 ray family extracted by a deflector with a 10 mil septum. The table groups rays into azimuthal bins, the bin at theta =100-110 (containing 529 rays) being the group of rays transmitted through the deflector -- loss fraction =(595-529)/595=11.1%. The bin corresponding to rays stopping in the septum contains 0 rays, the bin corresponding to rays hitting central region components contains 5 rays, and the remaining 61 rays

stop on the outer wall (which, in the angular interval from 60 to 120 degrees, represents the deflector high voltage electrode).

Table II.3 is a "lost ray" printout giving the initial coordinates and the final energy and final angular bin for each ray not in the transmitted group. Fig. II.14 is a composite plot of the trajectories of the 66 lost rays and shows the predominant grouping of these rays in the vicinity of theta = 0, i.e. in the hill preceding the deflector. Fig. II.14 also gives at the bottom a plot of the axial behavior of each of the lost rays and shows a considerable axial expansion of order x10 for a subgroup of the rays . A removable catcher assembly on the wall would therefore need to fill the complete 1.8" gap between the hills and when scattering is included in the penetration calculations a few rays will hit the hill surfaces proper, which may then also need an easily removable cover. (For simplicity the Septum Penetration Code uses only linear terms in z -- non-linear terms would be expected to couple part of the axial energy back into radial motion and reduce the overall axial expansion.)

Tables II.4 and II.5 and Figure II.15 are like Tables II.2 and II.3, and Figure II.14 except that the septum thickness is changed from 10 mils to 5 mils (the value used in the PSI Philips injector). The thinner septum reduces the number of lost rays to (595-553)/595=7.1% but the distribution is less concentrated with several rays not reaching the tank wall in the previous hill (the "TURN LIMIT" stop code in Table II.5); these rays then continue to circulate in very off-center orbits with considerable z growth therefore probably coming to a final end point on one of the dees.

The final computational step in the present study consisted of a check on the behavior of the rays transmitted by the first deflector to see that a well behaved beam envelope persisted through the remainder of the extraction elements (see Figures A-III.13,14,15,&16). Figure II.16 shows the results of this calculation and evidences well behaved envelopes out to the cyclotron exit port. The initial calculation shown here includes only dipole and quadrupole components of the magnetic elements -- higher order multipole components are normally a small correction in systems of this type and will be included in future more detailed studies.

At this point in the study, an incidental interest in tracking an orbit backward led to the realization that a number of rays (45) from the 595 ray family were in fact rays which hit the inner wall of the septum on a previous turn, a phenomenon which had not previously been tested for on the grounds that the selection of the septum location (on the Rmax envelope of the median plane rays) made it not possible for rays to hit the inner wall of the septum. A list of the 45 rays which hit the inner side of the septum (the side toward the center of the cyclotron) is given in Table II.6; six of these rays also had hit the outer wall in the septum penetration runs and so were already included in the lost ray count. The rays hitting the inner wall add a further septum loss term increasing the total loss fraction was increased to (595-(525-45+6))/595=18.3%.

Figure II.17 gives an R,Pr plot at the deflector entry angle. Rays which hit the leading edge of the 10 mil septum are between the vertical lines at R=39.949" and 39.959", rays which will further on hit the outer edge of the septum are just beyond the R=39.959" line and rays which hit the deflector high voltage electrode are beyond the line at 32.195". The initial phase of

the lost rays is indicated by the coding of the points, using the code shown at the top of the Figure. The additional lost rays due to hitting the inner side of the septum wall are plotted in Fig. II.18. This Figure has the same relative scales as Figure II.17 but with the zero shifted to include the large lost-ray cluster at the upper left, which from comparison with Table II.6 is seen to be due to rays hitting the septum on the previous precession cycle. A small change in the septum location or in the setting of the extraction bump would remove this group of lost rays and thereby return the total loss fraction to nearly the previous value i.e. (595-(525-6))/595=12.8%.

Unfortunately, rather extensive additional computing is required to quantitatively catalog the effect of moving the entry edge of the septum or of changing the extraction bump, and these runs have not yet been made. In the interim a deflector modification which involves only the septum penetration part of the calculation has been explored, namely leave the septum entry at the same radius, but move the downstream location out to clear all the particles in the inner wall loss group (the rays plotted in Fig. II.18). The downstream end of the septum moves out by 15 mils using this assumption for the optimum septum location and the deflector voltage must be increased to 140 kV/cm to hold the rays in the deflector aperture. Figure II.19 shows the R,Pr location of the 96 rays lost with these assumptions for the deflector septum position and strength; the lost ray fraction is improved somewhat (to 96/595=16.1%) but less than would be expected from the more desirable option of moving the previous precession loop group from Figure II.18 with an extraction bump readjustment.

The calculations described above imply that beam losses in a 200 microamp, 250 MeV, Compact Superconducting Cyclotron operating in the multi-turn extraction mode, can surely be below 10% and that 5% is a reasonable probable value for losses in a fully optimized system. (Various details of the operating configuration were not fully optimized for the calculations in this report in order to conform to the time and cost constraints of the sub-contract study). This result is quite consistent with the 7% loss rate given in the literature for the PSI Philips injector which also operated at 200 microamps with 7% extraction loss and with machine activation compatible with traditional "hands-on" maintenance procedures. There is, however, a major difference between the Philips injector and the cyclotron considered here, namely, that the energy is 250 MeV rather than 72 MeV; the nominal beam range in copper is then 63 millimeters rather than 7.4 millimeters, and, if the neutron yield is taken as the product of the increase in range (the increase in the number of target atoms per cm^2) times the increase in energy (approximately the increase in the number of neutrons per interaction) a total x32 factor results as the estimated increase in neutron production relative to the Phillips injector. (If the design energy were lowered to 200 MeV as has sometimes been discussed, the range in Copper is reduced to 43 millimeters and the estimated increase in neutron yield relative to the Phillips injector is reduced to x16 i.e. to half of the 250 MeV value.) The increase in neutron yield presumably implies a similar increase in residual radioactivity except for some small self-shielding benefit from the deeper neutron penetration which places the radioactive nuclei further from the surface of heavy components.

A factor of 30 increase in residual activity relative to a hands-on maintained machine is of course not overwhelming but must be carefully considered in the design stage of the project. An immediate straight-forward

approach in such a situation is simply to design devices which increase the distance between radioactive objects and workers by a factor of 5 (or do this to a partial degree and add intermediate shielding in the increased space). Figure II.20 is a perspective view of a relatively simple power activated arm which was designed at NSCL for deflector replacement and which approximately accomplishes the desired goal of increasing the distance between radioactive components and maintenance personnel by a factor of 5 (from about 1' for hands on to about 5' for the handling device shown). (A budget allocation for devices of this type is therefore included in the cost estimate.)

The previous design study provides adequately for other components of the 250 MeV CSC cyclotron. (The increase in beam power by a 10E4 factor to a level of 50 kw is well within the power range of the amplifier provided in the 1993 design.)

A significant neglected factor in the present study is the degree to which scattering and nuclear interactions in the septum further broaden the distribution of radioactivity implied by Figures II.14 & 15. To obtain a qualitative sense of the magnitude of the scattering effect we used the program SRIM to calculate the behavior of a group of 100 rays passing through 40.6 mm of Copper, corresponding to the average path length of unscattered rays in the 10 mil septum. At the exit of the 40.6 mm block, 11 of the 100 particles were displaced by more than 2 mm from the central ray and 11 rays had a direction change of more than 6 degrees relative to the straight ahead direction (six rays were in both of these groups, the other ten were in only one). Lacking at present a code which combines magnetic fields, complicated geometrical structures, and Monte Carlo scattering, we introduced displacements of +/- 1mm and +/- 6 degrees arbitrarily into one of the septum penetrating rays after it had traveled through 20 mm of the septum and thereafter tracked these 4 new rays with the Septum Penetration Code; plots of the resulting trajectories are shown in Figures II.21 & 22. The undisplaced ray and the +1 mm and + 6 degree rays are shown in Fig. II.21. The -6 degree ray quickly hit the deflector shoe and does not show in the Figures while the -1 mm ray continued on an off-center precession cycle for many turns as shown in Fig. II.22. These sample runs then imply that the distribution of radioactivity in the tank wall will broaden considerably (50 to 60 degrees) when scattering effects are realistically included in the calculations, and that such calculations should therefore be a priority component of further studies of the distribution of residual radioactivity.

At this moment in time, the CSC extraction optimization story cuts off since further computations have not yet been made, and needs of other projects have necessitated a temporary shift of key personnel to other assignments. This is clearly very dissatisfying, but as noted previously, a report must be made at this point in time to comply with stipulations of the sub-contract. Full optimization of the CSC extraction system to maximize extraction efficiency will be a focus of further calculations and further results will be reported at points of appropriate scientific completeness.

V. FURTHER COMPUTER STUDIES

When extraction studies resume, a first activity will be restructuring of two of the computer programs (SPIRAL GAP Z4 and SEPPEN) used for the orbit calculations described in the previous section, to more accurately incorporate

details of the geometry of the CSC design (the simultaneous presence of both centering and bump coils, the location of accelerating gaps, etc.), and to make it easier to transfer intermediate results between the programs (an output file from SPIRAL GAP providing starting coordinates for SEPPEN runs for orbits hitting either the inner wall or the front end or the entrance of the deflector, etc.).

With the revised programs the studies described in the previous section will be repeated with small inconsistencies of the present study eliminated, i.e. having the best centered ray as the center of the phase distribution, etc. A search on the extraction bump strength will be included to ascertain whether a slightly smaller bump would reduce distortion and therefore improve extraction efficiency without overly reducing the radius gain per turn.

At this point the study should also take a renewed look at the detailed design of the magnetic field, noting that the field for the present CSC study was simply taken over from the MSUCL-874 development program. An important detail to investigate with respect to the magnetic field is whether further sharpening of the field turn-over at the transition from Isochronous to extraction can significantly reduce the phase slip as the beam approaches the magnet edge so as to reduce the distortion from passing through NuR=1 at an "off-peak" rf phase.

Another future highly desirable computation study is to explore the benefits vs cost of lowering the magnetic field so as to make the overall cyclotron somewhat larger. This would clearly increase turn spacing and extraction efficiency, and would reduce the electric field required in the deflectors all of which are quite desirable. Magnet weight and size would go up, but the CSC accelerator is quite small compared to the desired location in Room C110 as is indicated in the next section so a somewhat larger cyclotron would not be a problem. Costs would also presumably increase as the field is lowered, but the CSC already has a large margin in this area relative to other accelerator choices and so a somewhat higher cost would perhaps be an attractive tradeoff in gaining a more relaxed operating situation.

A particularly interesting step in the direction of exploring larger, lower-field compact style cyclotrons is to lower the field to the point where a room temperature coil can provide the needed ampere turns with a reasonable power dissipation (500 kw or less). Such a cyclotron study would provide an opportunity to compare the design concepts of the 230 MeV cyclotron being constructed by the Ion Beam Applications (IBA) Corp. for Massachusetts General Hospital, against a more conventional compact cyclotron design. The most significant feature in this regard would be the use of a larger magnet gap (46mm vs 9mm) to provide for the x10,000 increase in the desired beam current. The larger magnet gap also brings field gradients into the regime where conventional orbit tracking techniques are known to be reliable which is also an important benefit. The main magnet coils in such a cyclotron could also easily be superconducting in order to reduce operating costs. Omitting the liquid helium system has the advantage of eliminating downtime associated with routine refrigerator maintenance, but operating expenses for electric energy are considerably increased.

An initial brief exploration of such a magnet has already been made and results seem favorable. Figure V.1 shows the arrangement of magnet steel assumed for this study and Figure V.2 shows the important azimuthal average of

the magnetic field predicted by the calculation. The coil current has been adjusted to match the maximum bending power of the magnet with the rigidity of 250 MeV protons. At this current, the coil power is approximately 450 kw and with further work, the radial shape of the field could clearly be easily matched to the required isochronous shape. Magnet weight is 176 tons vs the 80 ton weight of the MSUCL-874 design, and the outer diameter is (coincidentally) 176 inches vs 122 for the MSUCL-874 configuration. Further exploration of this interesting design concept, designated an RTC in the list of options in the Introduction, is clearly a very desirable direction for further study.

A future desirable computing capability on which we will at the moment defer work is to include scattering effects in the SEPPEN code when particles are passing through the septum. At the moment this appears to be a very large programming assignment and it seems clear that the results of such studies will not significantly impact major features of the cyclotron design. The number of particles lost in the extraction system will be the same and the total radioactivity induced in the cyclotron will be nearly the same; The distribution of the radioactivity will be different with the general feature of being distributed more broadly than indicated by the present calculations but generally in the fashion implied by the orbits shown in Figures II.21 & II.22. The issues described in preceding paragraphs (assessing whether to change the main magnetic field to a lower value, optimizing extraction efficiency, etc.) have very much greater impact on the overall evolution of the project and should therefore take precedence over more accurate calculations of the effects of septum scattering. In the interim, some additional calculations of the type shown in Figures II.21 & 22, with smaller steps in energy, will suffice to provide adequate guidance for the design of removable beam catchers and associated robotic handling devices.

VI. CSC AND SSC IN ROOM C110

As noted in the Introduction, studies of a Separated Sector Cyclotron to meet the HRIBF specifications are in progress, but less advanced than the CSC study (since the latter had the benefit of being able to start from a previous report). A separate report on the SSC study will be prepared at a later date; the work has however already evolved to the point where the basic magnet configuration is clear and we therefore use these results here to show how either the CSC or the SSC might be set up in room C110.

Figure VI.1 is a perspective view of the magnet configuration that would be used for a 220 MeV SSC to give a sense of the overall size of this magnet relative to a 6 foot person. Figures VI.2 & VI.3 show a possible location for both the CSC cyclotron and the SSC in Room C110, Figure VI.2 being a plan view and Figure VI.3 a vertical section view (with the 6' man included). In both of these Figures the CSC and SSC cyclotrons are superimposed, the CSC structure being cross-hatched and the SSC shown as outlines. Viewing these Figures, we conclude that it is clearly feasible to install either a CSC or an SSC in Room C110, but the CSC system is much smaller, lighter, and less crowded, and therefore can be expected to be significantly easier to install. At this time, no detailed planning of how this might be accomplished has been undertaken for either option.

VII. COST ESTIMATES

Section V of the Appendix describes the process used in 1993 to estimate the cost of the 250 MeV medical cyclotron, the structure assumed for the CSC studies in this report. Table A-V.1 (page 74) displays sub-elements and results from this previous Feb 1993 cost study. In this Table, data from the upper part is collected and summed in lines 50 through 59 of the third column. We omit two items from this list, namely, the Industrial Partner Compensation @$140k(x1.45) (which would not be relevant for this project) and the Contingency @$437k (since Contingency will be provided by HRIBF on an overall basis for their entire upgrade proposal) and obtain a base cyclotron cost in 93k$ of $4164.74k. We next adjust this figure to a 1996$ basis using the Consumer Price Index, and add 280k$ (96) for remote handling devices to arrive at a final total cost for the CSC System of $4807k$ (96) not including Contingency.

Manpower Subtotal	1260.54	
Plus supervision @18%	1487.83	
Fringe benefits @34%	505.73	
Inspection Travel	30.00	
Subtotal		2023.56
Indirect at 45% of above		910.60
Procurement		1230.58
Total Cyclotron Estimate 1993 k$		4164.74
Escalate to 1996 k$		x1.087
Total Cyclotron 1996 k$		4527.07
Remote handling devices		280.00
CSC System Total 1996$		4807.07

No cost data for the SSC are available at this time; comparisons based on data in the "Cyclotron Characteristics" section of the Proceedings of the several International Cyclotron Conferences give a factor of approximately x4 as the expected cost ratio between SSC and CSC thus implying a cost of about 20 M$ for an SSC system.

VIII. SUMMARY COMMENTS AND RECOMMENDATIONS

The large cost advantage of the high current Compact Superconducting Cyclotron make it (or a modification with lower magnetic field) the leading candidate as the ORIC replacement for HRIBF. The basic feasibility of such an accelerator is clear; reducing residual radioactivity by fully optimizing the multi-turn extraction process is an essential component of a sound design and exploring the marginal cost/benefit of reducing the magnetic field by incremental amounts is an important element of a sound design optimization process. In this application, a CSC accelerator would constitute a significant extension of the operating regime of such devices, and such a project would therefore make an important advance on the technical frontiers of accelerator physics, which, together with cost effectiveness, can be a powerful and significant element in the overall rationale supporting the request for funding for such a project.

One of us (HB) strongly recommends proceeding vigorously with further design on the CSC system (while completing the already in progress SSC study) and bypassing initiation of further exploratory studies of other options. Any of the accelerator systems listed as candidates in the Introduction can

undoubtedly be made to work, but a sharply focused, in-depth effort always has much greater impact than broad, necessarily shallow surveys. We strongly recommend that HRIBF as soon as possible select one option as its design choice and put all available effort into the fullest attainable development of that option.

Table II.1
CSC basic parameters

Extraction radius θ=60°	31.2"(79.25cm)
Field at r=0	2.38 Tesla
Avg. Field at extraction	3.06 Tesla
Maximum Hill field`	3.60 Tesla
Final Orbit Bending Power	2.432 Tesla meter
# sectors	4
# Trim Coils	0
# Harmonic Coils	2 sets ("centering bump" & "Extraction bump")
Orbital frequency	36.258 MHz
Harmonic #	2
RF Frequency	72.516 MHz
Amplifier rf Power	150 kW
Weight of magnet steel	80 tons

Ion Source: Cold Cathode
Tantalum Cathodes
0.25" dia by .010" wall Molybdenum Chimney

Extraction:

2 electrostatic deflectors operating at 100 kV/cm and 83 kV/cm
6 passive iron bars magnetic focusing elements

Table II.2
Ray summary (10 mil septum)

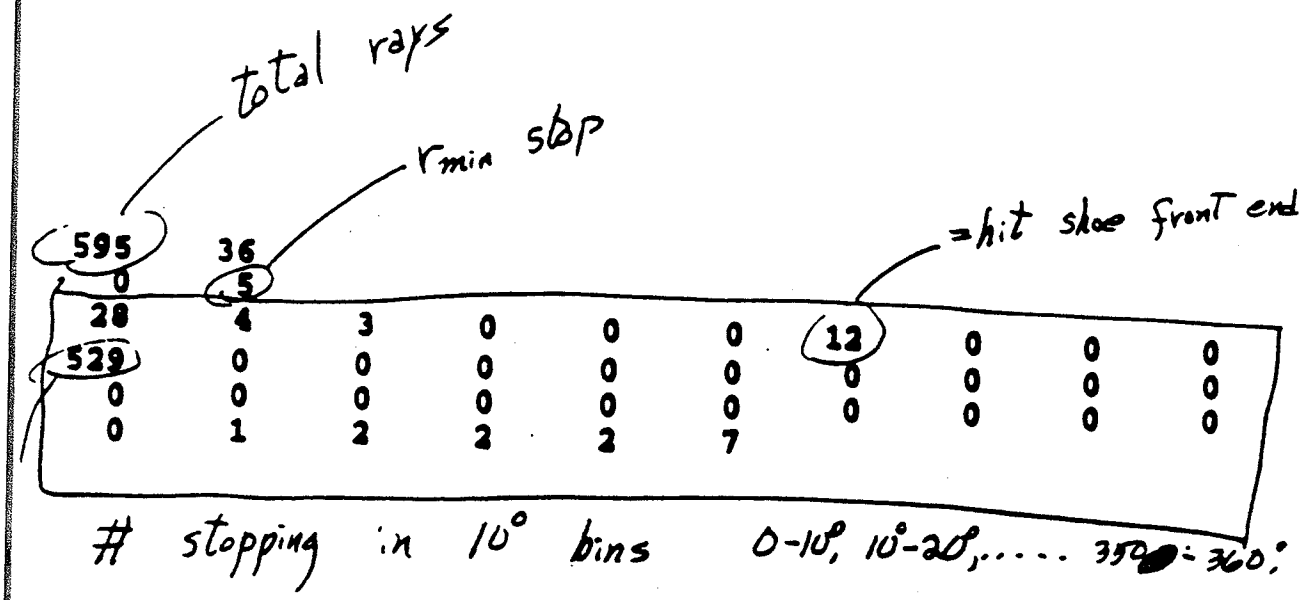

Table II.3
Lost Rays -- (10 mil septum)

37	60.000	31.95768	2.71988	250.199829	72.885049	-3171 RMAX BIN	2
57	60.000	31.95712	2.74861	250.225861	63.480295	-3231 RMIN	
65	60.000	31.94888	2.74899	250.088684	135.704230	-3244 RMAX BIN	36
69	60.000	31.95001	2.72666	249.991379	131.682642	-3253 RMAX BIN	36
74	60.000	31.94917	2.70863	250.018387	158.485953	-3263 RMAX BIN	33
75	60.000	32.20966	2.53212	250.421097	250.421983	-3264 RMAX BIN	7
77	60.000	32.20381	2.53974	250.552597	250.553486	-3271 RMAX BIN	7
88	60.000	31.95524	2.71523	250.192123	90.800323	-2002 RMAX BIN	1
108	60.000	32.22138	2.52462	250.513824	250.514708	-2142 RMAX BIN	7
112	60.000	31.95019	2.68999	250.101166	151.059143	-2151 RMAX BIN	34
113	60.000	32.21147	2.52006	250.479919	250.480801	-2152 RMAX BIN	7
117	60.000	32.23461	2.51472	250.488281	250.489161	-2161 RMAX BIN	7
118	60.000	32.20506	2.52652	250.490799	250.491683	-2162 RMAX BIN	7
123	60.000	32.21244	2.53429	250.536499	250.537386	-2172 RMAX BIN	7
147	60.000	31.95141	2.67560	250.063354	139.550207	-2241 RMAX BIN	35
148	60.000	32.21168	2.51204	250.452560	250.453439	-2242 RMAX BIN	7
151	60.000	32.20974	2.51571	250.390747	250.391627	-2250 RMAX BIN	7
156	60.000	32.19870	2.52399	250.415207	250.416090	-2260 RMAX BIN	7
161	60.000	31.95660	2.69270	250.137955	86.354182	-2270 RMAX BIN	1
162	60.000	32.21079	2.52644	250.505936	250.506820	-2271 RMAX BIN	7
176	60.000	31.95359	2.72042	250.047897	99.200682	-1110 RMAX BIN	1
180	60.000	31.95321	2.72378	250.046768	103.416067	-1114 RMAX BIN	1
215	60.000	31.94889	2.73979	250.026962	139.508271	-1184 RMAX BIN	35
217	60.000	31.95135	2.69827	250.086060	131.793574	-1211 RMAX BIN	36
222	60.000	32.22907	2.51121	250.410278	250.411157	-1221 RMAX BIN	7
225	60.000	31.96186	2.69014	250.058609	90.784054	-1224 RMIN	
254	60.000	31.95083	2.75041	250.049210	111.710097	-1283 RMAX BIN	1
341	60.000	31.95347	2.70669	250.008591	107.537163	1000 RMAX BIN	1
342	60.000	31.95119	2.72885	250.026749	115.766354	1001 RMAX BIN	1
343	60.000	31.95390	2.69792	250.019943	107.551220	1002 RMAX BIN	1
357	60.000	31.95159	2.71432	250.026581	119.806796	1131 RMAX BIN	1
358	60.000	31.96281	2.67615	250.014023	111.797767	1132 RMAX BIN	2
377	60.000	31.95277	2.74126	250.020996	99.166593	1171 RMAX BIN	1
381	60.000	31.95691	2.72006	250.016205	77.228344	1180 RMAX BIN	1
395	60.000	31.94880	2.73156	250.050674	151.002106	1224 RMAX BIN	34
397	60.000	31.95225	2.69855	250.019470	119.798251	1231 RMAX BIN	1
398	60.000	31.97037	2.65549	250.001282	103.502245	1232 RMIN	
417	60.000	31.95726	2.75045	250.009689	63.169394	1271 RMIN	
425	60.000	31.95081	2.75734	250.039551	107.575500	1284 RMAX BIN	1
427	60.000	31.94871	2.71865	249.973221	165.866633	2001 RMAX BIN	32
437	60.000	31.95545	2.72602	249.968277	81.680060	2121 RMAX BIN	1
441	60.000	31.95368	2.71722	249.950623	99.077435	2130 RMAX BIN	1
443	60.000	31.95687	2.70190	249.967773	81.679384	2132 RMAX BIN	1
448	60.000	31.96388	2.68492	249.964310	99.256544	2142 RMAX BIN	3
451	60.000	31.96257	2.68729	249.949219	107.610382	2150 RMAX BIN	3
452	60.000	31.95411	2.70127	249.973648	103.324412	2151 RMAX BIN	1
453	60.000	31.95932	2.67974	249.961899	119.845169	2152 RMAX BIN	1
456	60.000	31.95288	2.68825	249.947006	119.711202	2160 RMAX BIN	1
485	60.000	31.94967	2.74648	249.979431	123.758111	2234 RMAX BIN	1
492	60.000	31.95799	2.68319	249.968597	81.680489	2251 RMAX BIN	1
493	60.000	31.96882	2.65844	249.951218	107.606020	2252 RMAX BIN	3
496	60.000	31.95790	2.66897	249.938705	86.091653	2260 RMAX BIN	1
514	60.000	31.95511	2.69435	249.923355	99.042898	3003 RMAX BIN	1
529	60.000	31.94895	2.71351	249.926270	163.109520	3133 RMAX BIN	33
531	60.000	31.95259	2.70979	249.909729	111.538953	3140 RMAX BIN	1
540	60.000	31.95162	2.68573	249.946350	131.629896	3154 RMAX BIN	36
543	60.000	31.95740	2.69597	249.942215	81.645182	3162 RMAX BIN	1
545	60.000	31.95211	2.67452	249.937210	131.619189	3164 RMAX BIN	36
546	60.000	31.96154	2.67430	249.896881	127.754039	3170 RMAX BIN	36
549	60.000	31.96331	2.67335	249.918686	111.679964	3173 RMAX BIN	2
568	60.000	31.95239	2.73787	249.920258	103.257512	3232 RMAX BIN	1
572	60.000	31.95125	2.72754	249.956467	115.680976	3241 RMAX BIN	1
577	60.000	31.95408	2.69965	249.972153	103.322540	3251 RMAX BIN	1
580	60.000	31.96349	2.67324	249.966797	111.739594	3254 RMAX BIN	2
585	60.000	31.96418	2.65459	249.949371	127.808134	3264 RMAX BIN	36
589	60.000	31.97505	2.64868	249.910660	94.921173	3273 RMIN	

Table II.4
Ray summary -- (5 mil septum)

36								
0								
0	0	0	0	0	12	0	0	0
0	0	0	0	0	0	0	0	0
0	0	0	0	0	0	0	0	0
1	2	2	2	6				

Table .II.5
Lost Rays -- (5 mil septum)

65	60.000	31.94888	2.74899	250.088684	135.704230	-3244 RMAX BIN	36
69	60.000	31.95001	2.72666	249.991379	131.682642	-3253 RMAX BIN	36
74	60.000	31.94917	2.70863	250.018387	158.485953	-3263 RMAX BIN	33
75	60.000	32.20966	2.53212	250.421097	250.421983	-3264 RMAX BIN	7
77	60.000	32.20381	2.53974	250.552597	250.553486	-3271 RMAX BIN	7
108	60.000	32.22138	2.52462	250.513824	250.514708	-2142 RMAX BIN	7
112	60.000	31.95019	2.68999	250.101166	151.059143	-2151 RMAX BIN	34
113	60.000	32.21147	2.52006	250.479919	250.480801	-2152 RMAX BIN	7
117	60.000	32.23461	2.51472	250.488281	250.489161	-2161 RMAX BIN	7
118	60.000	32.20506	2.52652	250.490799	250.491683	-2162 RMAX BIN	7
123	60.000	32.21244	2.53429	250.536499	250.537386	-2172 RMAX BIN	7
147	60.000	31.95141	2.67560	250.063354	139.550207	-2241 RMAX BIN	35
148	60.000	32.21168	2.51204	250.452560	250.453439	-2242 RMAX BIN	7
151	60.000	32.20974	2.51571	250.390747	250.391627	-2250 RMAX BIN	7
156	60.000	32.19870	2.52399	250.415207	250.416090	-2260 RMAX BIN	7
162	60.000	32.21079	2.52644	250.505936	250.506820	-2271 RMAX BIN	7
215	60.000	31.94889	2.73979	250.026962	139.508271	-1184 RMAX BIN	35
217	60.000	31.95135	2.69827	250.086060	131.793574	-1211 RMAX BIN	36
222	60.000	32.22907	2.51121	250.410278	250.411157	-1221 RMAX BIN	7
254	60.000	31.95083	2.75041	250.049210	111.710097	-1283 RMAX BIN	1
342	60.000	31.95119	2.72885	250.026749	115.766354	1001 RMAX BIN	1
343	60.000	31.95390	2.69792	250.019943	135.761531	1002 RMAX BIN	36
357	60.000	31.95159	2.71432	250.026581	119.806796	1131 RMAX BIN	1
377	60.000	31.95277	2.74126	250.020996	176.981035	1171 TURN LIMIT	1
395	60.000	31.94880	2.73156	250.050674	151.002106	1224 RMAX BIN	34
397	60.000	31.95225	2.69855	250.019470	119.798251	1231 RMAX BIN	1
425	60.000	31.95081	2.75734	250.039551	107.575500	1284 RMAX BIN	1
427	60.000	31.94871	2.71865	249.973221	165.866633	2001 RMAX BIN	32
453	60.000	31.95932	2.67974	249.961899	143.425698	2152 TURN LIMIT	1
456	60.000	31.95288	2.68825	249.947006	119.711202	2160 RMAX BIN	1
485	60.000	31.94967	2.74648	249.979431	123.758111	2234 RMAX BIN	1
492	60.000	31.95799	2.68319	249.968597	143.427246	2251 TURN LIMIT	1
496	60.000	31.95790	2.66897	249.938705	162.239165	2260 TURN LIMIT	1
514	60.000	31.95511	2.69435	249.923355	139.525751	3003 TURN LIMIT	1
529	60.000	31.94895	2.71351	249.926270	162.109520	3133 RMAX BIN	33
531	60.000	31.95259	2.70979	249.909729	111.538953	3140 RMAX BIN	1
540	60.000	31.95162	2.68573	249.946350	131.629896	3154 RMAX BIN	36
545	60.000	31.95211	2.67452	249.937210	131.619189	3164 RMAX BIN	36
568	60.000	31.95239	2.73787	249.920258	103.257512	3232 RMAX BIN	1
572	60.000	31.95125	2.72754	249.956467	115.680976	3241 RMAX BIN	1
577	60.000	31.95408	2.69965	249.972153	143.437609	3251 TURN LIMIT	1
585	60.000	31.96418	2.65459	249.949371	158.534883	3264 TURN LIMIT	1
-1							

Table II.6
Rays that hit low-radius side of septum
(595 Z^4 rays, septum from median-plane runs)

22	385	64.000	32.09633	2.58595	42.518	250.166183	-3141
55	382	92.000	32.36819	-1.40739	27.433	249.096909	-3224
57	382	66.000	32.16761	2.51201	25.710	248.856888	-3231
113	380	92.000	32.36871	-1.40809	26.452	248.847351	-2152
118	380	78.000	32.43670	0.76776	25.735	248.864059	-2162
123	380	70.000	32.28455	1.99085	26.885	248.831543	-2172
124	383	64.000	32.09606	2.59015	45.483	250.174606	-2173
128	380	72.000	32.33414	1.67463	27.484	248.902954	-2182
133	380	68.000	32.22559	2.25327	29.209	249.007233	-2212
153	380	70.000	32.28339	2.01298	24.765	248.626617	-2252
154	380	66.000	32.16446	2.54703	24.965	248.629211	-2253
157	380	94.000	32.32335	-1.74879	25.869	248.758957	-2261
158	379	66.000	32.16560	2.52707	21.041	248.154572	-2262
159	379	68.000	32.22917	2.23081	20.680	248.155106	-2263
161	380	100.000	32.13722	-2.52504	29.144	248.904114	-2270
162	380	84.000	32.45926	-0.16052	26.197	248.887222	-2271
163	379	64.000	32.09697	2.73895	22.651	248.288239	-2272
164	380	66.000	32.16813	2.52274	26.894	248.791443	-2273
167	379	70.000	32.28317	1.96714	23.315	248.437637	-2281
168	379	66.000	32.16558	2.50812	23.843	248.436890	-2282
188	377	94.000	32.32309	-1.75740	28.555	248.771179	-1132
193	377	70.000	32.28348	1.97418	27.125	248.621277	-1142
194	377	68.000	32.22618	2.24598	27.355	248.621277	-1143
228	377	68.000	32.22701	2.29054	27.926	248.663971	-1232
229	377	72.000	32.33404	1.66643	27.335	248.666428	-1233
231	377	72.000	32.33413	1.67105	26.904	248.569794	-1240
233	377	64.000	32.09653	2.74687	27.255	248.556320	-1242
234	377	64.000	32.09890	2.72219	27.288	248.555847	-1243
238	378	70.000	32.28355	1.96461	30.394	248.984589	-1252
239	378	66.000	32.16679	2.50135	31.095	248.981216	-1253
250	380	64.000	32.09720	2.59910	44.990	249.962250	-1274
302	374	88.000	32.43200	-0.78398	30.495	248.736206	0211
303	374	68.000	32.23028	2.26763	30.581	248.640701	0212
308	374	66.000	32.16764	2.51294	30.724	248.624268	0222
378	376	66.000	32.16312	2.33946	53.611	250.019806	1172
404	373	90.000	32.40480	-1.07602	35.117	248.899246	1243
405	373	78.000	32.43654	0.75571	34.215	248.903458	1244
409	372	68.000	32.22721	2.25605	30.013	248.320145	1253
410	372	66.000	32.16439	2.50279	30.317	248.320374	1254
415	373	66.000	32.16615	2.51021	35.101	248.793015	1264
480	376	68.000	32.22521	2.11968	56.696	249.967575	2224
504	372	80.000	32.45254	0.43359	33.984	248.528915	2273
509	372	68.000	32.22785	2.25582	34.885	248.434631	2283
510	372	68.000	32.22667	2.23431	34.906	248.435226	2284
528	377	64.000	32.09536	2.56981	62.337	249.925964	3132

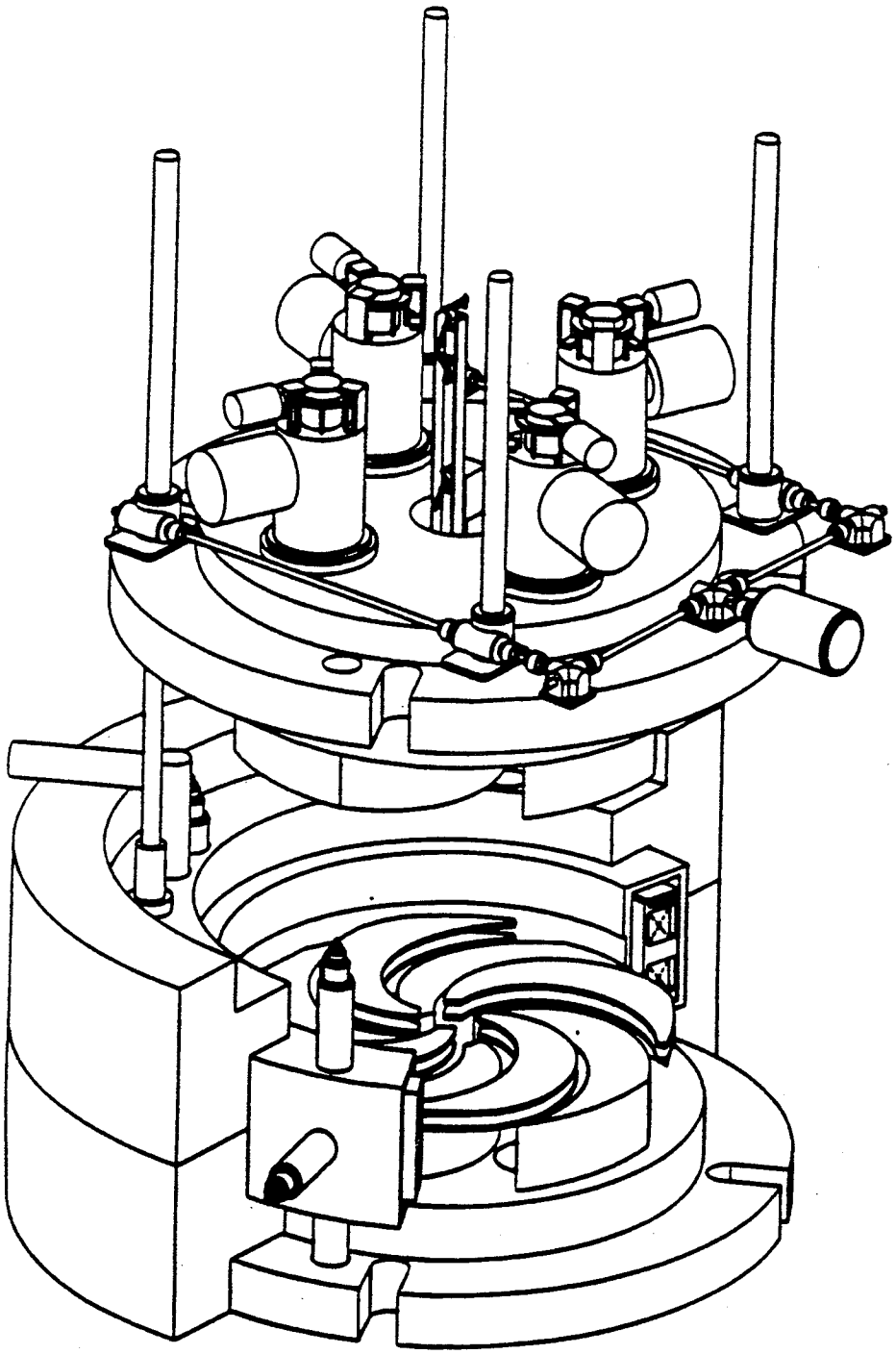

Fig. II.1 Perspective view of the 250 MeV superconducting medical cyclotron showing relative arrangement of major components. The upper pole cap is raised. Outer magnet rings and cryostat are cut away to give view of the spiral pole tips and of the accelerating electrodes.

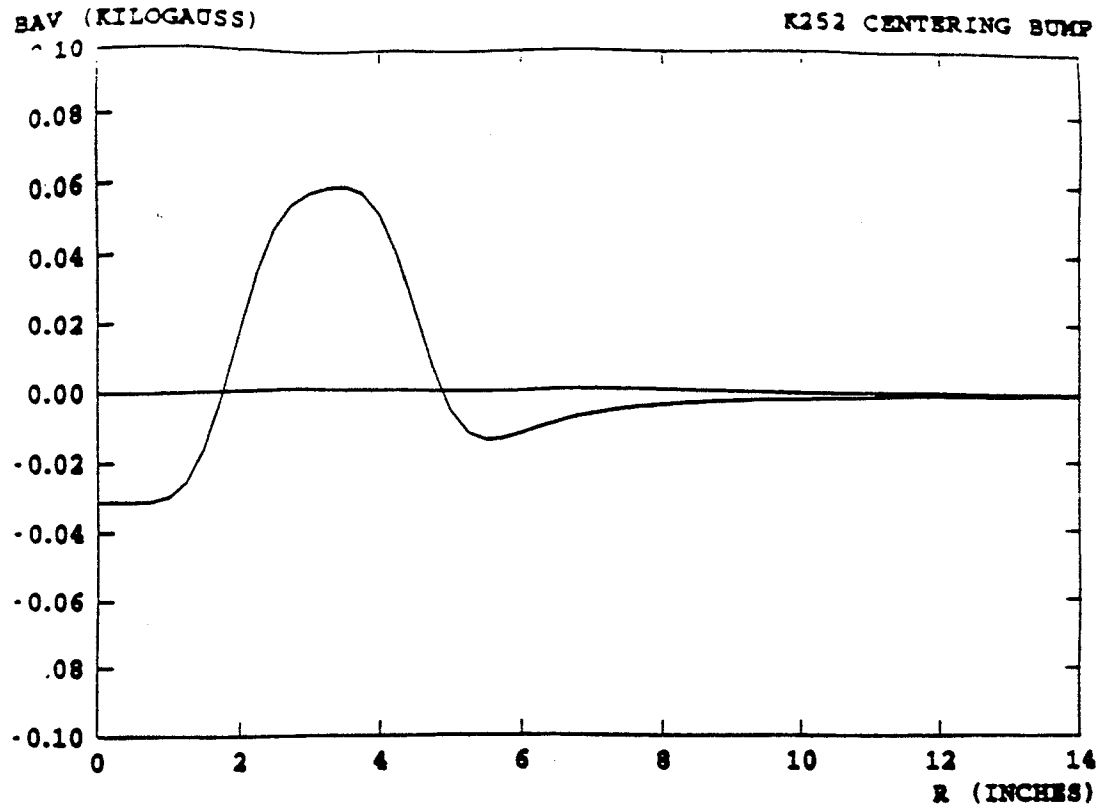

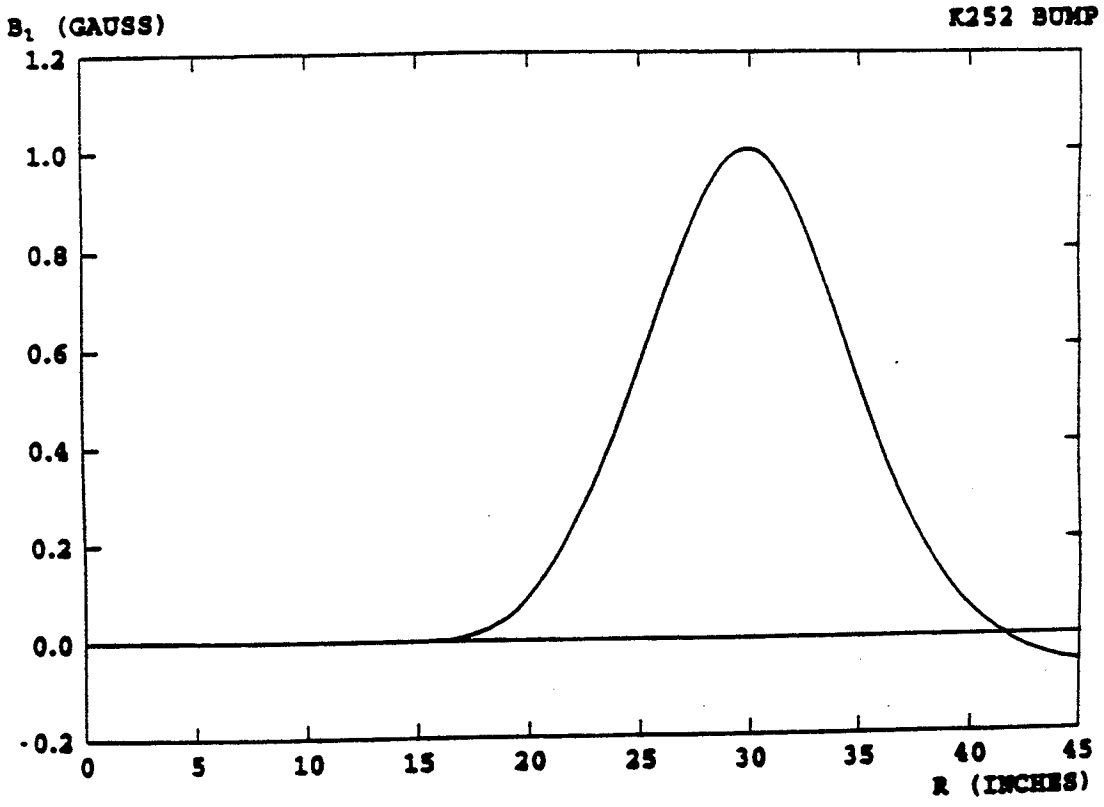

Fig. II.2 First harmonic fields for the centering and extraction bump with a coil excitation of 400 A.

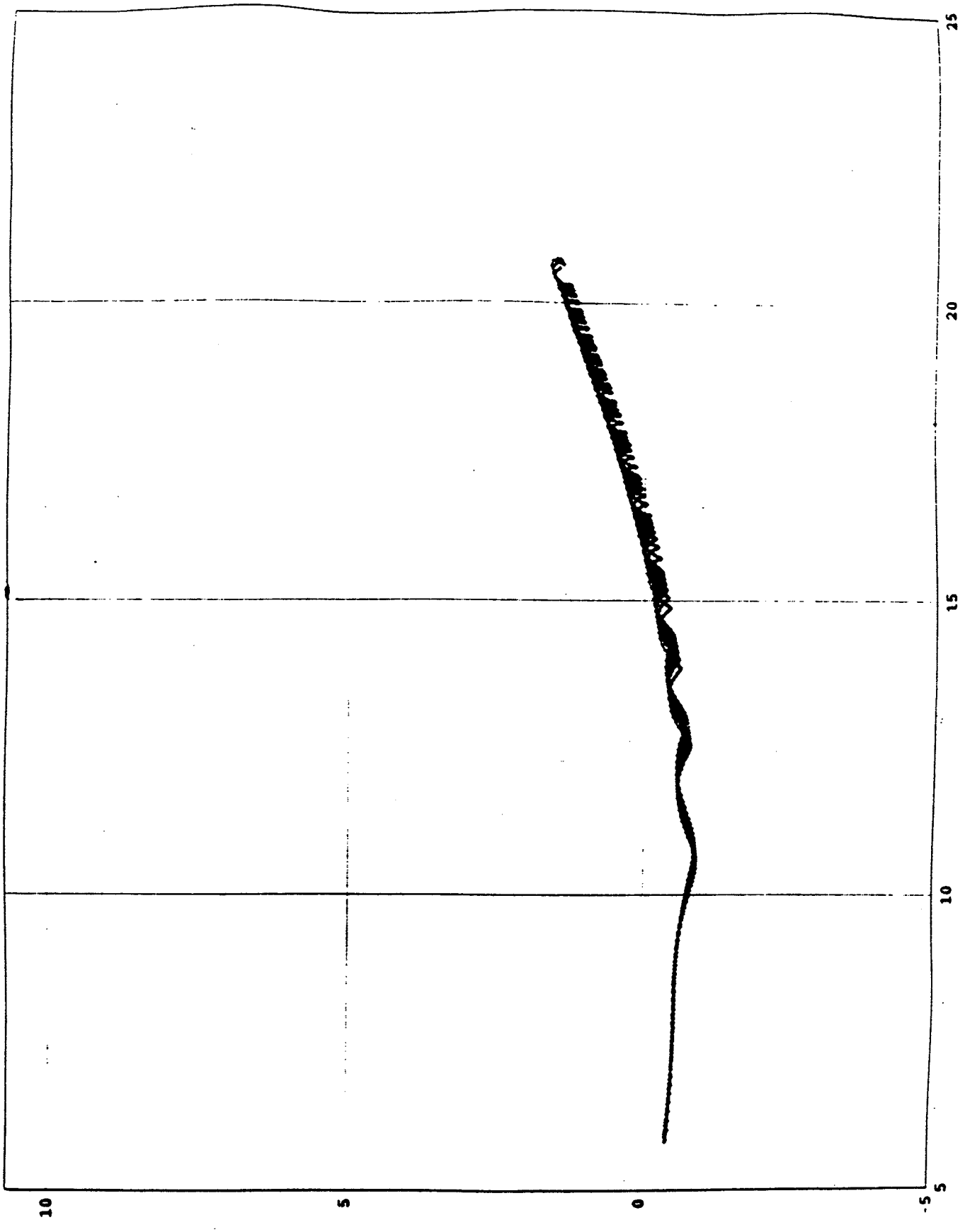

Fig. II.3 Pr vs. R for the group of seven central rays showing centering error when no centering coil is used.

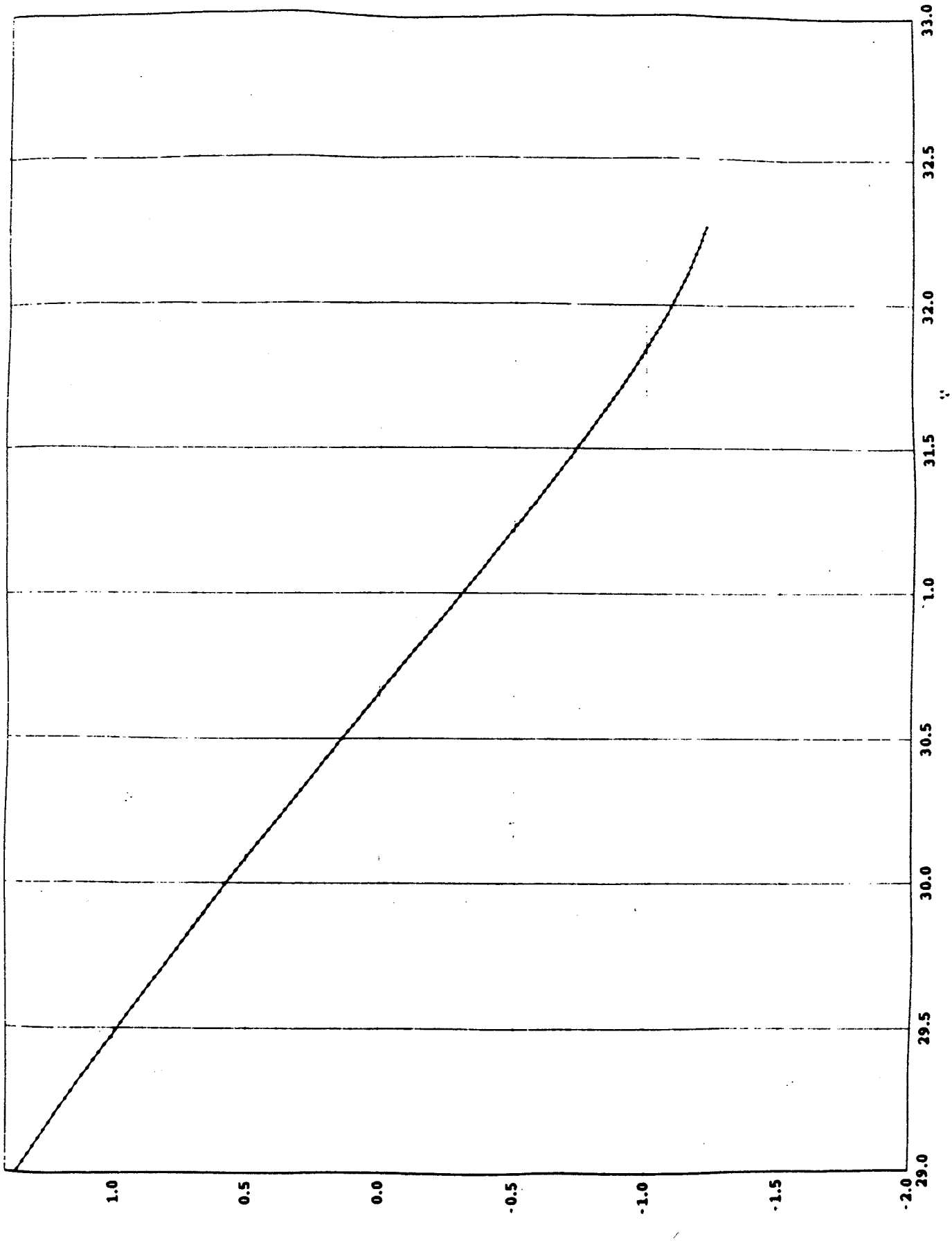

Fig. II.4 Pr vs. R for the central ray starting at to=210 degrees with a first harmonic bump of 1.05 gauss at 183 degrees. The last turn is turn 556.

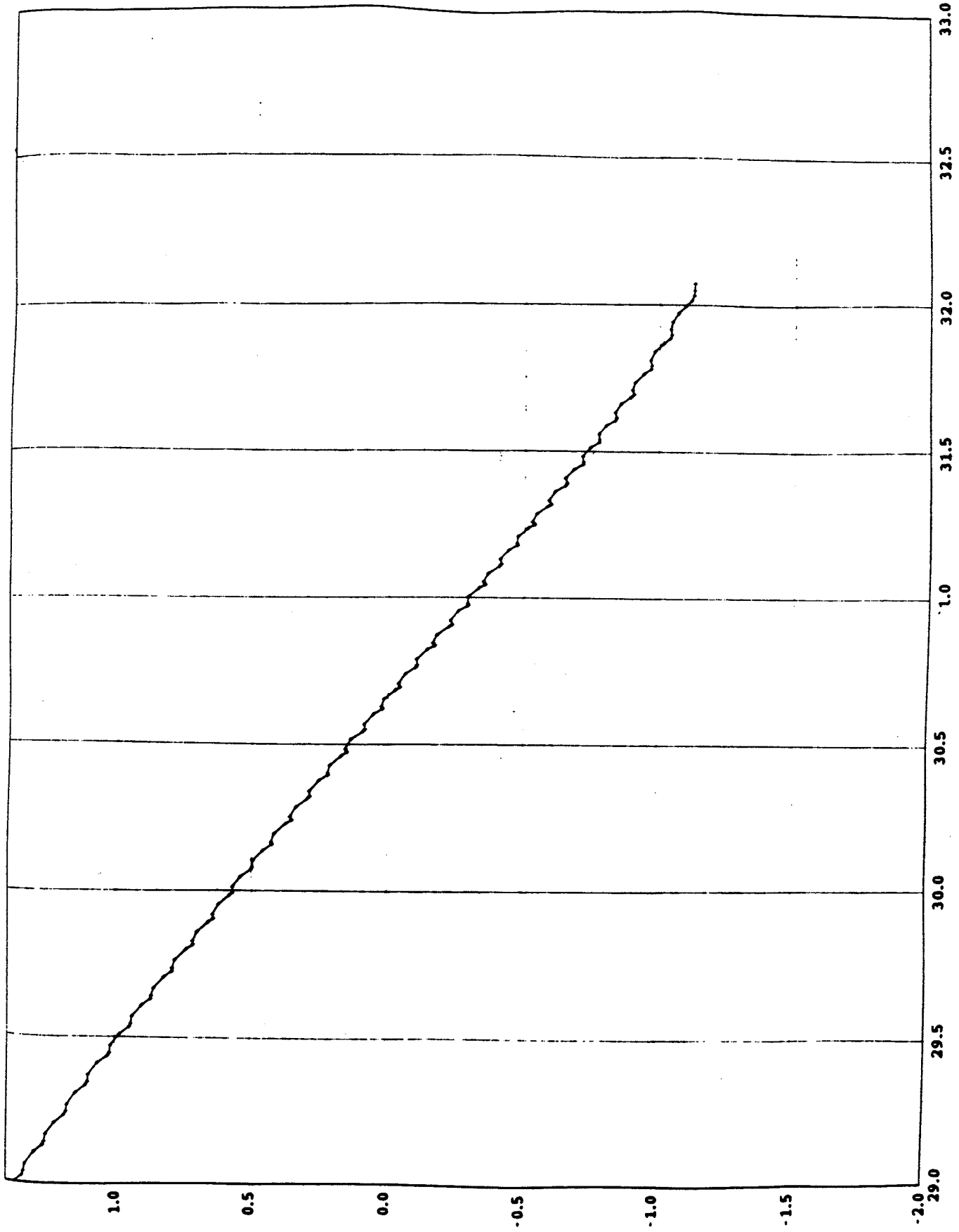

Fig. II.5 Pr vs. R for the central ray starting at to=195 degrees with a first harmonic bump of 1.05 gauss at 183 degrees. The last turn is turn 556.

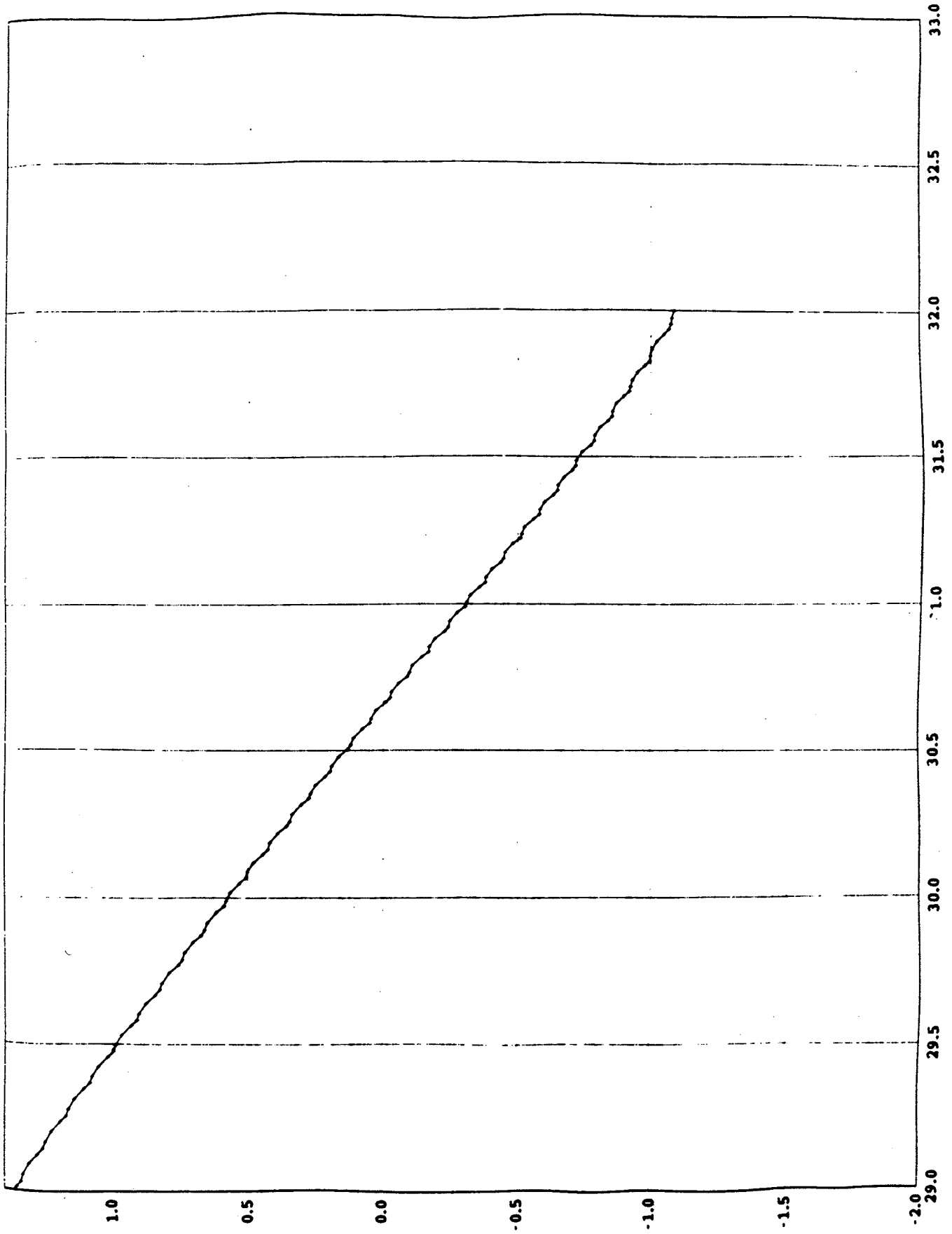

Fig. II.6 Pr vs. R for the central ray starting at to=225 degrees with a first harmonic bump of 1.05 gauss at 183 degrees. The last turn is turn 556.

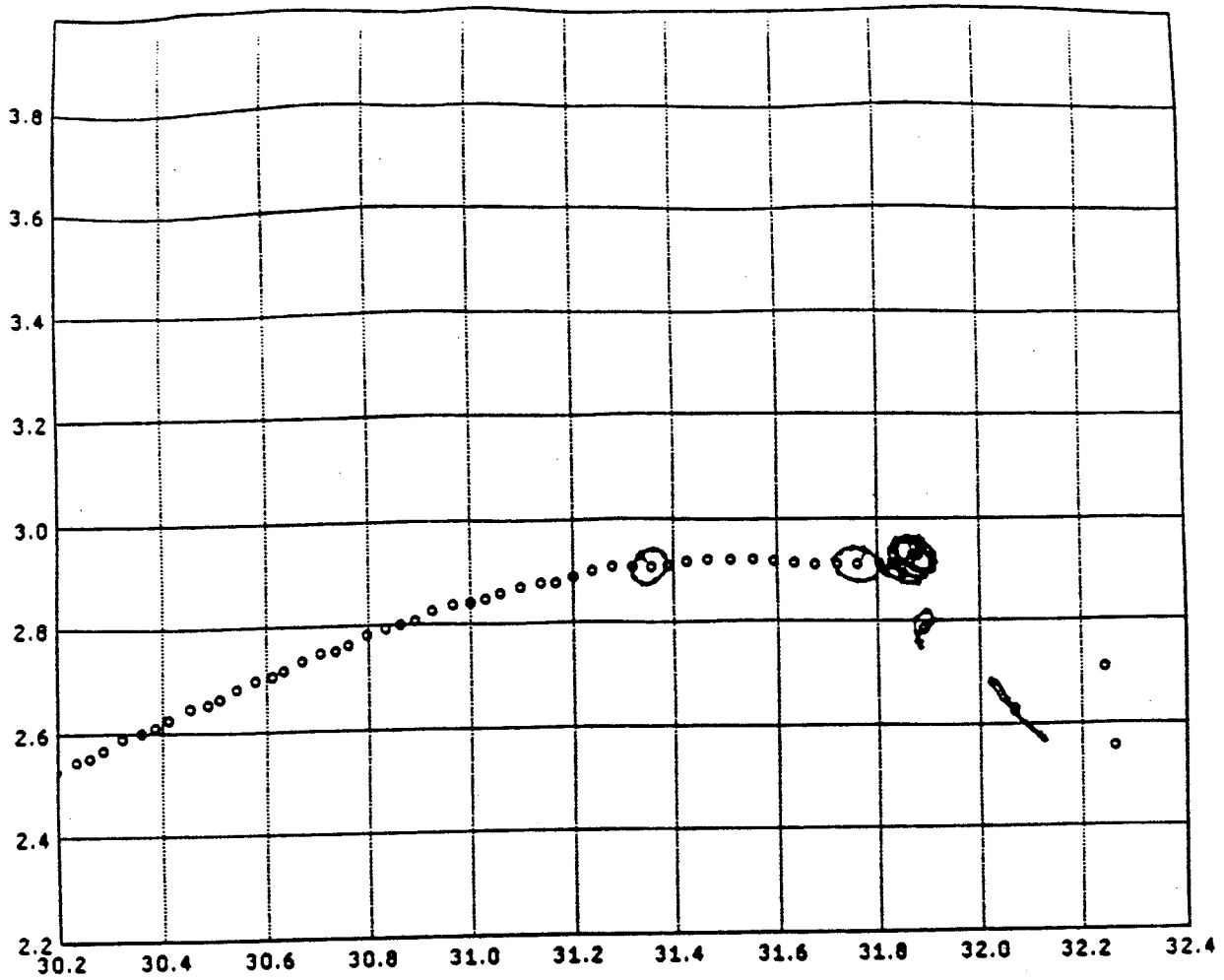

ellipses start at 44.5 MeV

Fig. II.7 Pr vs. R for the central ray starting at to=205 degrees with a first harmonic extraction bump of 1.0 gauss at 275 degrees. These plots are made at an azimuth of 60 degrees.

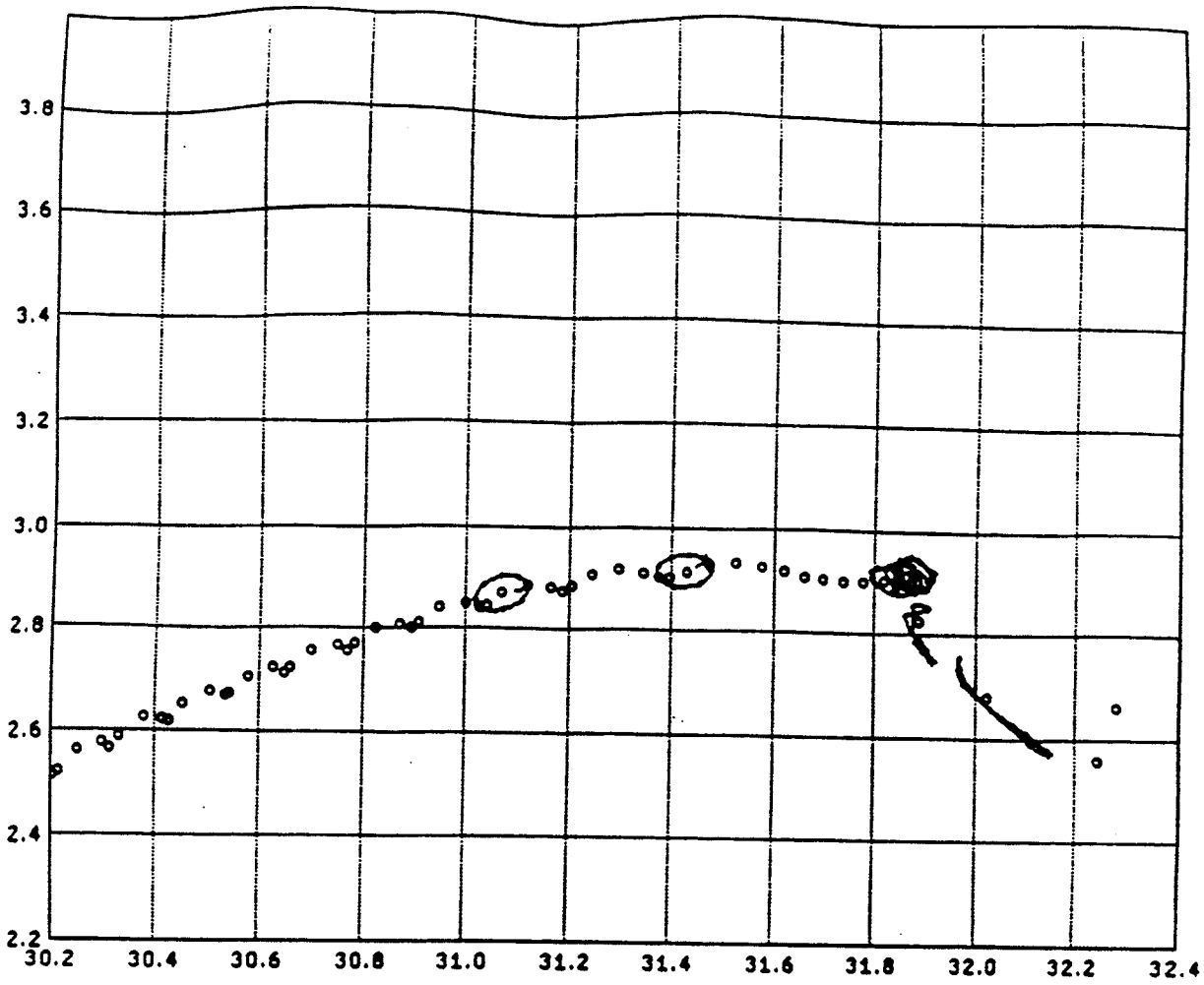

Fig. II.8 pr vs. R for the central ray starting at to=190 degrees with a first harmonic extraction bump of 1.0 gauss at 275 degrees. These plots are made at an azimuth of 60 degrees.

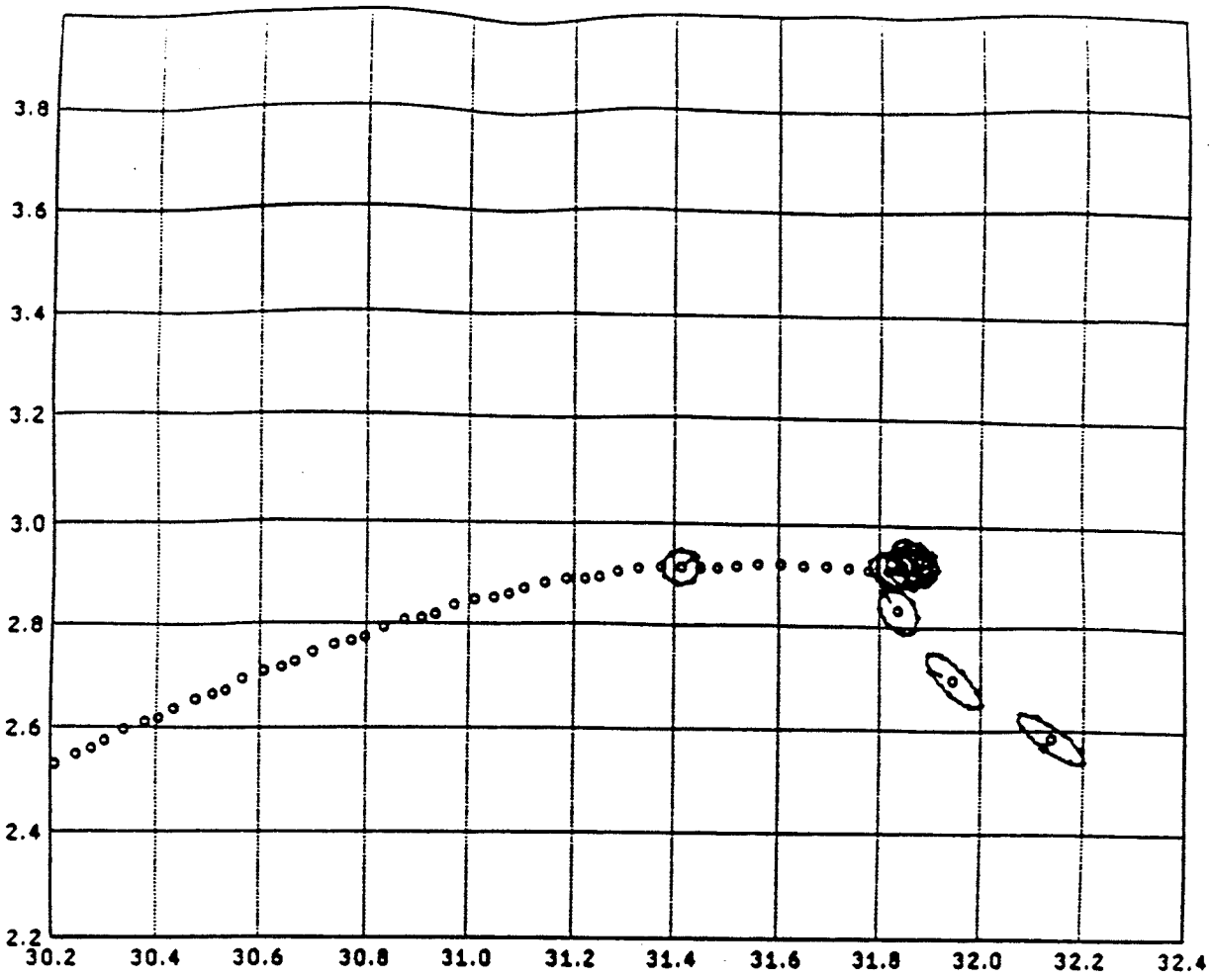

Fig. II.9 Pr vs. R for the central ray starting at to=220 degrees with a first harmonic extraction bump of 1.0 gauss at 275 degrees. These plots are made at an azimuth of 60 degrees.

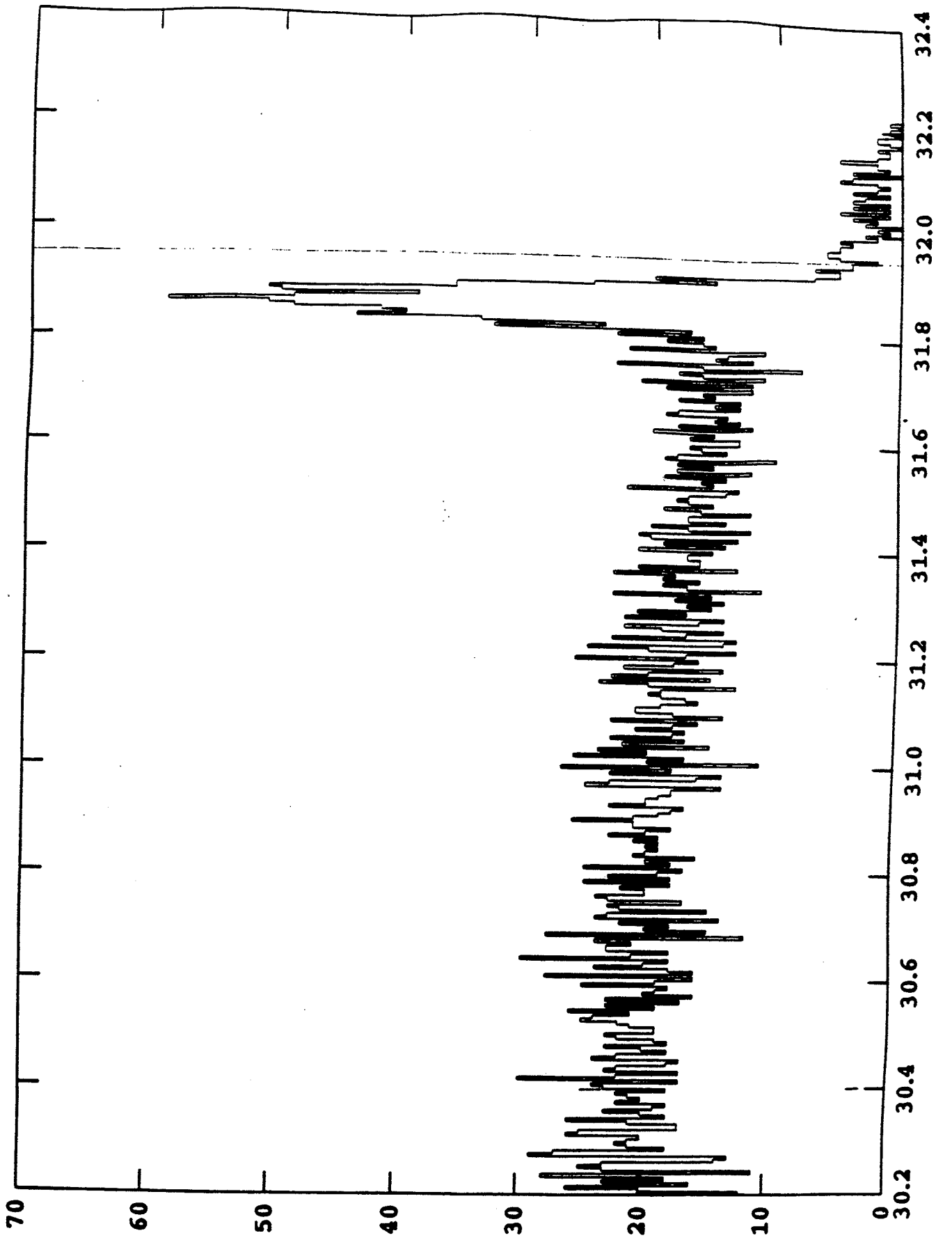

Fig. II.10 Histogram showing the radial distribution in 5.55 mils/channel bins at an azimuth of 60 degrees. Median plane rays, Rseptum=31.949 inches.

119 rays

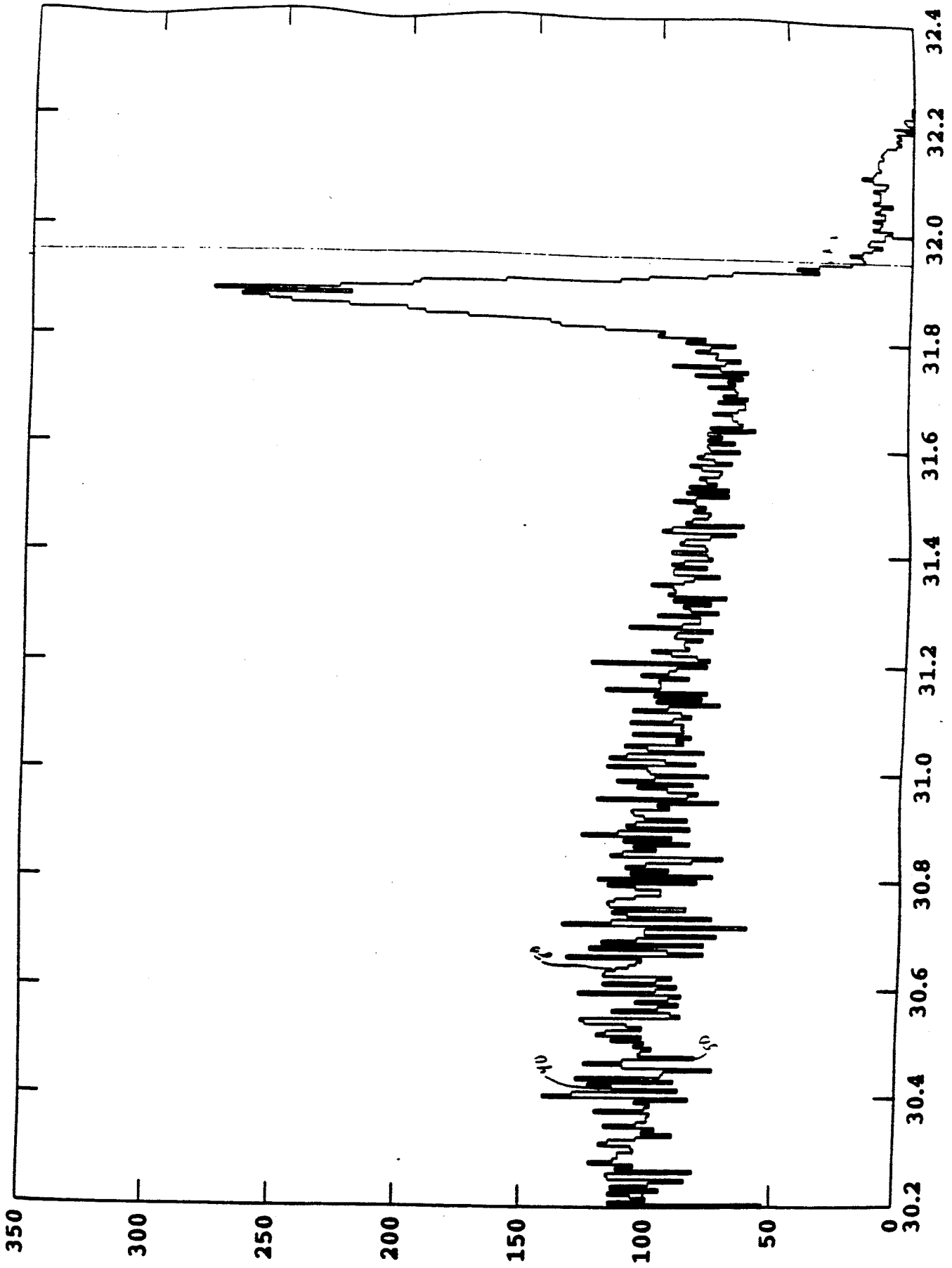

Fig. II.11 Similar to Fig. II.10 but includes the particles off the median plane.

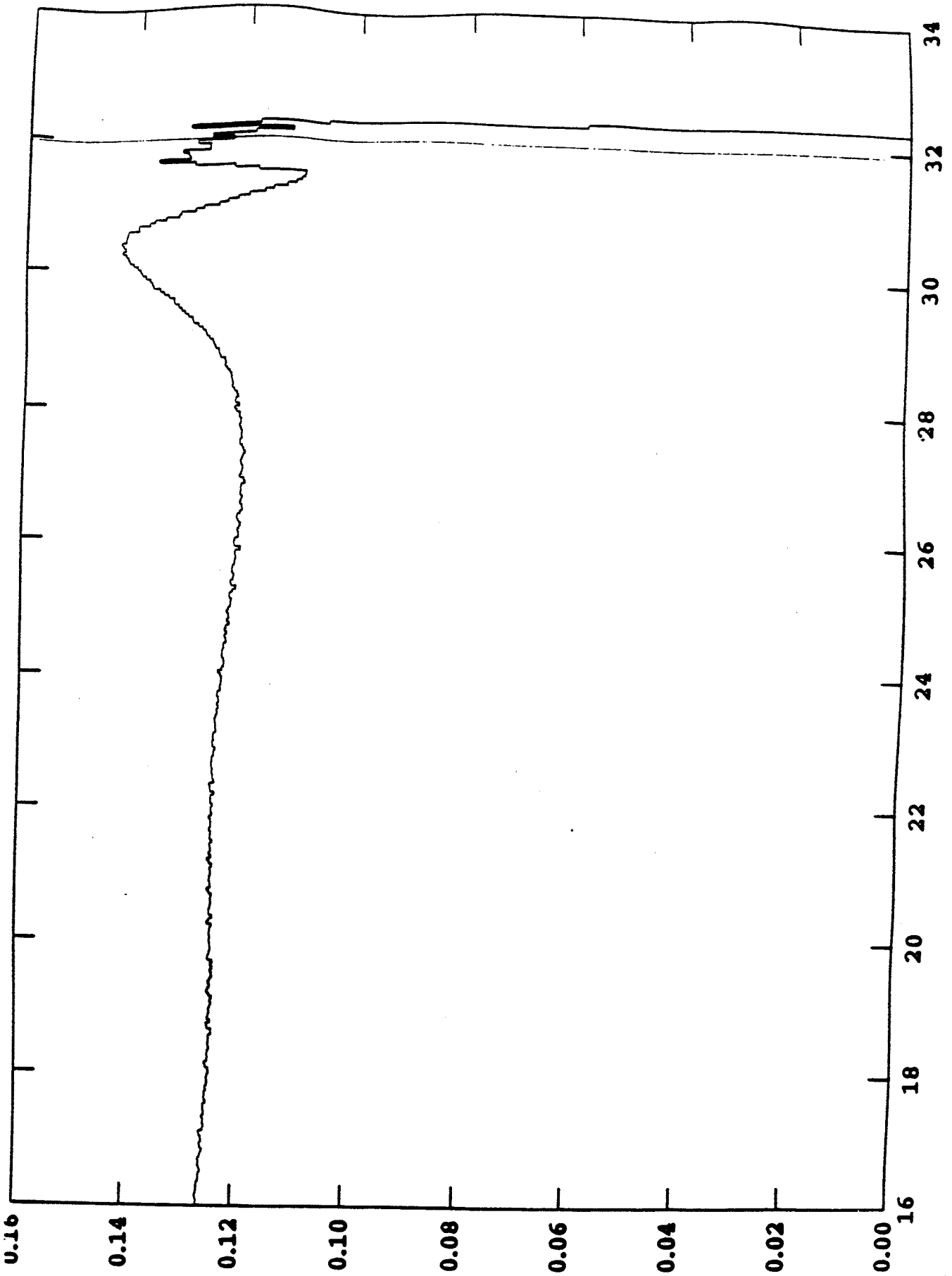

Fig. II.12 Maximum z as a function of radius (all azimuths) Rseptum=31.949 inches.

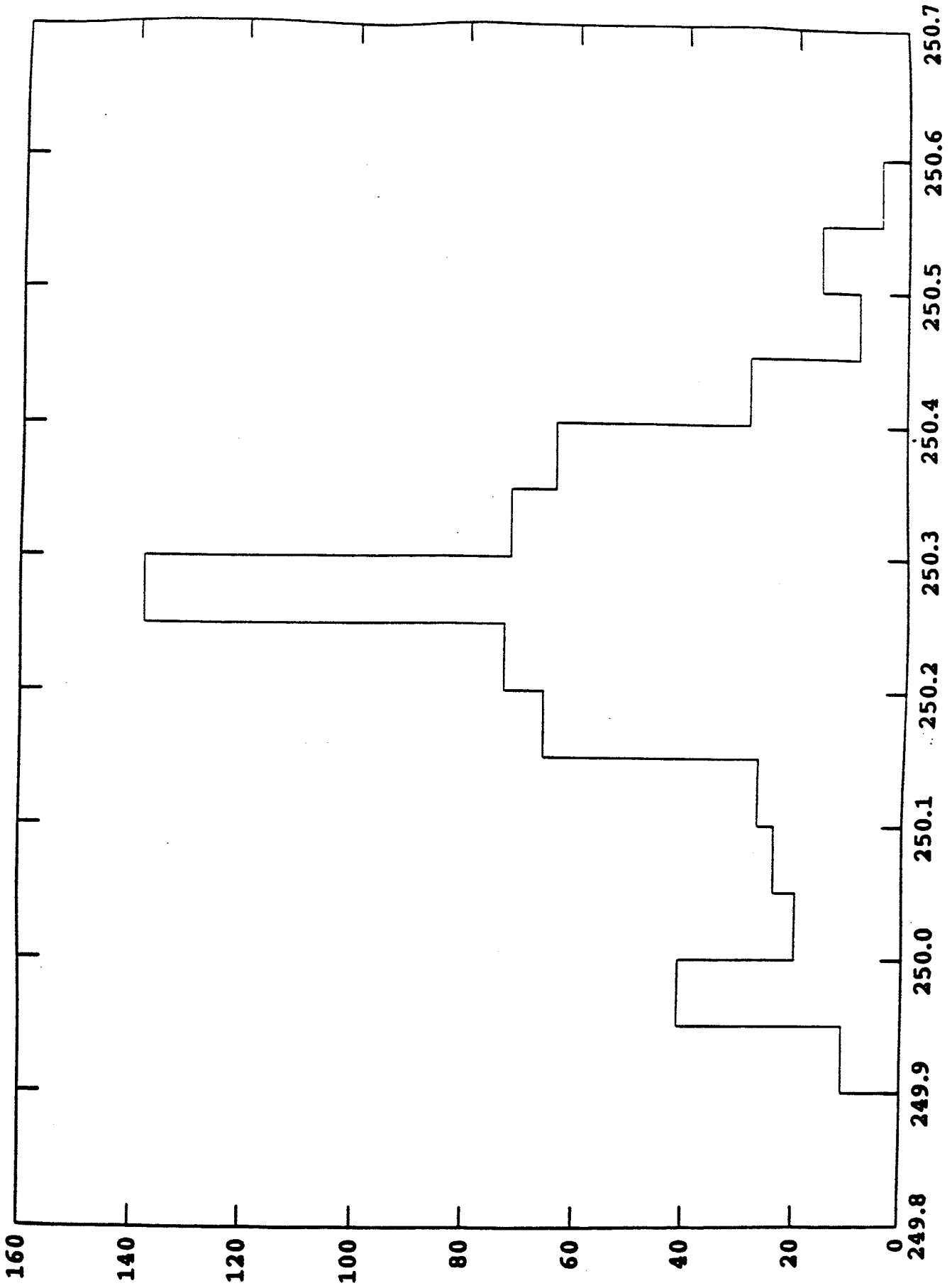

Fig. II.13 Histogram showing energy distribution of the rays which have passed the septum radium (31.949 inches)

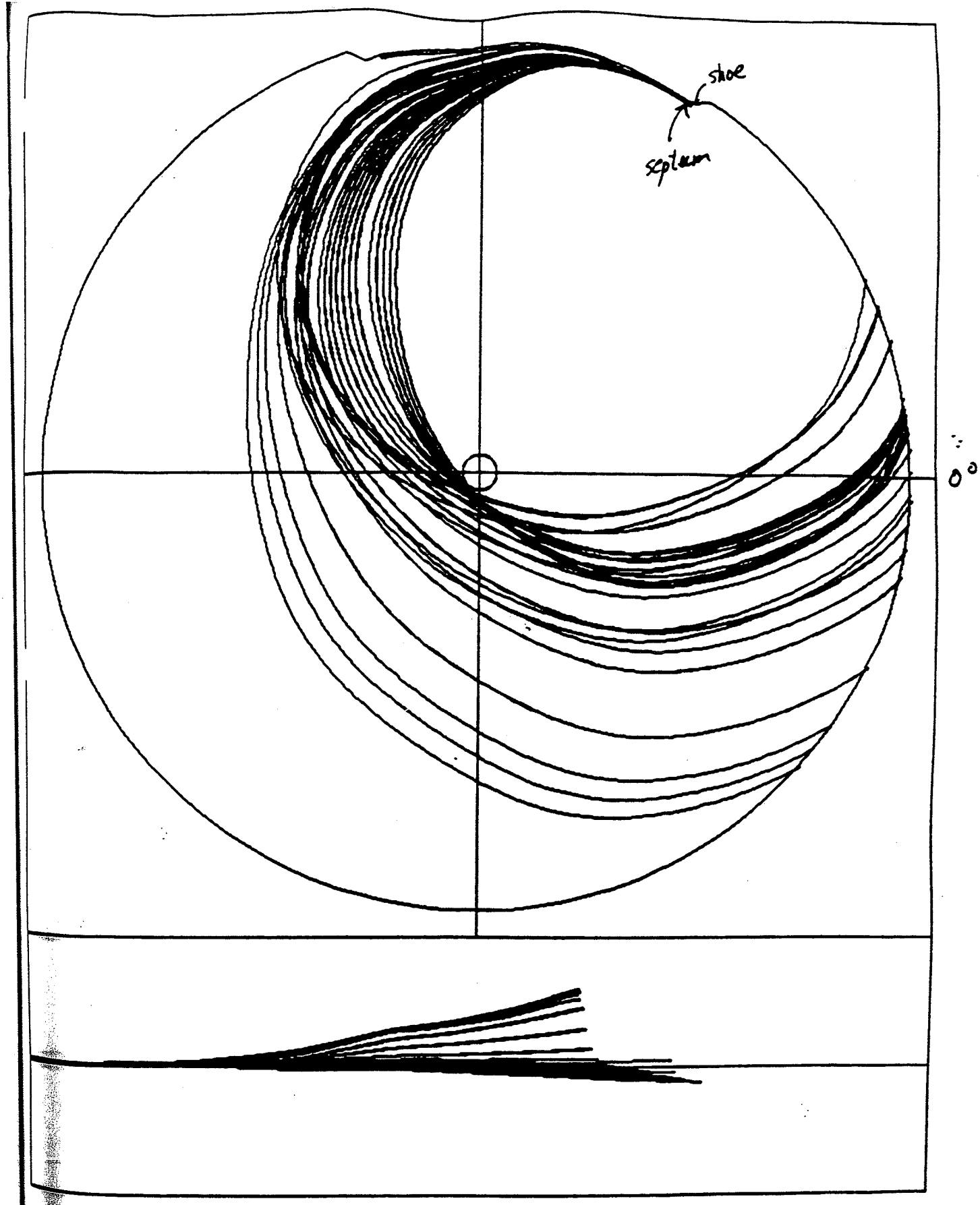

Fig. II.14 Polar plot of the trajectories of the 66 lost rays. The axial behavior is shown at the bottom. Septum thickness is 0.01 inches.

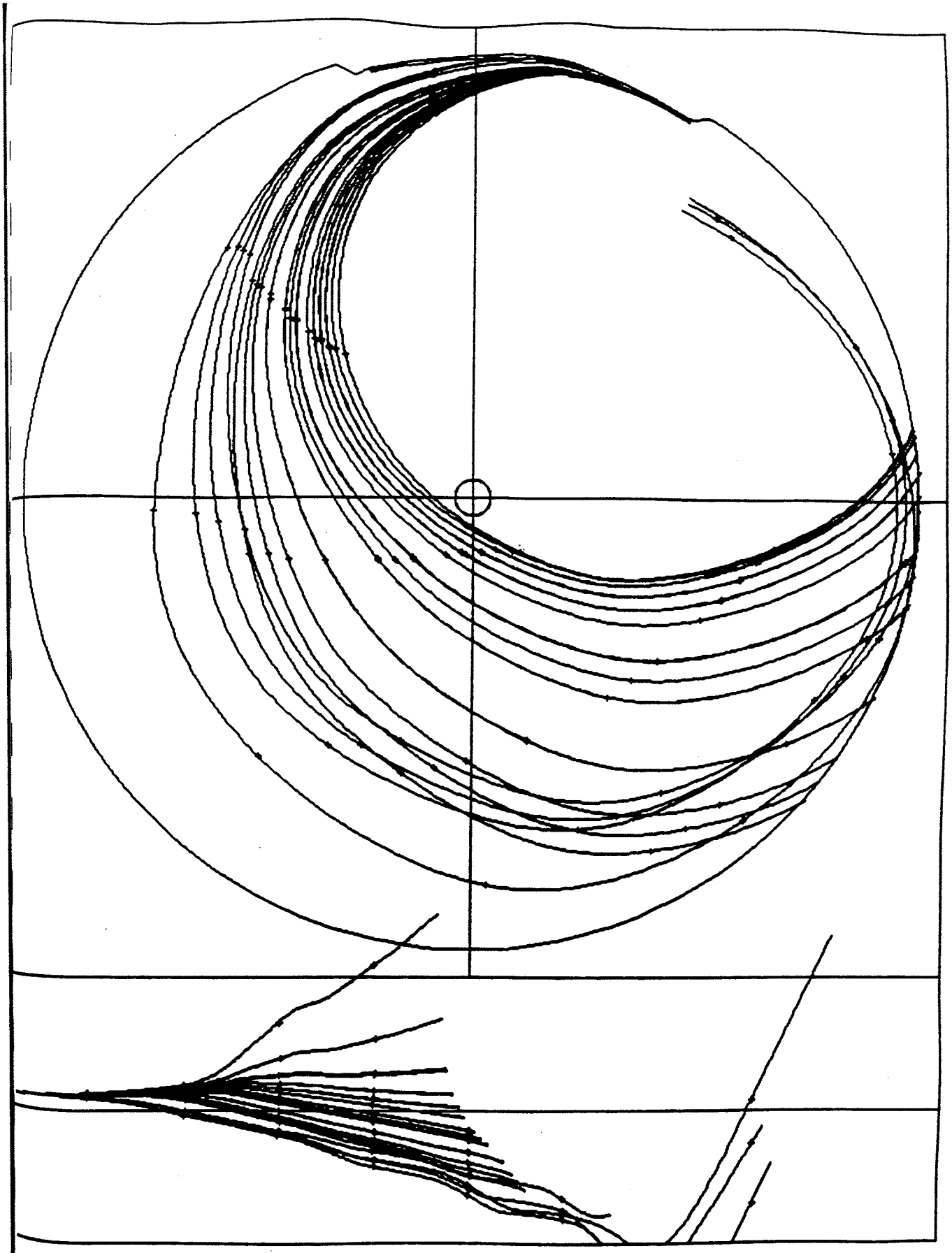

Fig. II.15 Similar to Fig. II.14 but for a septum thickness of 0.005 inches.

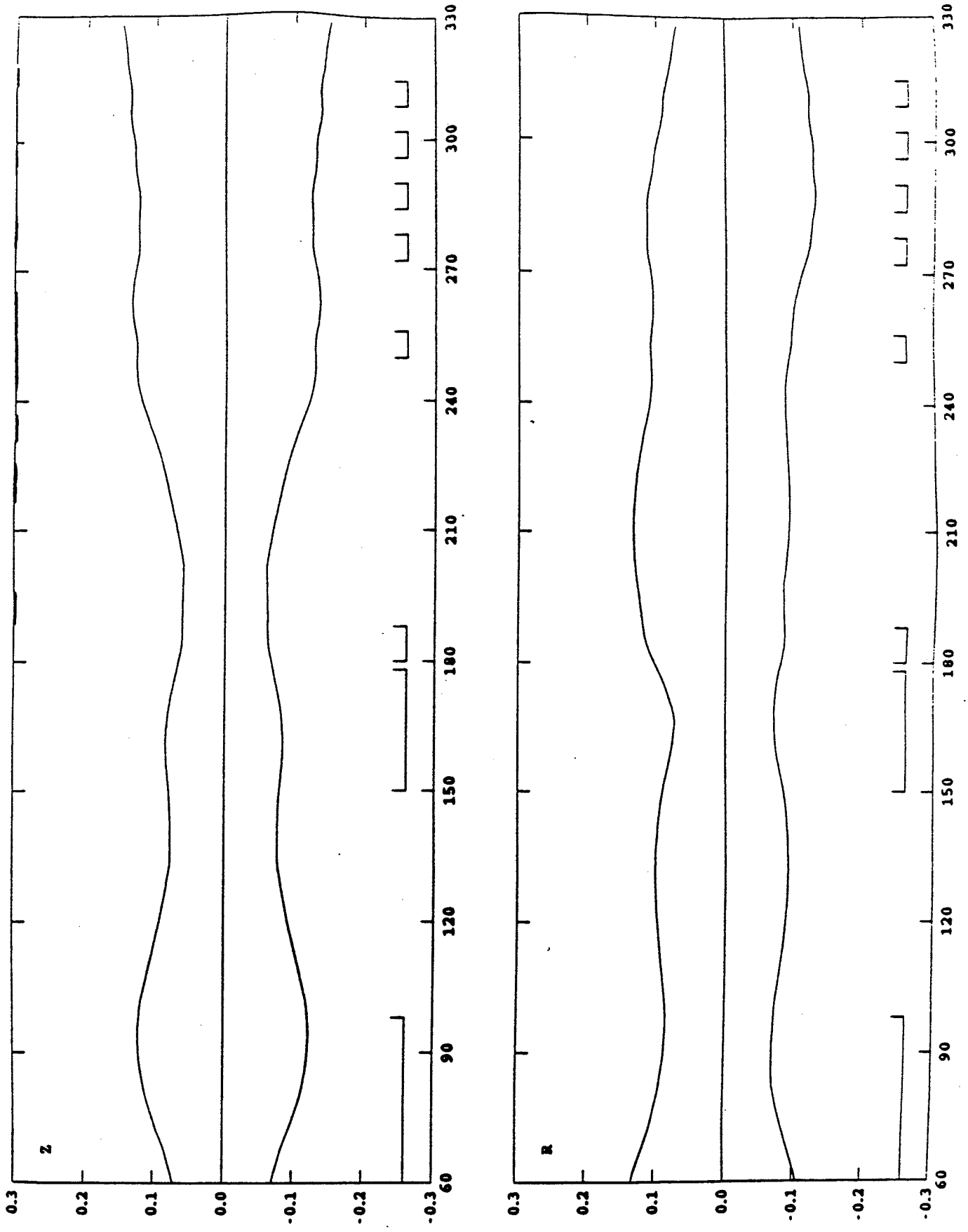

Fig. II.16 Vertical and radial envelope of the 595 rays through the extraction channel.

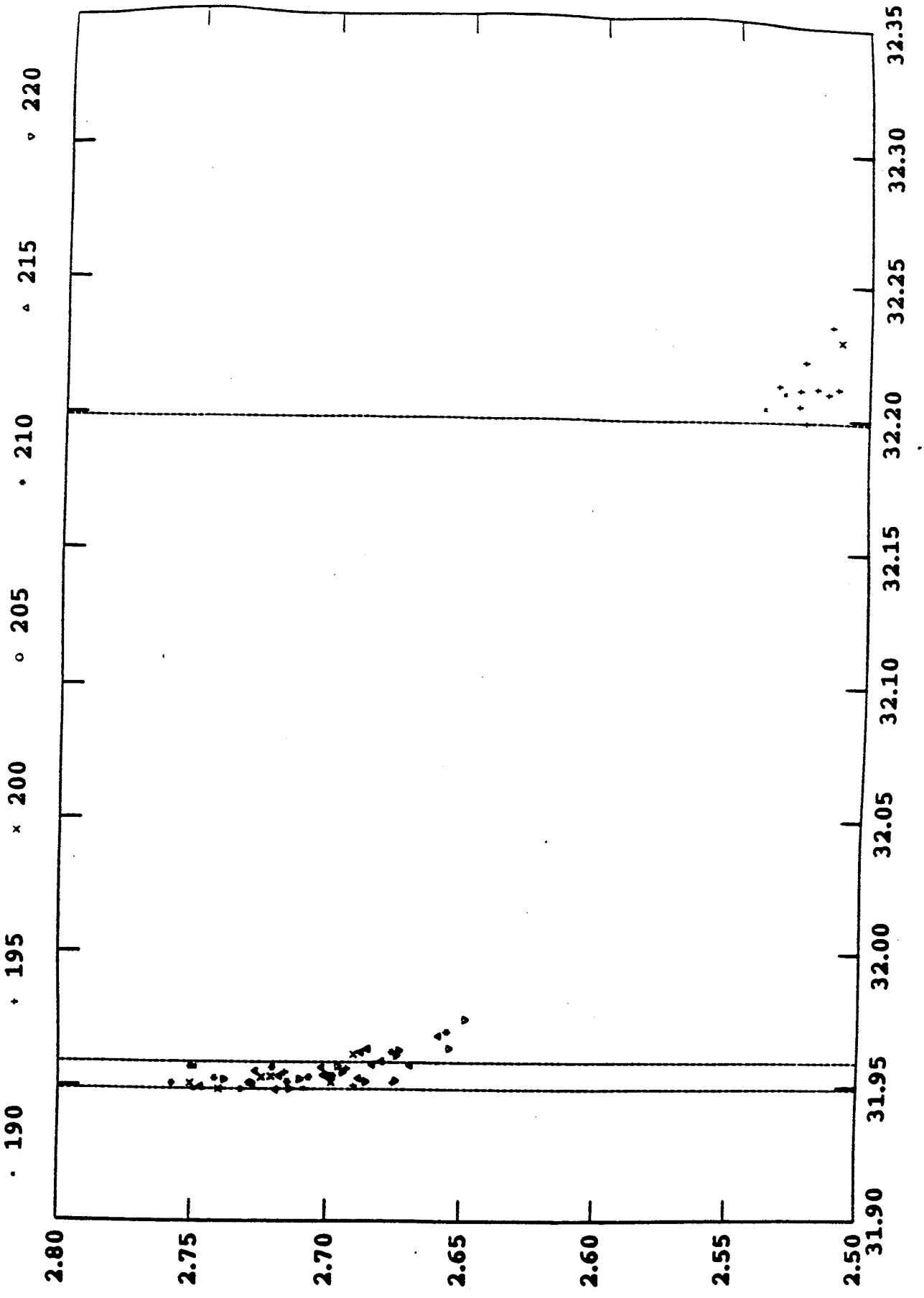

Fig. II.17 Pr vs. R plot at the deflector entry angle. Rays that hit the large r side of the septum and high voltage electrode are shown. The symbol identifies the starting times. Septum position from median plane ions only.

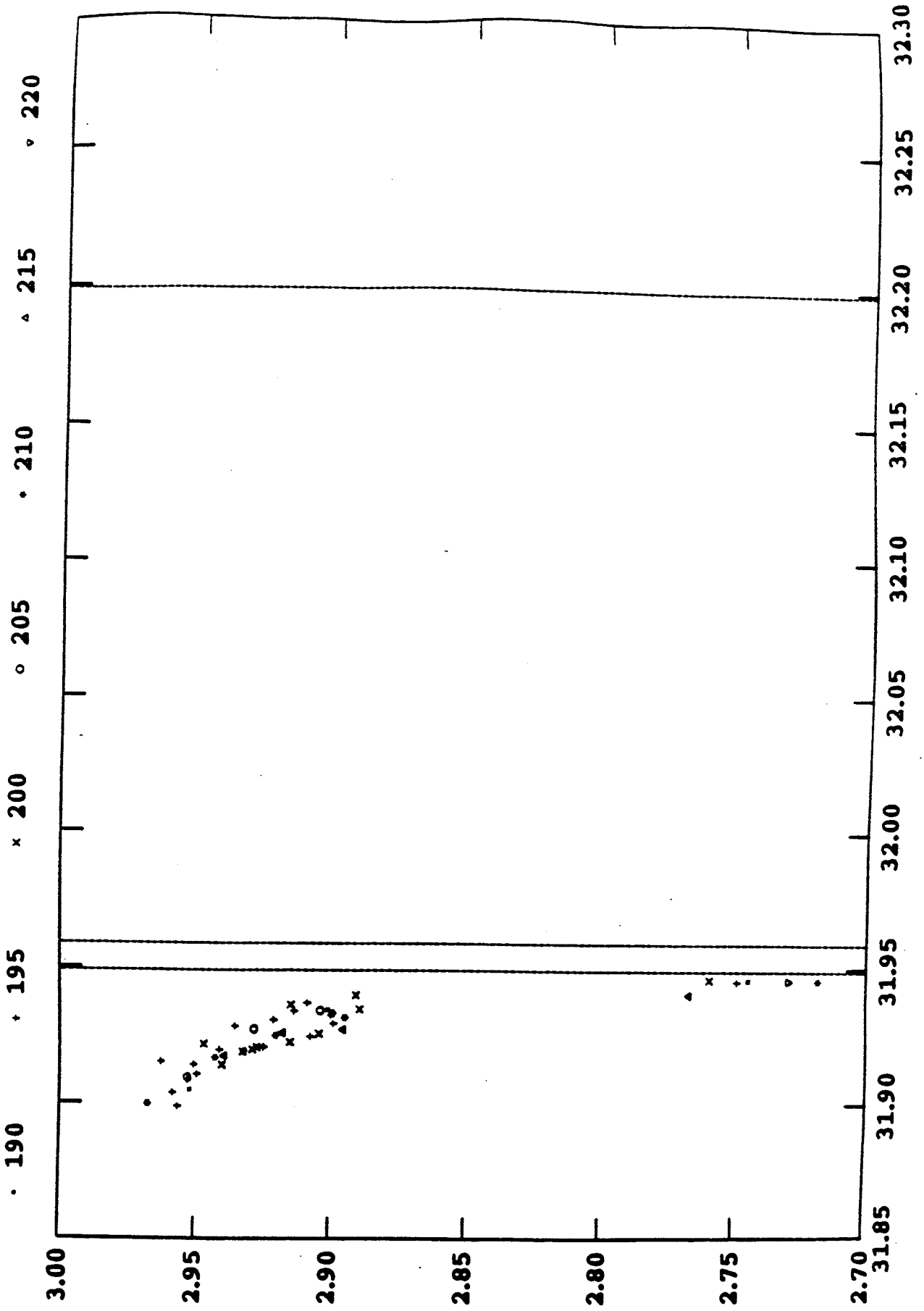

Fig. II.18 Similar to previous figure but shows the ions that hit the low r side of the septum.

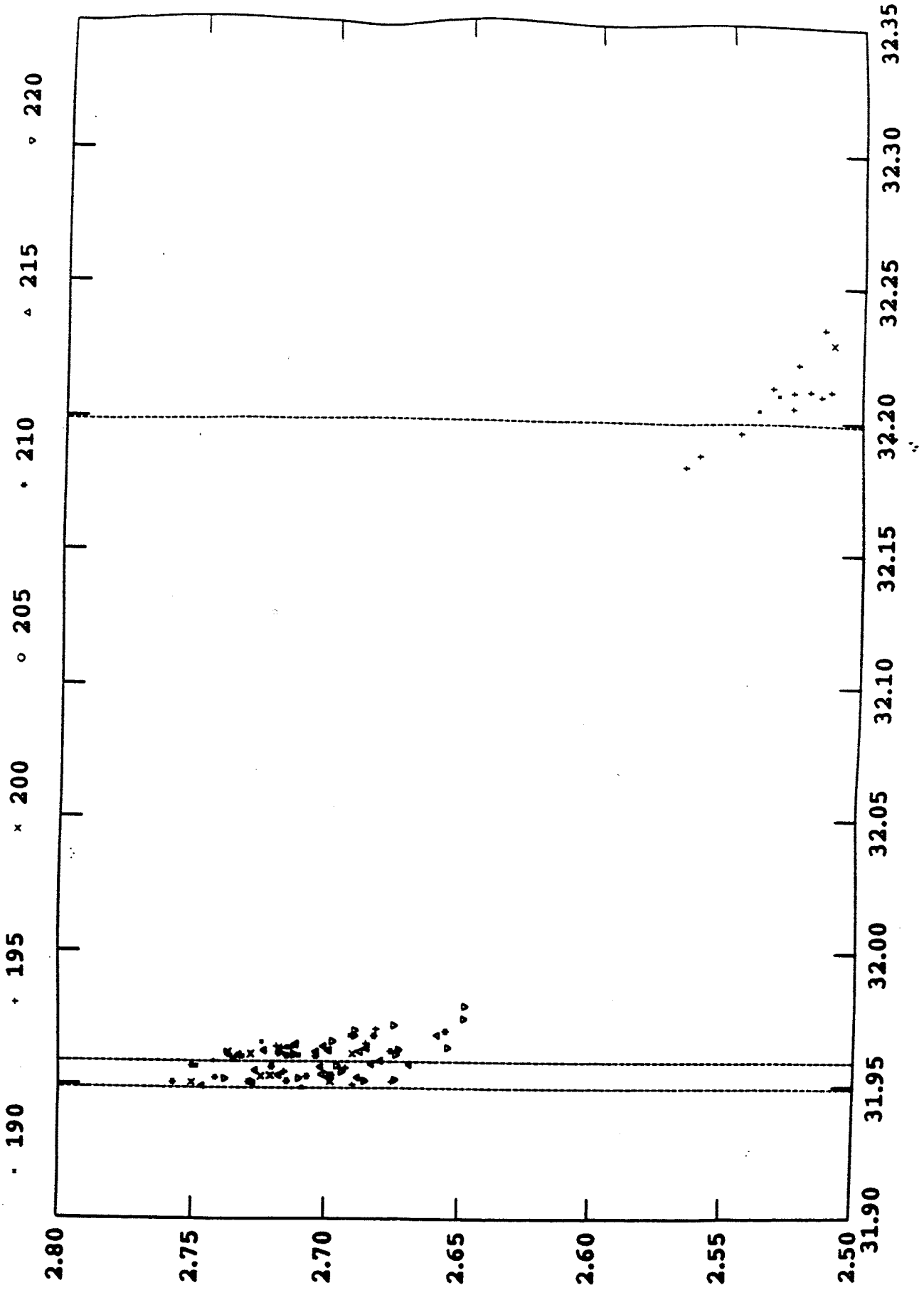

Fig. II.19 Similar to Fig.II.17 but the septum position comes from the Z4 code runs. Deflector electric fields = 140 kV/cm.

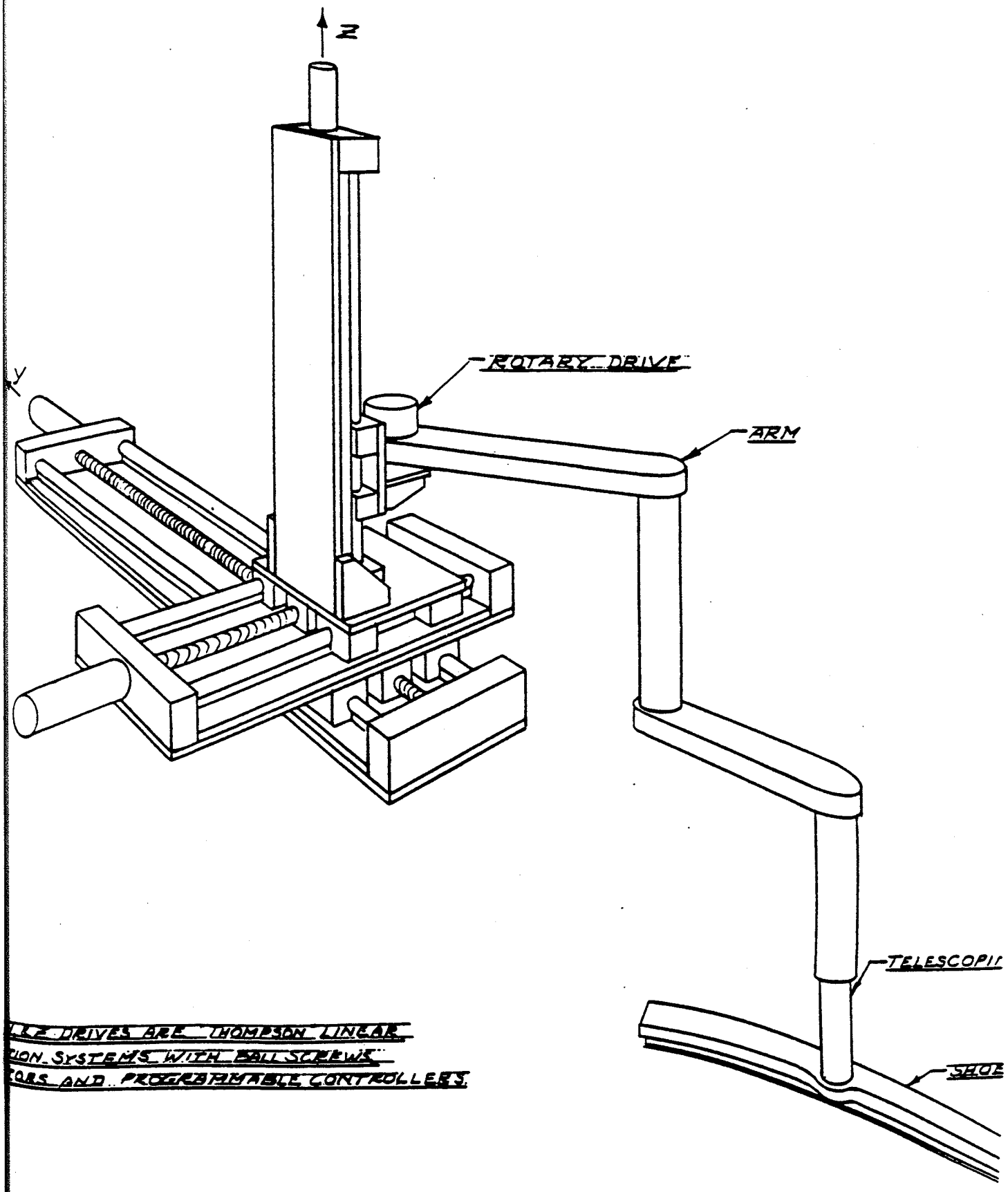

Fig. II.20 Deflector removal by remote handling device.

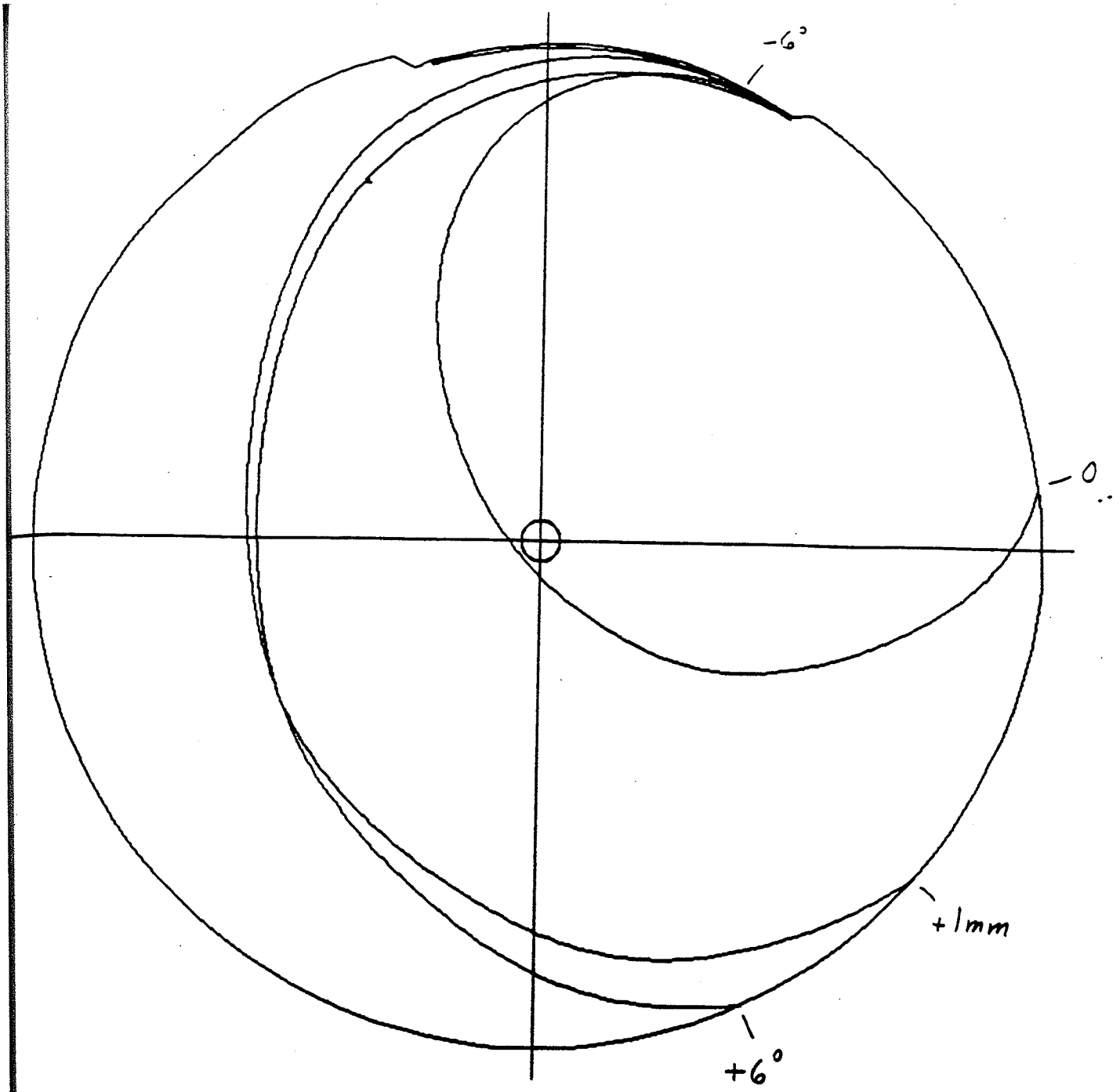

Fig. II.21 Simulation of particles lost by scattering inside the septum.

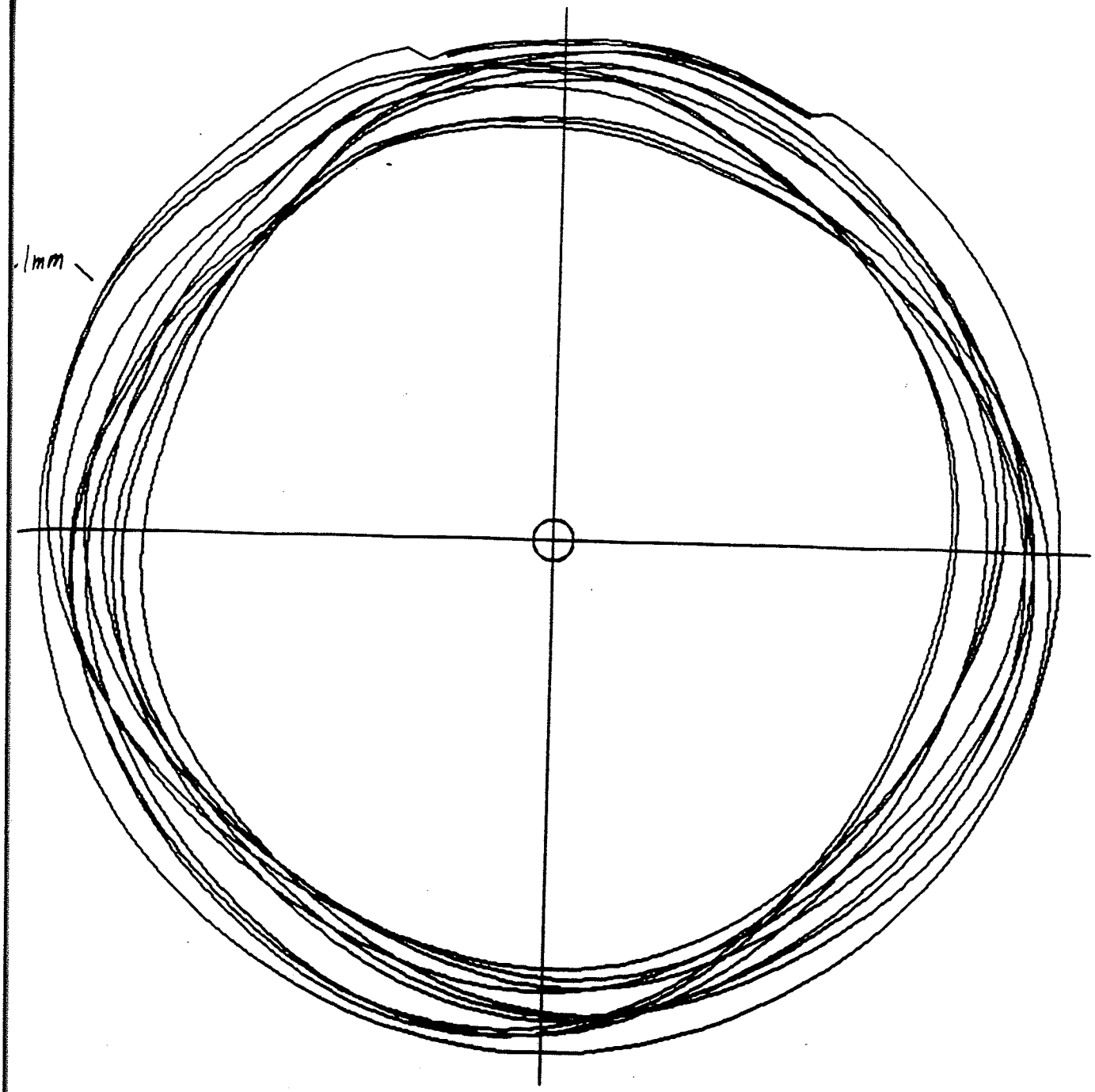

Fig. II.22 Similar to the previous figure.

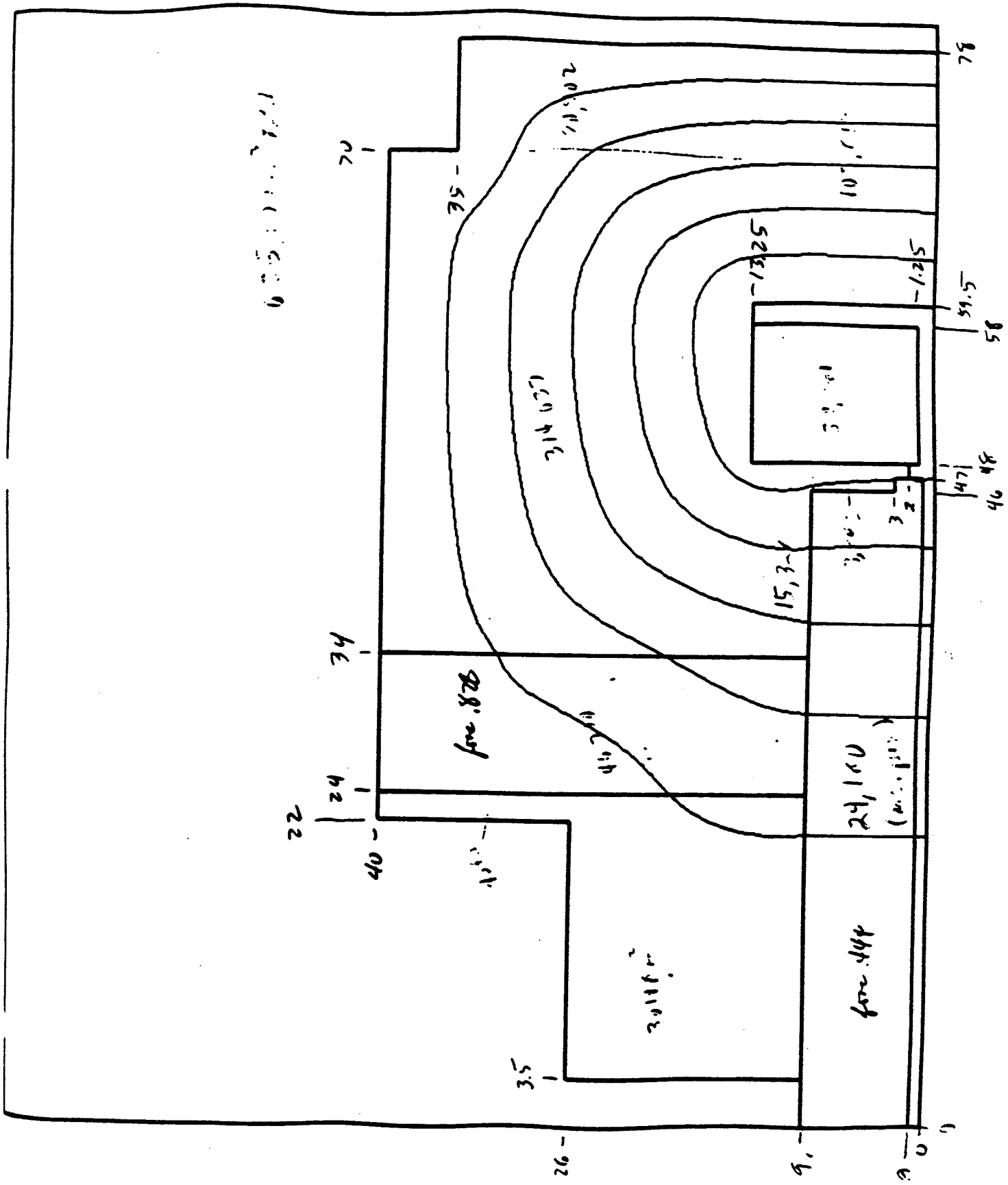

Fig. V.1 Steel distribution for a room temperature compact cyclotron study.

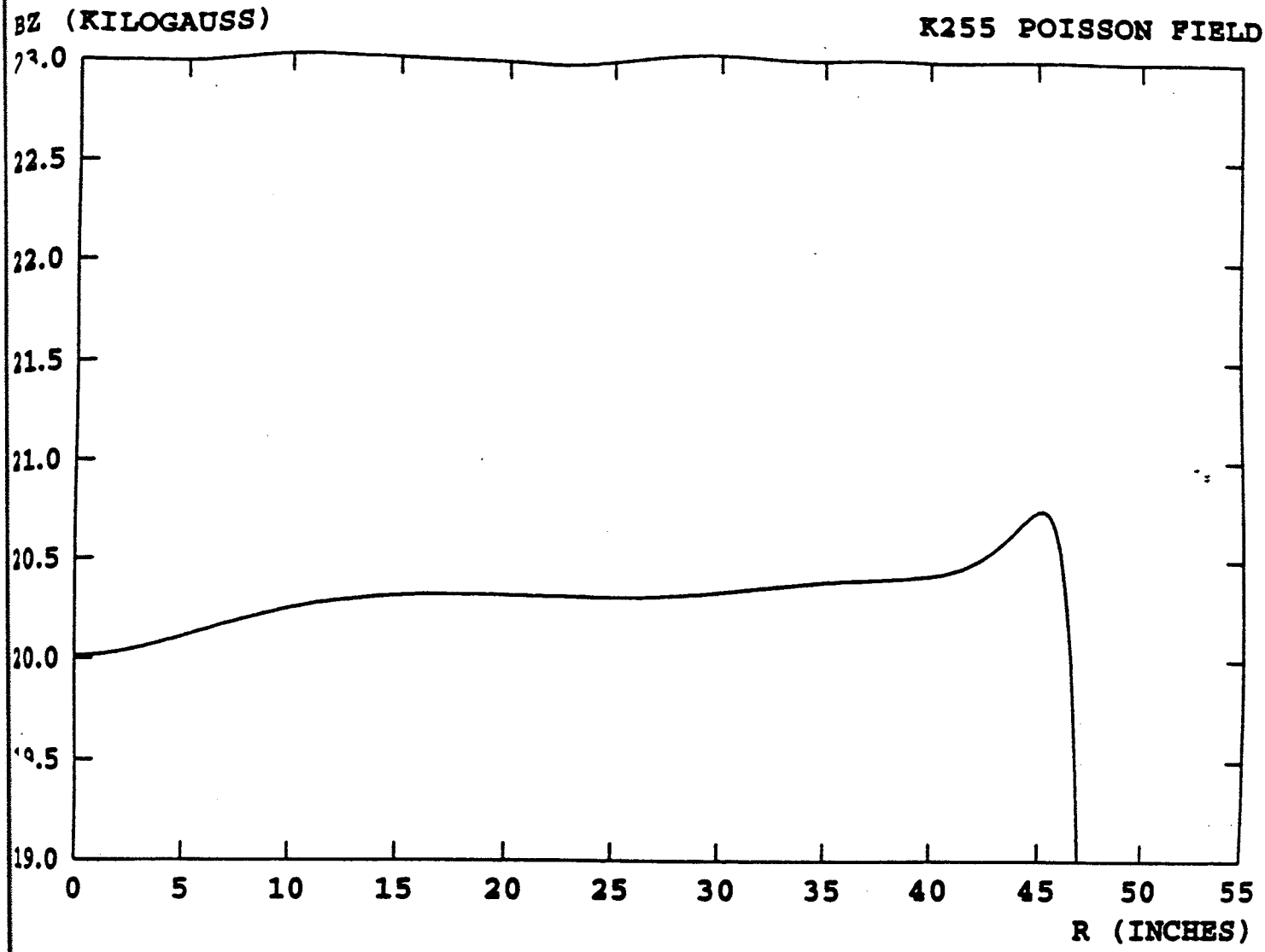

Fig. V.2 Average magnetic field for the model of the previous figure (2400 A/in2).

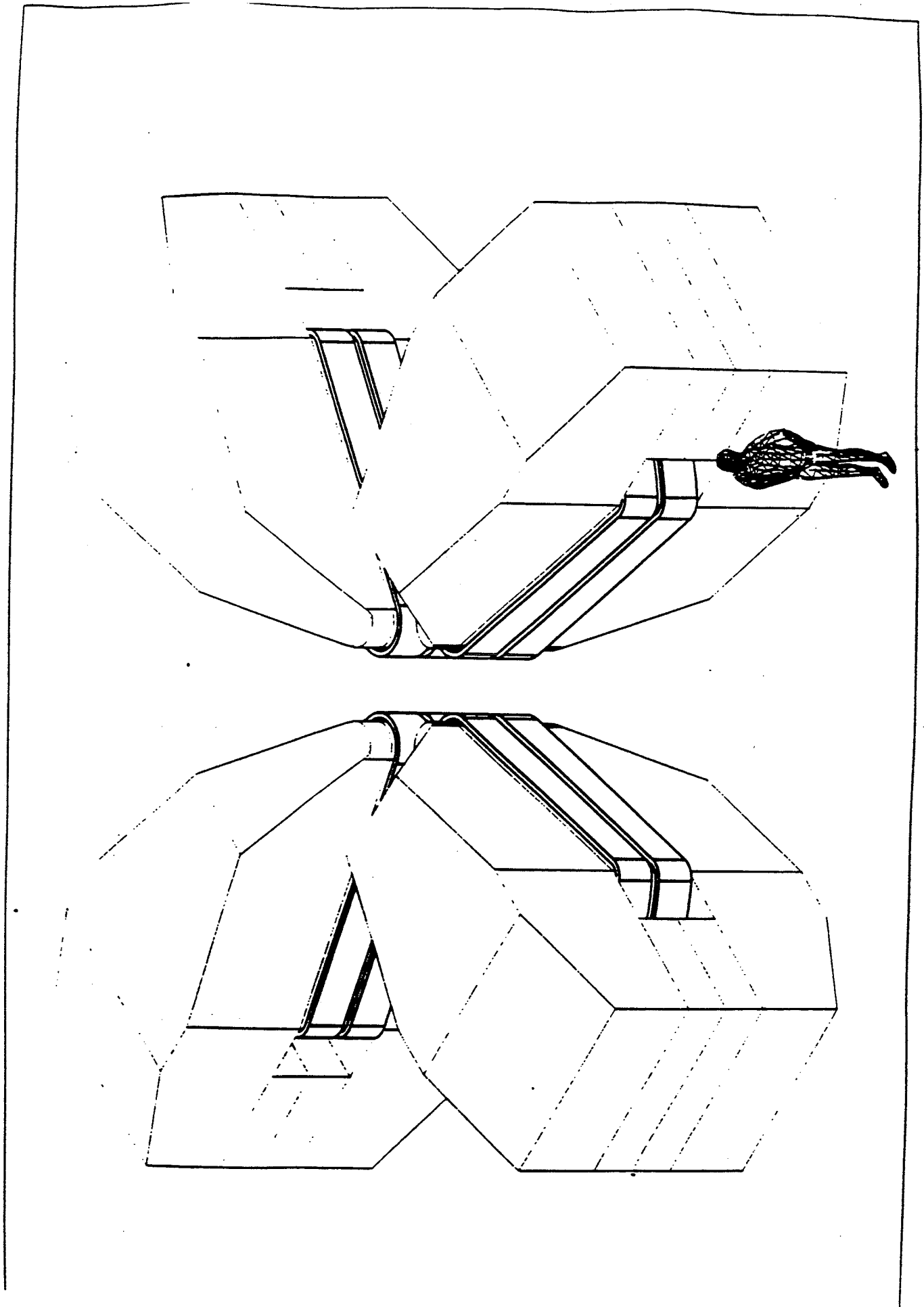

Fig. VI.1 Perspective view of the SSC magnet configuration.

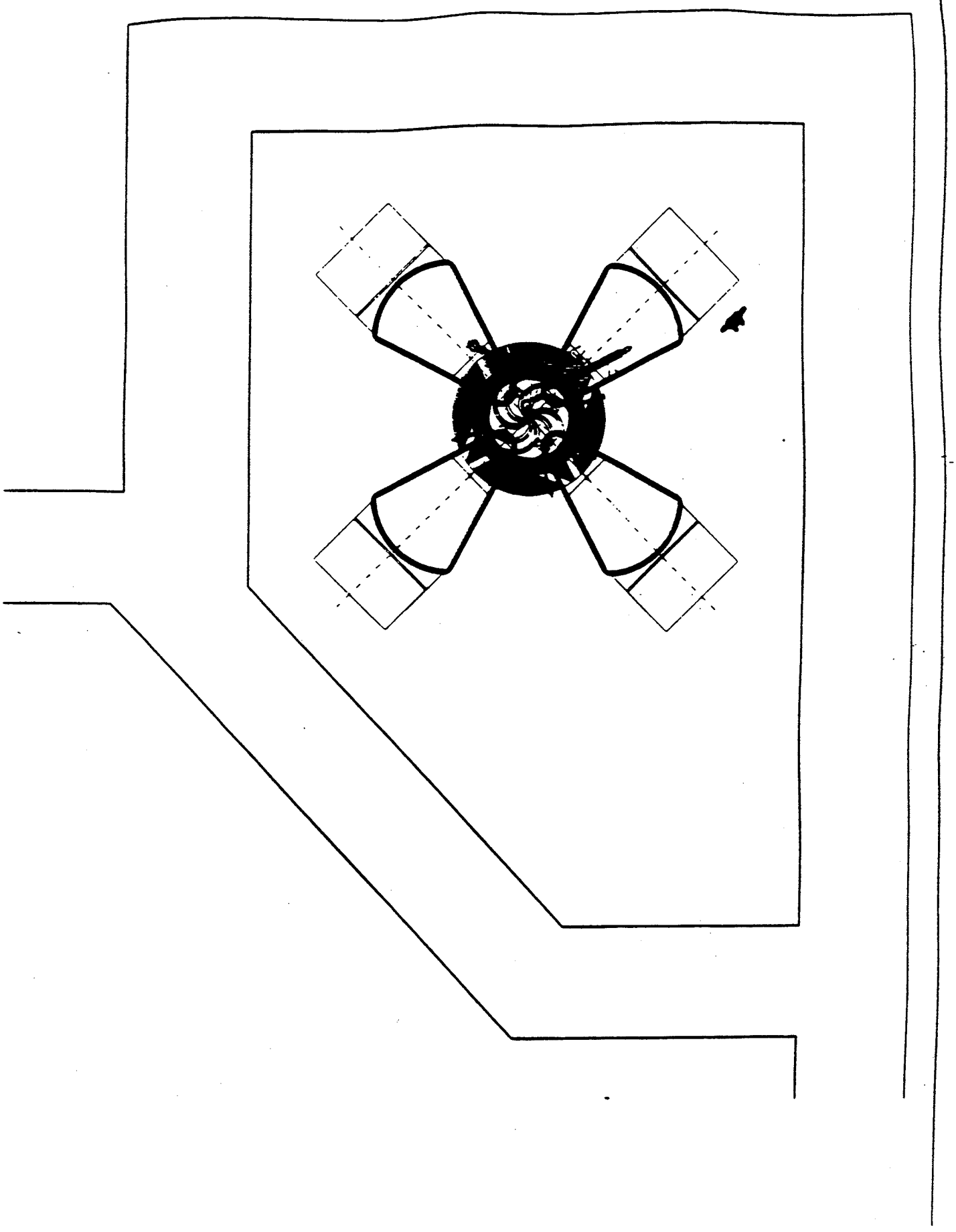

Fig. VI.2 Plan view of the CSC and SSC in room C110.

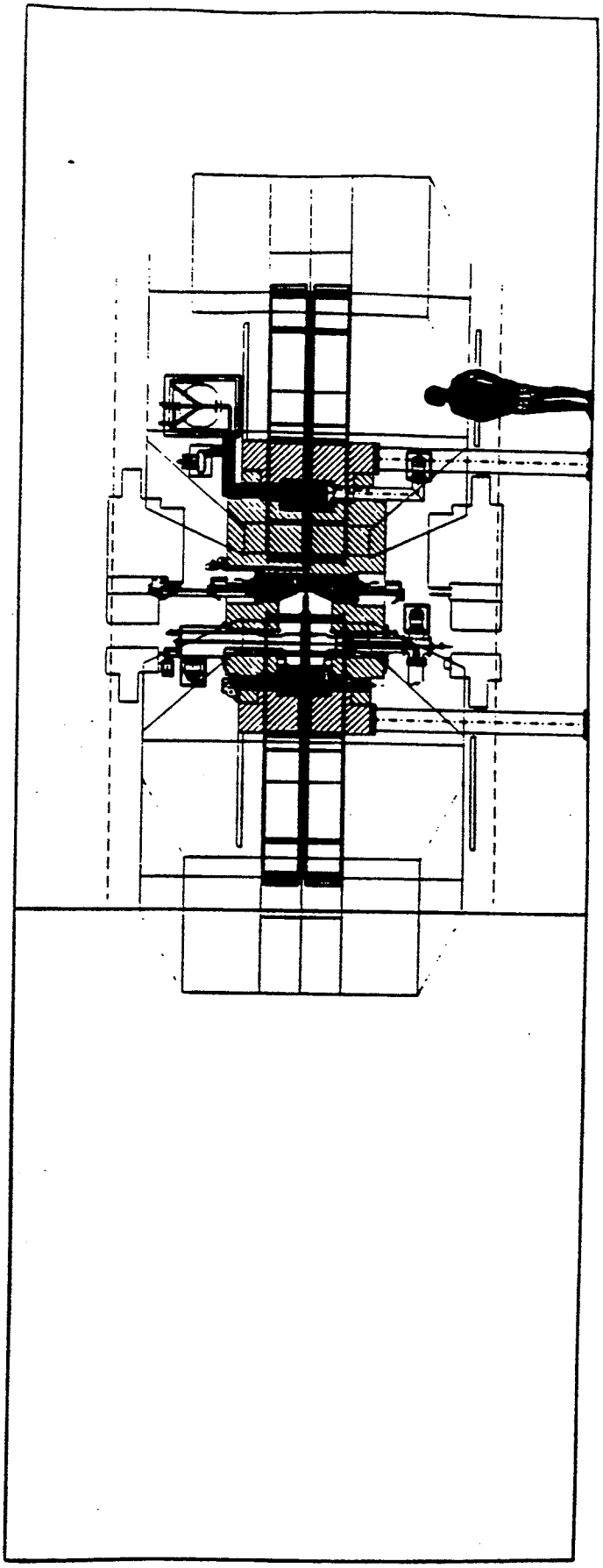

Fig. VI.3 Vertical view of the CSC and SSC in room C110.

Appendix

MSUCLI-874

Section III	pages 13-68
Section V	pages 73-82

Proposal for a

Manufacturing Prototype

SUPERCONDUCTING CYCLOTRON

for Advanced Cancer Therapy

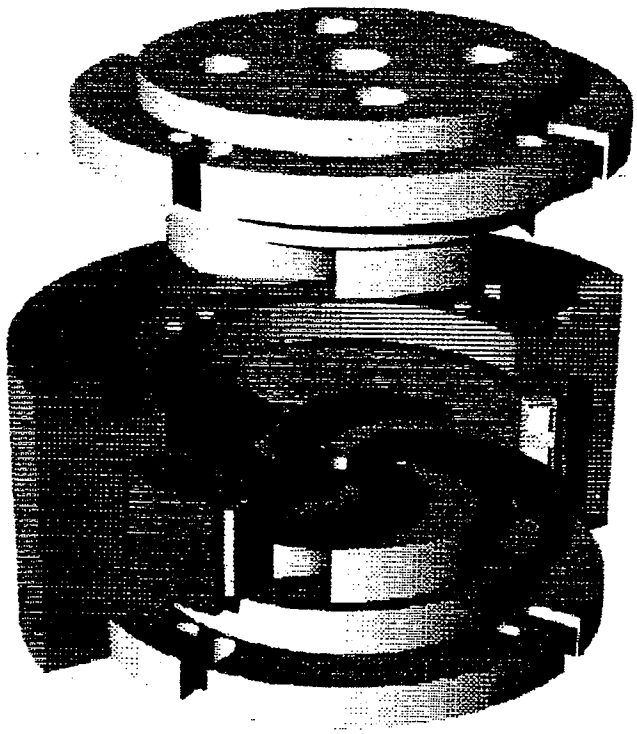

National Superconducting Cyclotron Laboratory

Michigan State University

February 1993

MSUCL--874

Chapter III

THE 250 MEV SUPERCONDUCTING CYCLOTRON

This chapter describes the design of the 250 MeV proton cyclotron. The design incorporates important features from previous MSU/NSCL cyclotrons, i.e. single turn extraction[30] as utilized in the K50 cyclotron to reduce beam losses and residual radioactivity, superconducting coils as used in the K500 and K1200 cyclotrons[31] to reduce the overall size and cost of the cyclotron, and pulsed operation as utilized in the K100 medical cyclotron in order to minimize power consumption[32]. The design calculations and mechanical layouts have been carried considerably further than in any of our previous proposals, and typically have the level of detail that would be customary in a Conceptual Design Report for the Department of Energy. The design work insures that all the desired performance characteristics can be successfully accomplished in a single cyclotron and that the resulting cyclotron will be an extremely effective and efficient system for achieving the desired end product, namely, proton beams of energy 250 MeV at currents of up to 10 nanoamps with outstanding beam quality. The depth of detail in the design also allows a "bottoms-up", component by component, cost estimate which is a much more accurate estimating procedure than is available from estimates based on scaling relative to similar projects or from looking at large components only. (The cost estimate is presented in chapter V of this proposal.)

A schematic view of the proposed cyclotron was given in the Introduction (Figure I.1). Major features of the cyclotron follow the general style of presently operating superconducting cyclotrons with a 'pill-box' yoke encompassing the full exterior periphery of the cyclotron, with access to internal components available by raising the upper pole of the cyclotron or lowering the lower pole, using a built-in jacking system. Figures III.1 and III.2 give main vertical and horizontal section views of the cyclotron. The two sections show the spatial relationship of major elements of the cyclotron including the four hills and valleys ('sectors') of the magnet, the pole tip spiral, the main coil and cryostat,

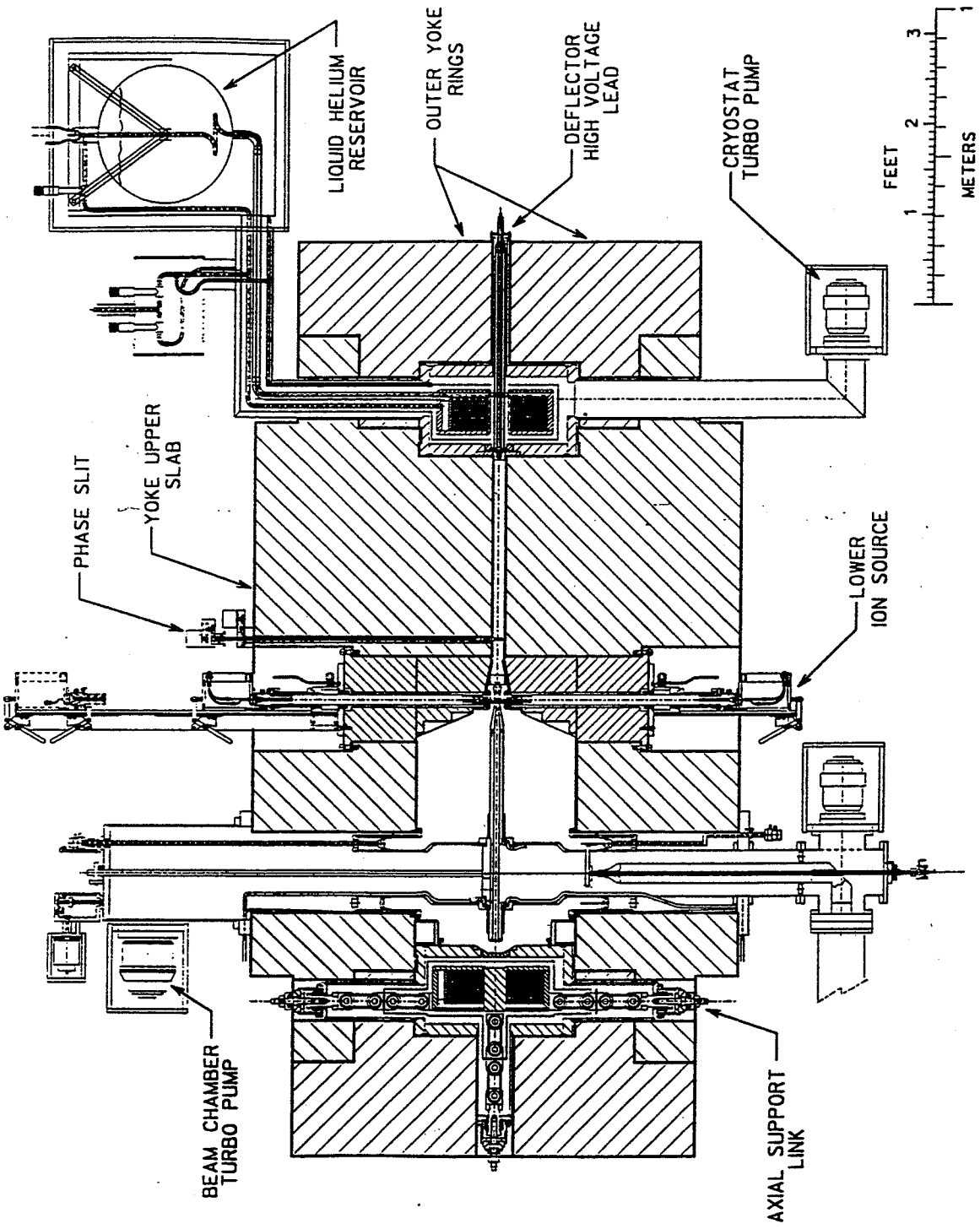

Figure III.1: Vertical section view through the superconducting cyclotron. On the left of the central ion source, the section follows the center line of a magnet valley, on the right the center line of a hill.

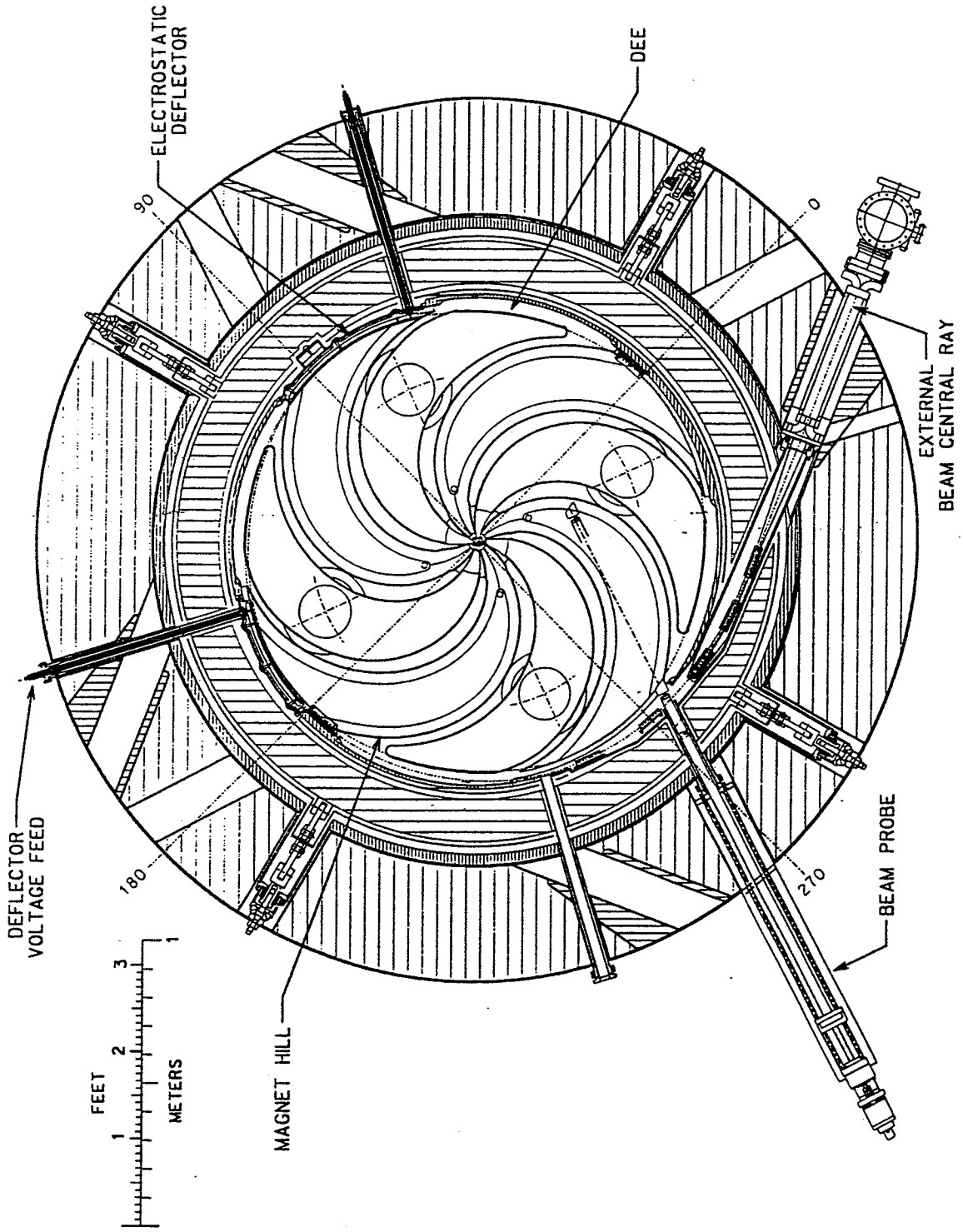

Figure III.2: Horizontal section view of the 250 MeV proton therapy cyclotron showing the arrangement of main components. Magnet hills and dees repeat with 90 degree spacing.

the dee in each valley of the magnet, the double stem configuration on each dee, the ion source, the extraction channel, etc.

Selection of a four sector design rather than three sectors as used in other MSU cyclotrons, results from a fundamental property of isochronous cyclotrons namely that the radial focussing frequency increases with radius (or energy) approximately as the mass of the accelerated particle, i.e.

$$\nu_r \approx \gamma = \frac{1}{\sqrt{1-(\frac{v}{c})^2}}$$

The factor v/c will be higher in the 250 MeV cyclotron than in previous MSU cyclotrons thus giving a higher ν_r; a four sector magnet comfortably avoids the region of violently unstable orbits which occurs if the radial focussing frequency reaches the value N/2 (where N is number of sectors in the magnet), since $4/2 = 2$, whereas this instability would be very difficult to avoid in a 250 MeV three sector cyclotron where $N/2 = 1.5$.

The four-sector, four dee configuration is well matched to the 250 MeV proton requirement on several grounds: 1) as indicated above, the region of unstable orbits (the N/2 stopband) is comfortably above the 250 MeV operating regime, 2) the four dees give a large energy-gain-per-turn which makes 'single-turn' extraction feasible thereby largely eliminating beam loss and induced radioactivity in the cyclotron, 3) the accelerating dees can operate in a natural 'push-pull' mode which greatly simplifies the rf drive system, and 4) with the high energy-gain-per-turn, there is no discernable beam disturbance as the operating point passes near the next most severe resonance at $\nu_r = N/3$.

The overall size of the cyclotron is fixed by the magnetic field strength, which in this cyclotron is low compared to the fields used in other MSU superconducting cyclotrons (a field of 2.38 Tesla at r=0 vs. 4.6 to 4.9 in other MSU superconducting cyclotrons). It is of course desirable to have a strong magnetic field to minimize the size and cost of the cyclotron, but beam extraction becomes more difficult as the field is increased, and stronger spirals must also be used to offset the decreased fractional azimuthal variation of the field (the "flutter"). For this medical cyclotron design, we have then selected a magnetic field which reduces the electric field needed in the extraction system relative to the values required in the K500 and K1200, since design electric fields have been difficult to achieve with good reliability in those cyclotrons. The resulting design for the overall cyclotron is both conservative and highly cost effective.

With 2.38 Tesla for the field at r=0, the orbital rotation frequency is 36.21 Megahertz, and beam extraction occurs at a radius of 915.6 millimeters, where the average magnetic field is 2.65 Tesla. The peak magnetic field in the hills of the magnet is approximately 3.6 Tesla and the minimum valley field in the operating region is approximately 2 Tesla. If the accelerating system is operated at twice the orbital frequency of the proton beam (the 'second harmonic' mode) a particularly simple resonant configuration occurs in which dees on opposite sides of the cyclotron operate 'in-phase', while the nearest-neighbor dees operate 180 degrees out of phase, i.e. the basic 'push- pull' mode of a conventional two dee cyclotron. Operating in this mode, all dees can be driven from a

single rf amplifier as in the superconducting cyclotron at Chalk River[33].

Following subsections give additional details of the major subsystems of the cyclotron.

III.1 Basic magnetic field and orbit calculations

Designing the magnetic field for a superconducting cyclotron is a successive approximation process which begins with use of a set of well known approximate formulae (the smooth approximation[34]) to select basic dimensions of the magnet. A 'first-try' magnetic field is then computed using a two dimensional relaxation calculation for the sensitive average value of the field, and using a saturated iron approximation to calculate the dependence of the field on the azimuthal coordinate. In the circumstance of a basically cylindrical cyclotron, the assumptions made in this assumed field model are quite good and, in the presently operating superconducting cyclotrons, such calculations have been the complete basis for proceeding with construction of full scale magnets. The calculations given in this proposal use this traditional approximation to calculate the magnetic field; recent advances in the availability of high speed computers and sophisticated three- dimensional relaxation codes make it, however, also now practical to include full three dimensional relaxation calculations as a step in the design process and we will do this as we finalize the magnet design. With such calculations we expect to achieve considerably more accuracy in the initially built magnet than was achieved in our previous cyclotrons (0.1% vs. 1%) so that adjustments to the basic iron configuration will be minimal.

The basic magnet structure used in the initial relaxation calculation is shown in Figure III.3 with some typical field lines superimposed in the region inside the iron. Outside of the magnet isogauss contours for the external magnetic field are shown; the fringe field peak at the corner of the step in the upper pole cap indicates that it would be helpful to move this step to larger radius which will be done as the overall design is finalized. (In order to minimize interactions with other hospital equipment, the quantity of iron in the yoke of the K250 cyclotron is increased relative to other MSU cyclotrons which lowers the fringe field by a factor of 5 to 10 compared to these cyclotrons.) Adding the pole tip field, calculated with the saturated iron approximation, to the field from the relaxation calculation gives the overall median plane field shown in Figure III.4. The spiral structure of the hills, the azimuthal variation from hills to valleys, and the sharp field fall-off at the magnet edge, all show clearly in this Figure.

Basic properties of closed orbits in the calculated magnetic field are given in Fig. III.5, namely, the orbital frequency and the axial and radial focusing frequencies all plotted vs. energy. The orbital frequency is plotted as the dimensionless ratio of the ideal isochronous frequency 'WO' to the actual orbital frequency 'W' at each energy (with unity subtracted to expand the scale). The focusing frequencies 'NU Z' and 'NU R' are similarly plotted as ratios of the actual focusing frequencies to the orbital frequency and are hence also dimensionless. All three of the curves in the Figure are well behaved from the perspective of desired cyclotron performance. The NU R curve rises toward, but does

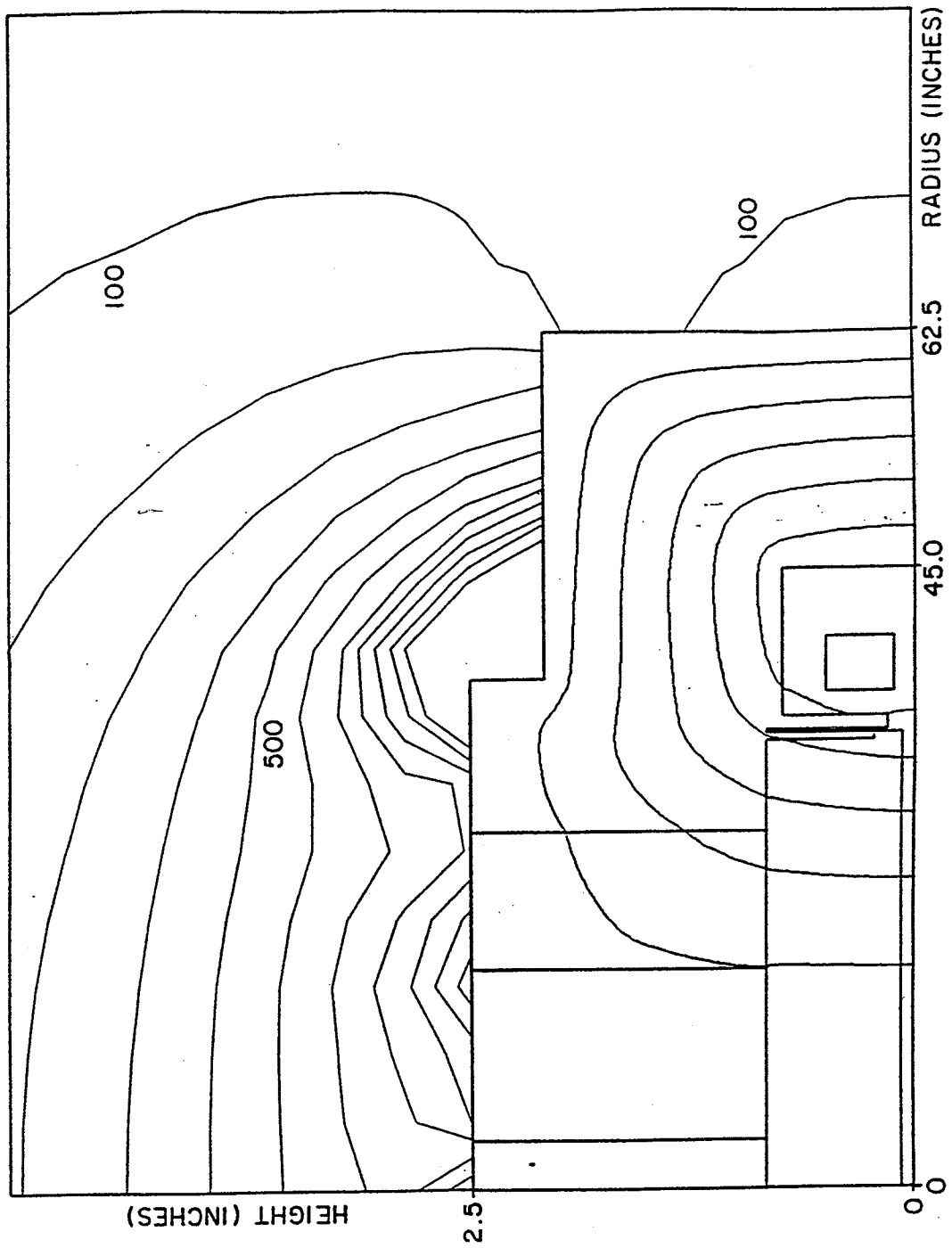

Figure III.3: The arrangement of magnet iron and main coil used for relaxation calculations of the magnet field. Flux lines are shown inside the steel and contours of equal field strength are shown outside. The labels on the outer contours give fringe field strength in gauss.

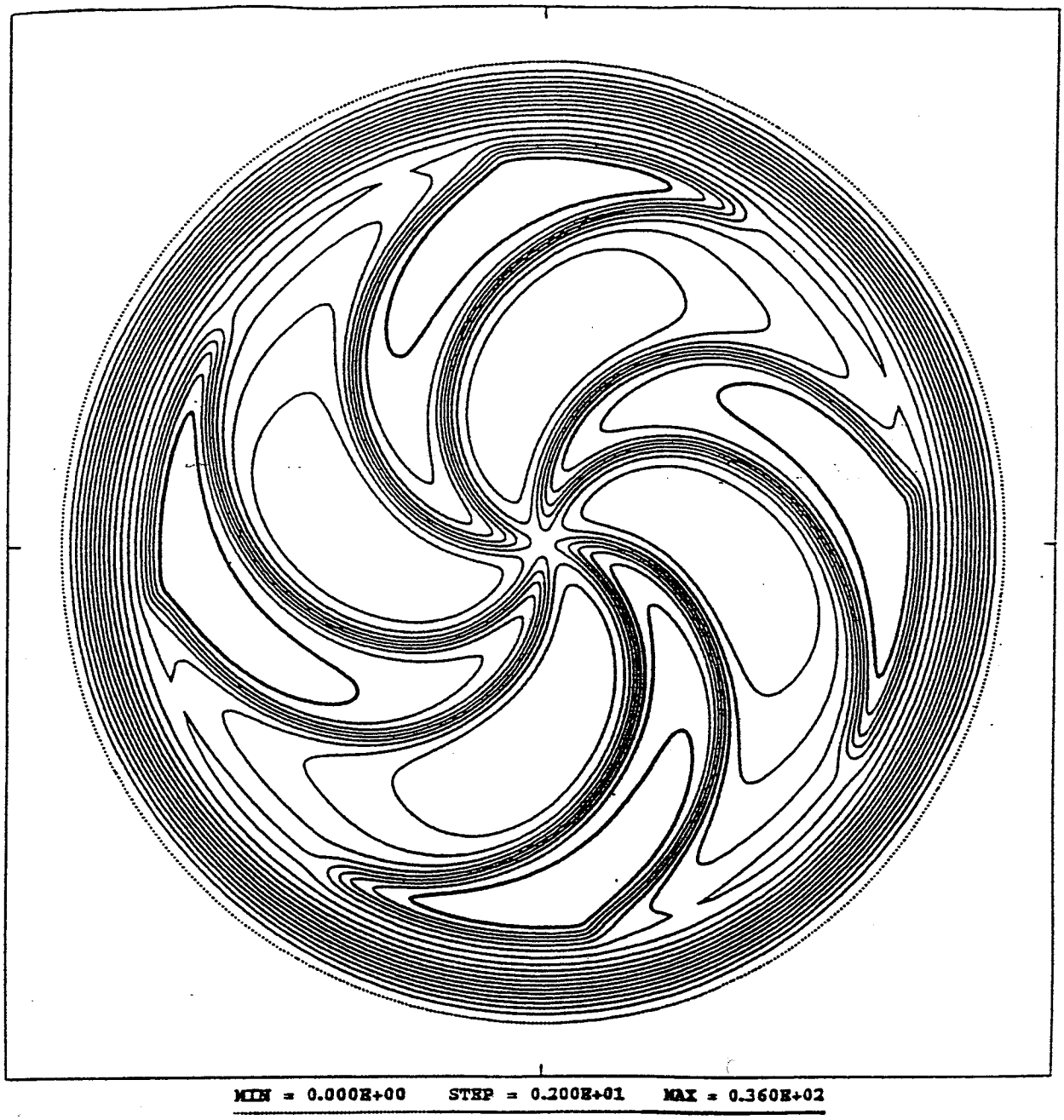

Figure III.4: Contour map of the medium plane field. Contour spacing is two kilogauss with the dotted contour at the outside at zero field strength and the double weight contour in the outer part of each hill at 36 kilogauss.

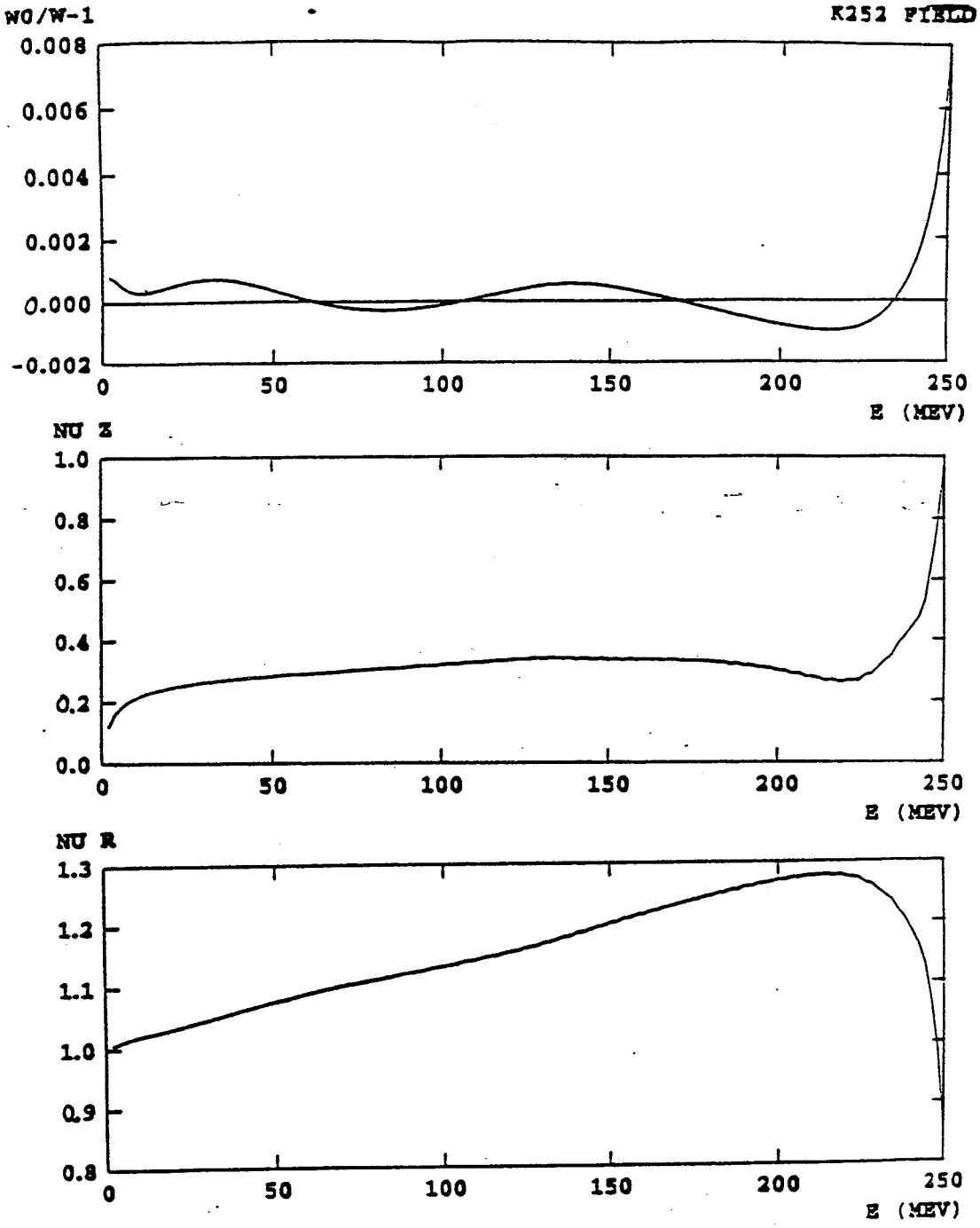

Figure III.5: Computer properties of closed orbits in the magnetic field of Fig. III.4. Upper plot shows the proton orbital frequency relative to a fixed value and the lower traces show the frequency with which linearly displaced orbits oscillate relative to the closed orbit.

not reach, the intrinsic third order resonance at 1.33; the NU Z curve corresponds to excellent axial containment; and the orbital frequency errors give small, readily tolerable, phase excursions relative to the rf accelerating voltage.

The closed orbit characteristics establish that actual accelerated orbits will be well behaved through the middle 95% of the acceleration process. At beginning and end more detailed calculations are needed to insure that orbits are similarly well behaved as the ions exit the ion source in the sensitive central region, and at the final energy, where a first harmonic perturbation is used to expand the turn spacing as the beam enters the extraction system.

Figure III.6 gives a median plane map of the central region with three orbits superimposed on equi-potential contours of a four dee acceleration system. The orbit shown with the solid line leaves the ion source at the design reference time; the orbits shown as dotted and dashed lines leave the source 10 degrees earlier and later respectively. Dees are located at the left, right, top, and bottom of the figure and the left/right pair is phase shifted by 180 rf degrees relative to the up/down pair so that the voltages on the two pairs are always equal and opposite, as can be inferred from the equi- potential contours. The location of the ion source housing produces the wart-like contour loop just below the point where the three orbits begin. The electric equi-potentials are calculated with a three dimensional relaxation code which allows a realistic representation of the actual electrode surfaces. Overall, such calculations give excellent agreement with experimental measurements of central orbits[35].

Figure III.7 shows the behavior of orbits initially displaced in the axial direction relative to the Figure III.6 orbits (the lower traces in the figure) or with an initial axial velocity (the upper traces). The overall behavior is seen to be excellent – the focusing oscillation is well defined and shows a period of about five turns which matches smoothly to the focusing in the main acceleration region.

A vertical section view of mechanical features of the central region electrodes is given in Figure III.8. A partial section view of one of the dees is on the left in the Figure (the coupled right and left dees from Fig. III.6); a magnet hill is on the right with an initial coarse phase selection slit, as in the MSU K50 cyclotron, and with centering coils mounted under the copper rf liner on the upper and lower magnet hills. Cathodes for the ion source show above and below the source chimney (the tube extending thru the median plane). Because of the tight 8 mm clearance between the source chimney and the extraction dee, the cathodes must be inserted separately from the top and bottom as is done in the medical cyclotron in Detroit. Cathodes in that cyclotron have a life-time of approximately six months before they must be replaced due to erosion; in the proton cyclotron, cathodes will probably erode at an even slower rate than that experienced in the Detroit cyclotron which accelerates deuterons rather than protons.

A plan view of mechanical features of the central region is shown in Figure III.9. Section views at AA and BB are also shown to give details of the centering coil arrangement and to show that the apparent conflict between hill structures and accelerating electrodes in the main plan view is due to viewing elements not in the same plane and is not a real

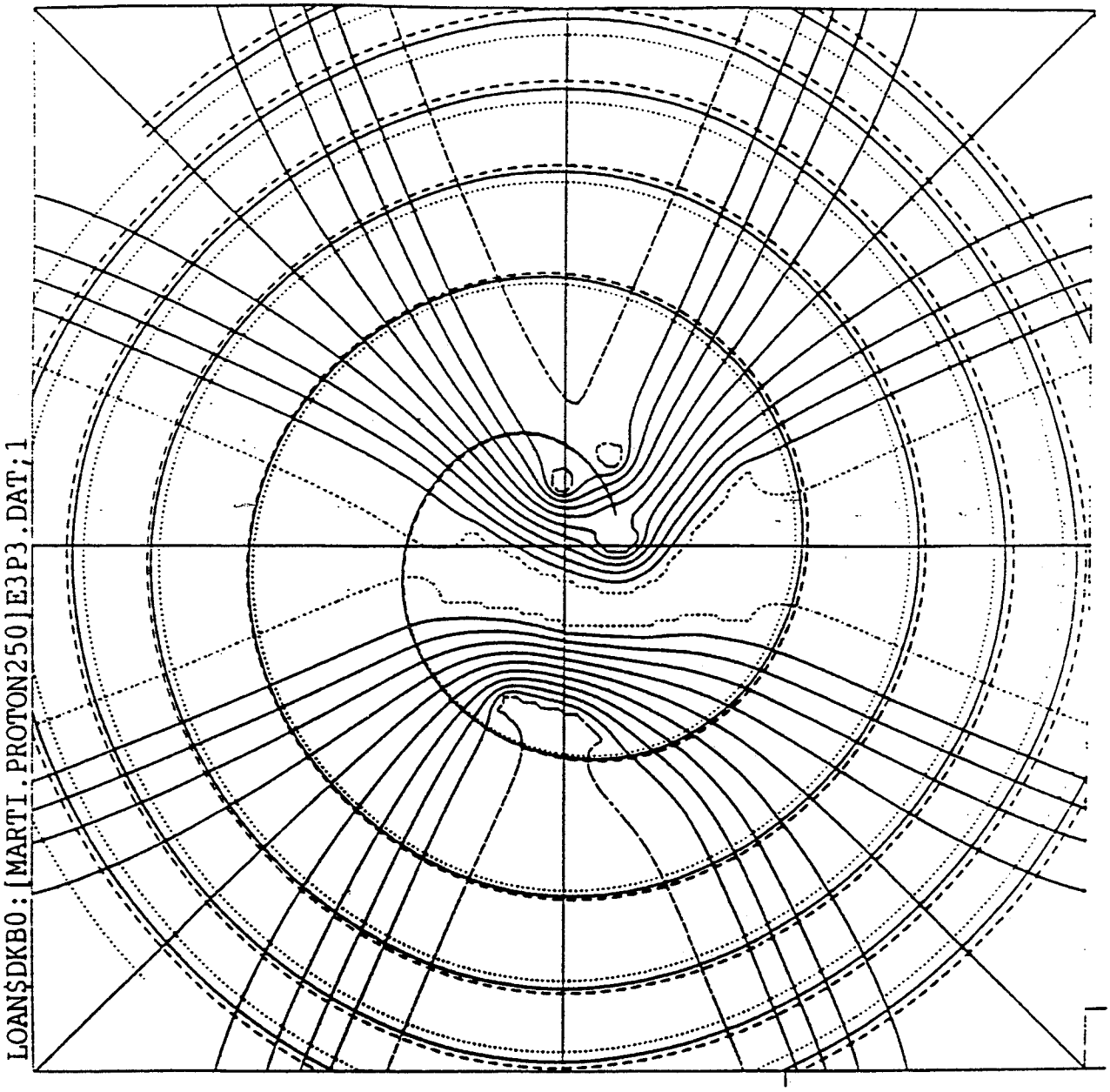

Figure III.6: Orbit behavior in the central region of the proposed medical cyclotron superimposed on voltage equi-potentials calculated with three dimensional relaxation code. Dees are at left, right, top and bottom with left-right dees galvanically coupled across the center and with top and bottom dees phase shifted by a 180 degrees relative to the left/right parent. Coordinate grid is +/-8.6 centimeters in each direction. Solid black ray left the ion source at rf phase of 210 degrees (where 270 corresponds to peak voltage). Dotted ray left source at 220 degrees, dashed ray at 200.

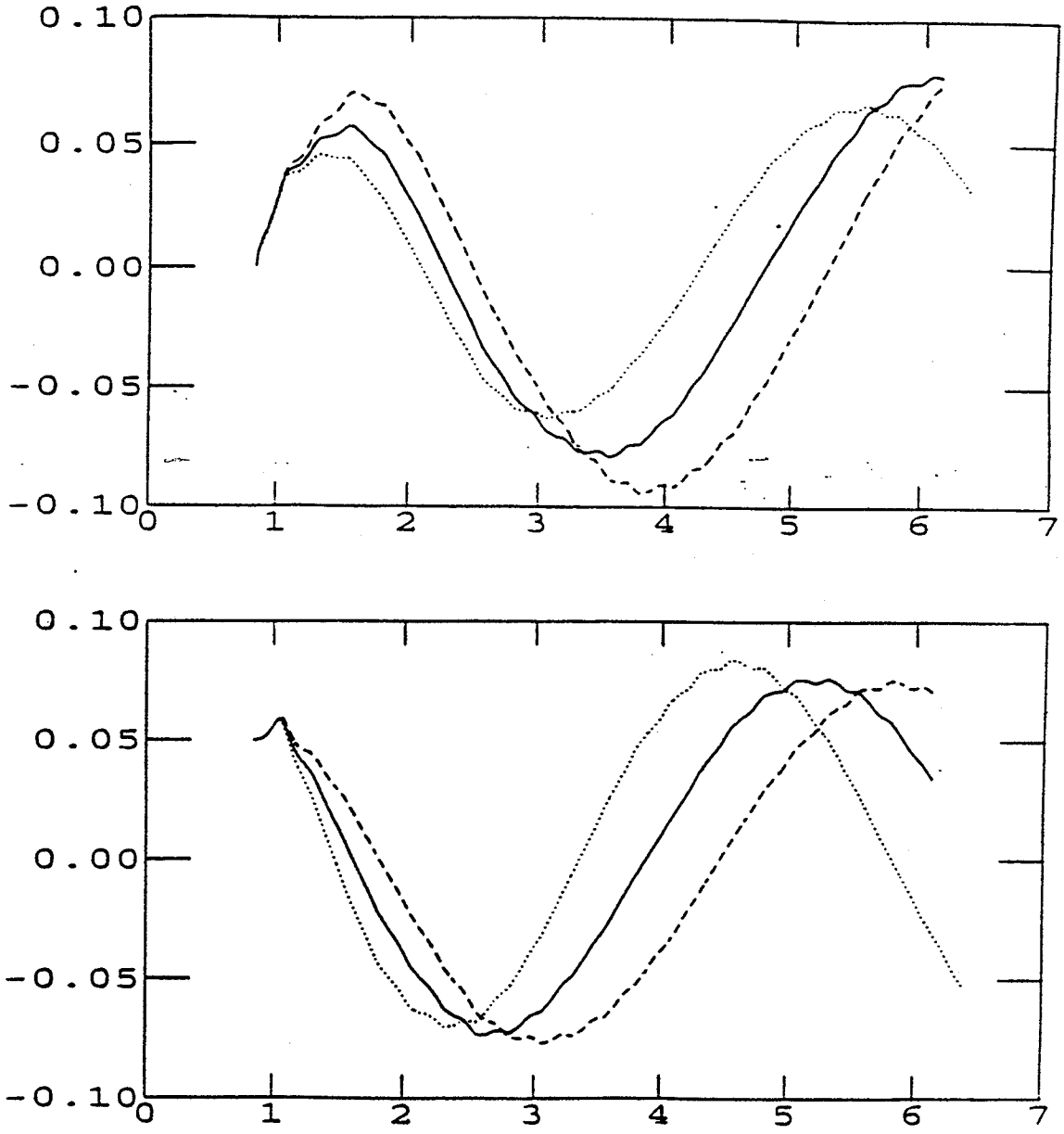

Figure III.7: Calculations of axial motion associated with the three orbits of Fig. III.6. In the upper group the orbits are given an initial axial velocity and in the lower, an initial axial displacement relative to the median plane ray central ray.

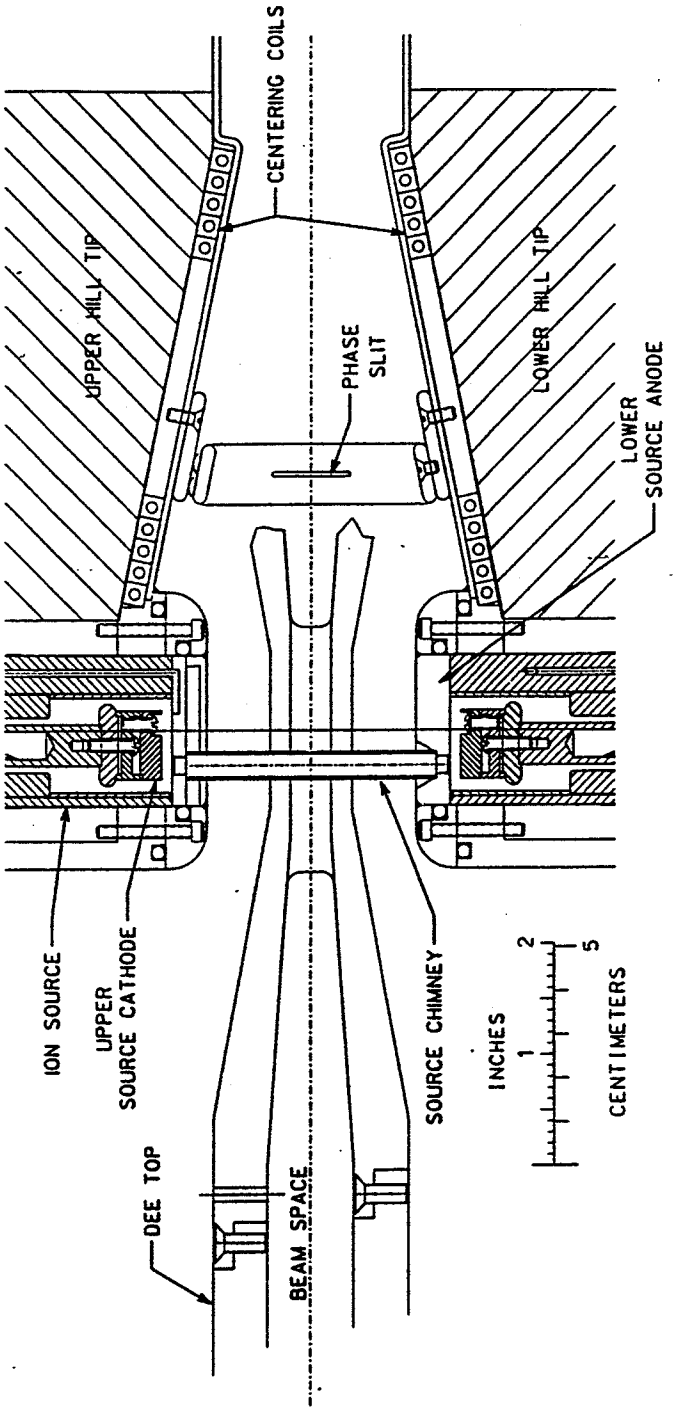

Figure III.8: Expanded vertical section view of the cyclotron central region showing details of ion source cathodes and anodes, the centering coils, and a portion of the east/west dee pair with the galvanic coupling crossing the cyclotron axis.

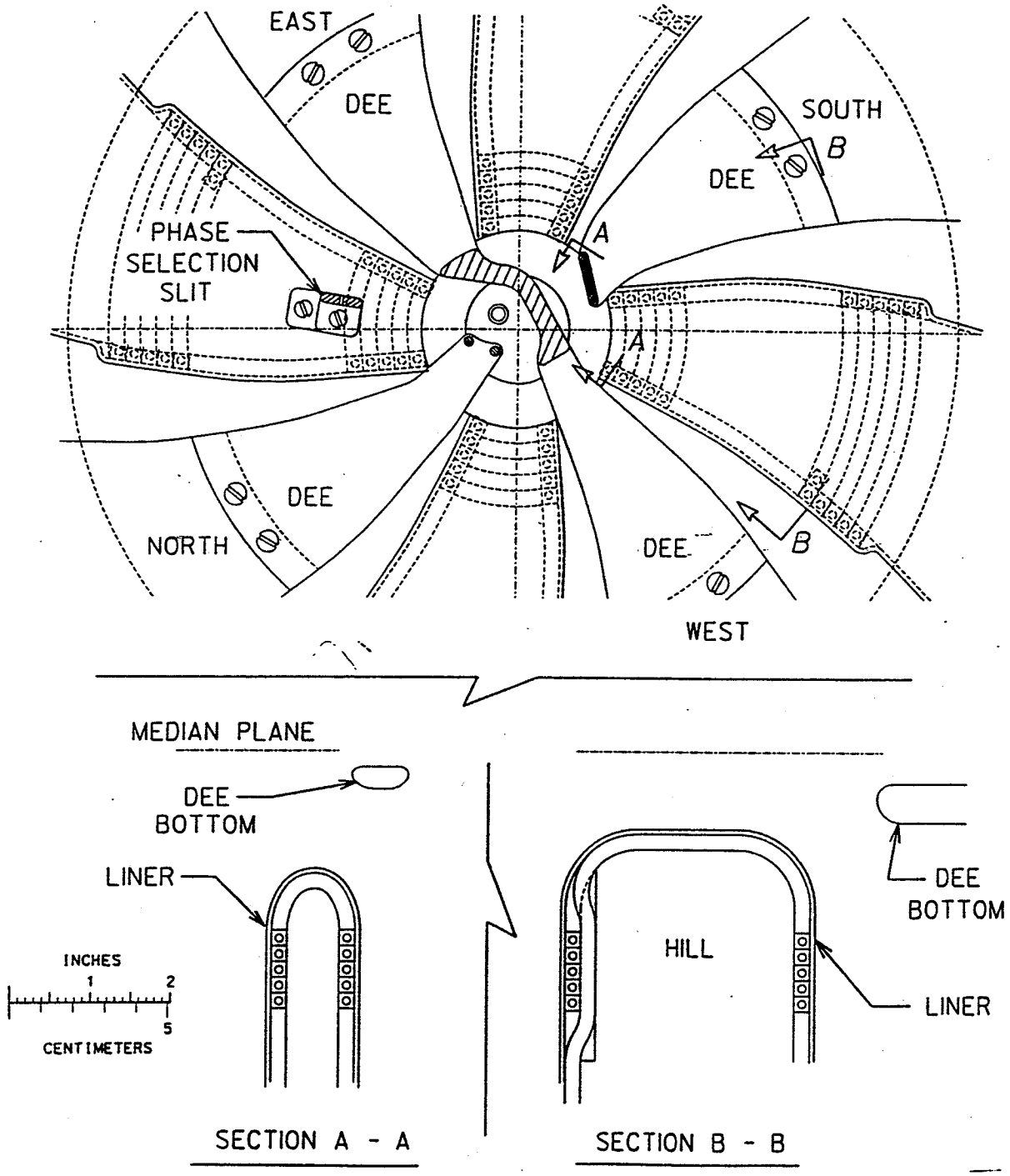

Figure III.9: Plan view showing mechanical details of the central region of the proton therapy cyclotron. The section views in the lower part of the Figure show the real clearance between dees and liner at two typical locations.

conflict.

The proton therapy cyclotron will include a phase selection system based on the design of the system used in the MSU K50 cyclotron[36]. Such systems can be superbly effective because of the extremely high brightness of an optimized proton source. Microamp intensities are transmitted by submillimeter slits, and the resulting, phase selected beam is very sharply bunched in time. Figure III.10 shows a time distribution observed experimentally in the K50 cyclotron, and the orbit calculations establishing the design of the phase selection system. With such a sharply bunched beam, fully separated turns can be easily achieved at the point of extraction as shown for the K50 beam at the lower right of Figure III.10. (The stabilization of magnetic field and of radiofrequency voltage, which are also necessary in order to have cleanly separated turns, are routinely achieved in modern magnet power supplies and rf systems.) With such cleanly separated turns at the entrance of the extraction system, lossless extraction can be effectively achieved and activation of the cyclotron is then largely eliminated.

Mechanical features of one of the selection slit mechanisms are shown in Fig. III.11. The retractable slit is formed by a pair of tungsten rods of 3 millimeter diameter with 0.2 millimeter aperture between the rods. Two such slit assemblies are required to accomplish the desired phase selection.

The proton beam will be extracted from the proton therapy cyclotron using the precessional extraction process pioneered in the MSU K50 cyclotron[30] and now used in nearly every positive ion cyclotron. An orbit 'precession' or off-centeredness is induced at the NU R = 1 resonance which occurs near the edge of an isochronous cyclotron as the isochronous field begins to turn over to join the natural edge field of the magnet. A small field perturbation
having an azimuthal first harmonic component of a few gauss is used to induce a coherent precession of the desired amplitude as the beam accelerates through this resonance. Final turns separate cleanly in radial position as a result of this precession, as seen in the lower right detail of Figure III.10 which is an experimental turn pattern taken in the extraction region of the K50 cyclotron.

Calculated beam behavior in the proton therapy cyclotron is shown in the upper half of Figure III.12. In the Figure III.12 computations, a "beam" is shown in radial phase space with the position coordinate on the horizontal axis and the direction coordinate on the vertical axis. An initial phase space ellipse is started at the left of the Figure and tracked for 50 turns through the later part of the normal acceleration region and into the extraction resonance. For clarity, the full ellipse is plotted only on every tenth turn for the first 40 turns, but with the central ray plotted on every turn – then for the final ten turns the full ellipse is plotted on every turn. The ellipse used in these calculations has approximately three times the amplitude, or ten times the area, of the experimentally observed emittance of the beam from the K50 cyclotron; actual turn separation in the medical cyclotron is therefore likely to be even cleaner than the calculation indicates.

[The aperture of the source slit and of the slits in the phase selection system interact with the duty cycle of the 'pulsed CW' operating mode, and with ion source 'brightness'.

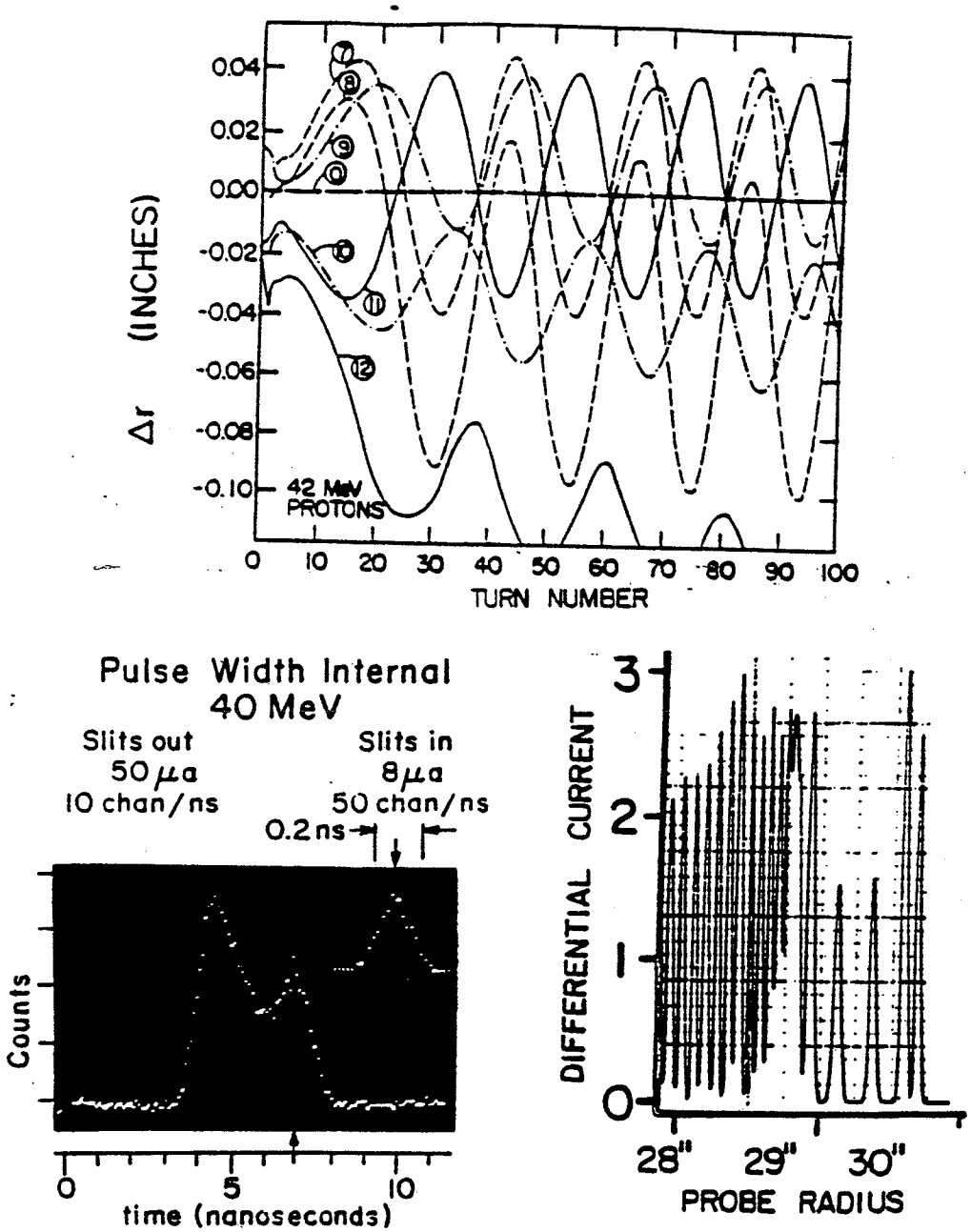

Figure III.10: Top: computer calculation for the K50 cyclotron showing orbit displacement from the central ray caused by different initial rf phase (basis for K50 phase selection system [36]). Lower left: experimental time-of-flight spectrum showing beam pulse structure with slits out and in – 0.2 nanoseconds corresponded in the K50 to a phase width of +/- 3.5 rf degrees. Lower right: final turns in the K50 displayed vs. radius (with phase slits in) showing cleanly separated turns beyond radius of 29".

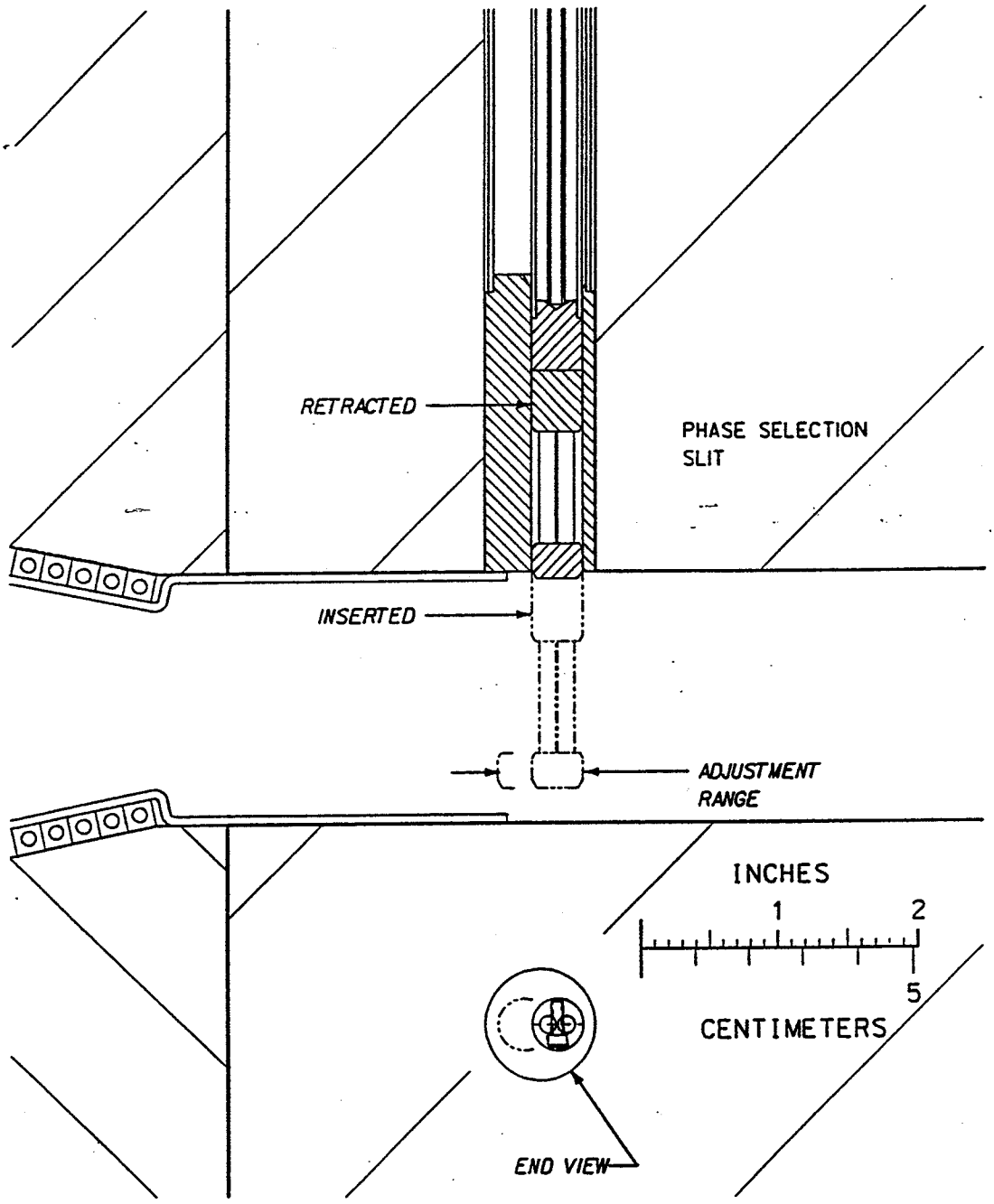

Figure III.11: Mechanical drawing showing details of one of the two phase- slits which will be used in the 250 MeV cyclotron. Each slit can be retracted or inserted remotely and moved in radius by rotating the outer mounting tube while holding the slit proper with no rotation.

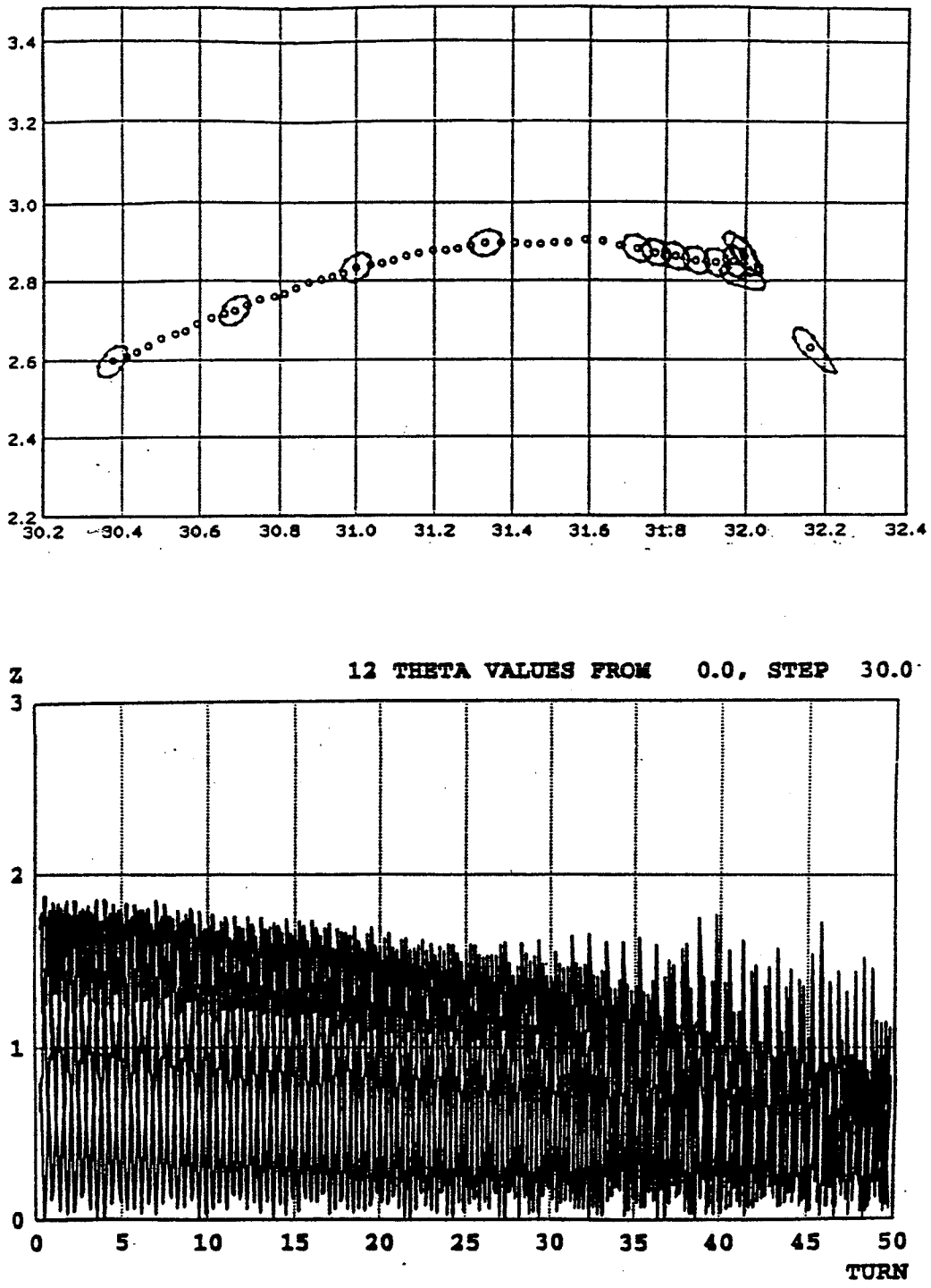

Figure III.12: Top: radial phase space plot of distribution of accelerated rays representing proton beam. Lower: plot of Z vs theta for a ray displaced initially 1.8 millimeters in Z from the central ray of the upper trace.

The results in Figure III.10, for example, are for a beam of 8 microamps, from a hot-filament ion source, accelerated for 212 turns, in the first harmonic mode, with full CW rf. In the medical cyclotron corresponding quantities are 10 nanoamp beam, cold-cathode arc source, 500 turns, second harmonic, and pulsed CW rf. The thousand fold factor in desired beam current will be in part accomplished by reducing the duty cycle and in part by using smaller slits which will increase beam precision. The optimum choice for this tradeoff will be determined as a part of the startup testing of the cyclotron at the NSCL. These studies will also take account of the longitudinal space charge effect[37], which will be larger than in the K50 due to the larger number of turns and the higher acceleration harmonic – lowering the instantaneous beam intensity by using narrower slits and a higher duty factor decrease the space charge force. This effect will also be included in the final overall tuning optimization.]

The $\nu_r = 2\nu_z$ coupling resonance (the "Walkinshaw resonance") occurs in the proposed medical cyclotron before the $\nu_r = 1$ radial imperfection resonance. This is advantageous relative to the reverse order in which these resonances occurred in the K50 cyclotron, because the effect of the resonance is to convert radial amplitude into axial amplitude, and, if the radial amplitude is nulled by carefully centering the beam in the normal acceleration region, the effect of the resonance is negligible. This is shown quantitatively in the lower graph of Figure III.12 which shows axial amplitude 'Z' vs. turn number for an orbit initially displaced axially from the central ray of the upper plot of Figure III.12 and then tracked through the same fifty turns as in the upper graph. The slight coherence which develops in the axial focusing oscillation in the last fifteen turns is the only indication of the presence of the coupling resonance, and this is insignificant in terms of its effect on external beam properties. These calculations then establish that a cleanly separated, tightly focused beam will enter the extraction system.

Continuing along the beam path, Figure III.13 shows the behavior of sets of radially and axially displaced rays as they pass through the set of extraction elements, the azimuthal location of the several elements being indicated by the rectangular labeled boxes between the two scales in the Figure. The axially displaced rays are plotted on the upper scale in the Figure and radially displaced rays on the lower scale. The arrangement of focusing elements has been optimized to give a very smooth distribution of the beam envelope with no large excursions; the beam therefore feels only the linear component of the focusing bar fields so that the precise optical properties of the beam as it enters the extraction system are preserved in the beam which exits.

The two longer boxes in Figure III.13 (labeled 'E') are electrostatic deflectors. A top view of the first deflector is shown in Figure III.14 and a cross section through one of the support insulators is shown in the upper part of Figure III.15. Since the medical cyclotron is a fixed energy, single-ion cyclotron, there is no need for the aperture to be as large as in K500 and K1200 cyclotrons (where the aperture must provide for the change in the orbit shape as energy or ion are changed). We therefore provide a 5 mm aperture in the medical cyclotron deflector vs the 7mm provided in the design of the K500 and K1200 cyclotrons. The smaller aperture lets the power supply and feed- through insulator

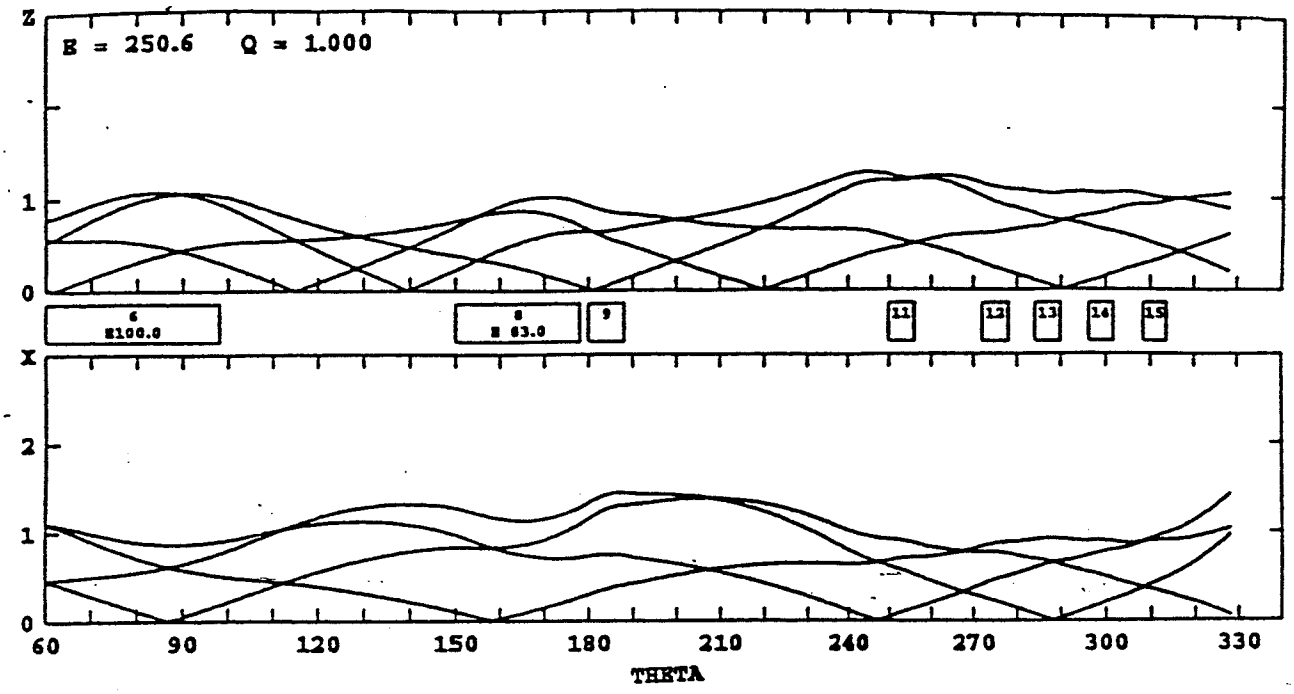

R = 32.1600 PR = 2.6300 E = 250.60

DEF	TH1	TH2	TYP	E,B,R	DER,AL	DE1	DE2
6	60.00	98.00	1	100.000	0.000	0.000	0.000
7	102.00	148.00	5	999.000	0.000	32.000	32.000
8	150.00	178.00	1	83.000	0.000	0.000	0.000
9	180.01	188.00	3	32.953	-1.000	0.000	0.000
10	192.00	238.00	5	1.180	180.000	32.404	32.358
11	249.93	256.05	3	33.947	3.400	0.000	0.000
12	272.01	277.96	3	34.890	5.100	0.000	0.000
13	284.09	289.88	3	35.694	7.200	0.000	0.000
14	296.20	301.75	3	36.878	10.600	0.000	0.000
15	308.40	313.53	3	38.782	17.100	0.000	0.000
16	0.01	8.00	4	32.953	-1.000	0.000	0.000
17	84.02	89.98	4	34.600	0.000	0.000	0.000

Figure III.13: Extraction channel behavior of phase space distribution of rays plotted as Z and R displacement from central ray vs azimuthal location. Parameters of extraction elements are shown in the table. Type code 1 indicates electrostatic deflectors, type code 3 indicates magnetic focussing bars, type code 4 indicates magnetic compensating bars, and type code 5 indicates a radial electric field varying like rf phase (corresponding to the E field at the outer edge of the dee).

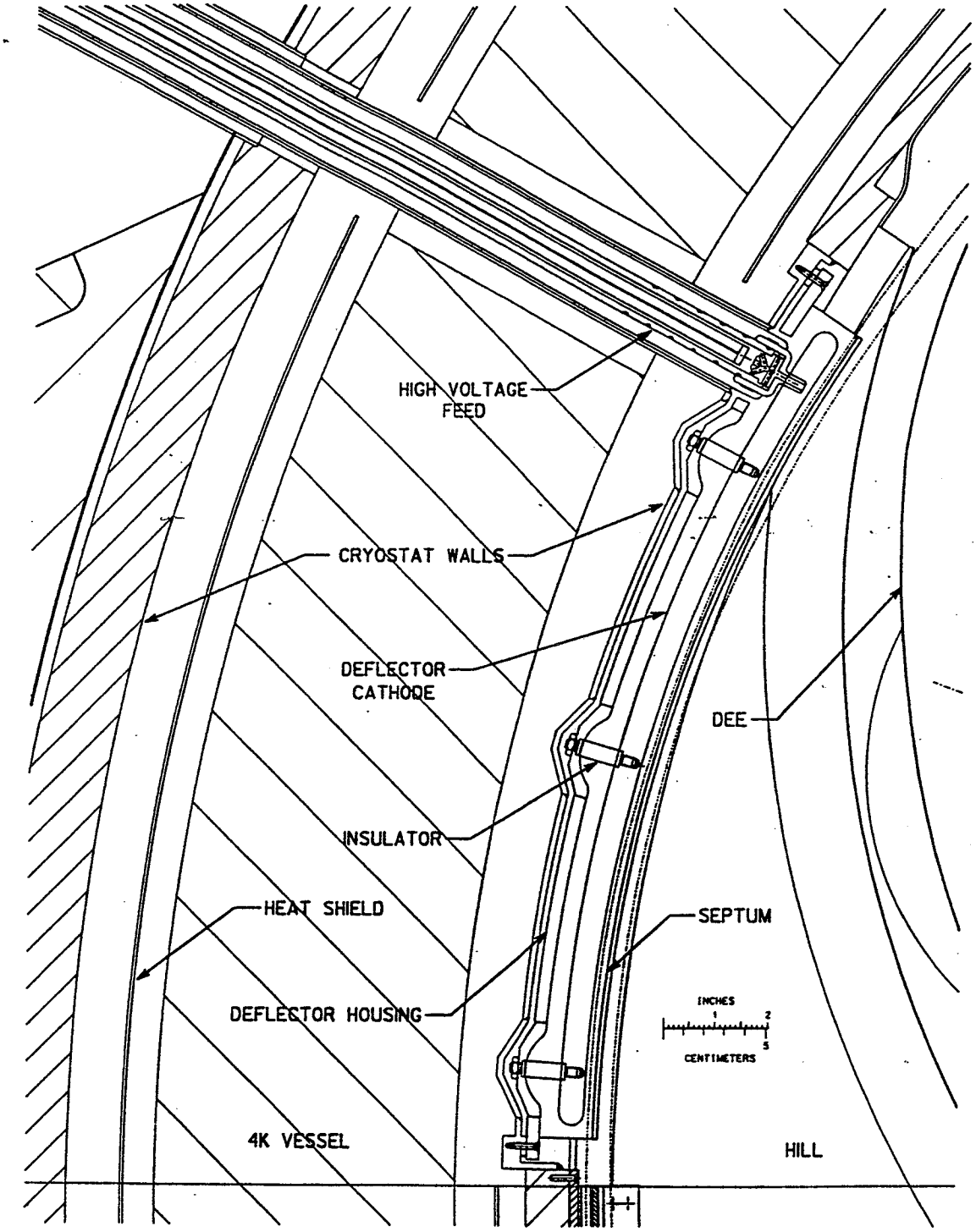

Figure III.14: Plan view of one of the electrostatic deflectors. Fine dotted lines show outer most internal beam ray and the extracted beam central ray.

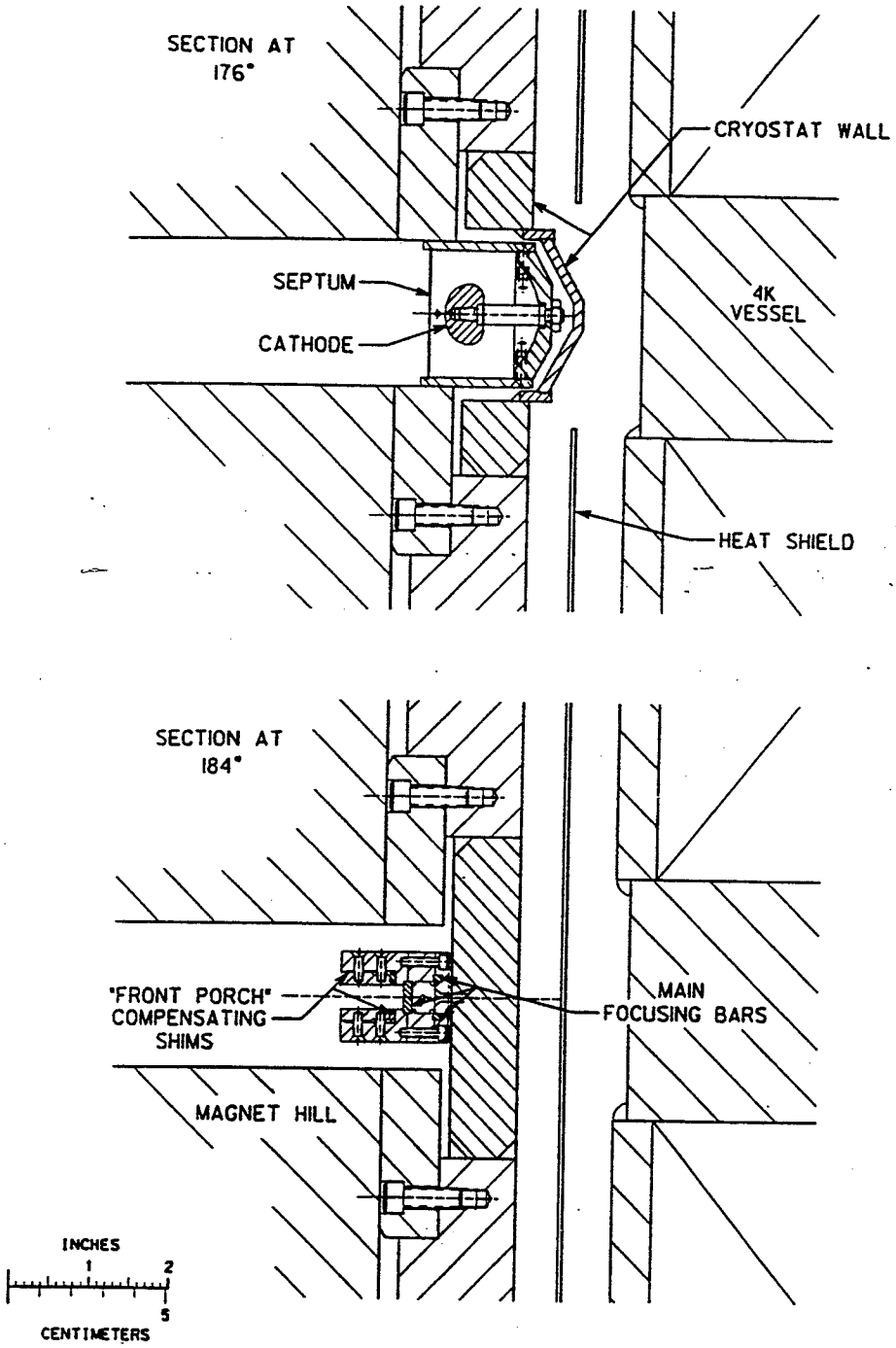

Figure III.15: Section views at 176 degrees and 184 degrees (angular coordinate system is defined in Figure III.2). The 176 degree section is at the location of a mounting insulator for the deflector cathode and the 184 degree section is at the location of the inner most focussing bar assembly.

operate at a lower voltage for a given electric field which decreases the installation sensitivity of these components.

The deflector operating conditions assumed in the calculations have been checked experimentally in the K500 cyclotron by resetting the deflectors in that cyclotron to 5mm aperture, and operating these deflectors at a magnetic field equivalent to that of the proposed K250 cyclotron. In this test the deflectors quickly baked in to the design K250 electric field and operated smoothly at electric fields which were 20% higher than those assumed in the K250 calculations. A recent newsletter from Chalk River[38] also reports deflector operation at fields which are 60% higher than the value used in the K250 calculations, thus further indicating the very conservative margin of safety in the K250 design.

The boxes labeled 9, 11, 12, 13, 14 and 15 in Figure III.13 are so called focussing bars, i.e. small iron elements arranged so that their net magnetic field provides a strong focussing gradient in the radial plane to offset the defocusing gradient from the edge magnetic field of the main magnet. A section view of the innermost of these focussing bars, M1, is shown in the lower part of Fig. III.15. Because of its close proximity to the internal beam, this bar set includes a 'front porch', i.e. a set of small iron sheets of increasing thickness mounted between aluminum blocks held in place by small vertical screws. These iron elements, and a mirror image bar on the opposite side of the cyclotron, offset the effect of the focussing bar fringe field on the internal beam to an adequate degree. Final design calculations for such a system involve a successive approximation loop in the fashion required for the design of the extraction system of the K1200 cyclotron. Computers are fortunately now available which make it possible to track this loop to convergence in a fraction of the time that was required for the K1200 design. The rays shown in Fig III.13 are then the results of a fully self consistent calculation in which the behavior of the beam prior to entering the extraction system is calculated in a field which includes the fringing effects from all of the following magnetic elements of the extraction system.

Figure III.16 is a plan view of the final segment of the extraction path and shows location and mounting details for the five final focussing bar clusters. A section view of one of the bar clusters is shown in the top part of Fig. III.17; the outer bars are simple relative to the inner bars, since no front porch correction is needed. Because the cyclotron will operate at only one magnetic field setting, all of the focusing bar clusters are fixed in position. In the unlikely event that adjustments are necessary, they will be accomplished by removing the bars and remachining the mounting blocks.

The three outer bars are an assembly which slides into the beam tube from the outside, whereas earlier bars attach to the cyclotron wall from inside the cyclotron. Finally, the lower section view in Figure III.16 shows a horizontal and vertical 3 degree steering magnet which will mount in the outer section of the magnet yoke. (This steering magnet is probably not necessary, but is included in the design as a possibly useful contingency feature.) For the prototype cyclotron project proposed here, the final element of the extraction path in Figure III.16 is an instrumentation pot where beam properties can be measured and verified.

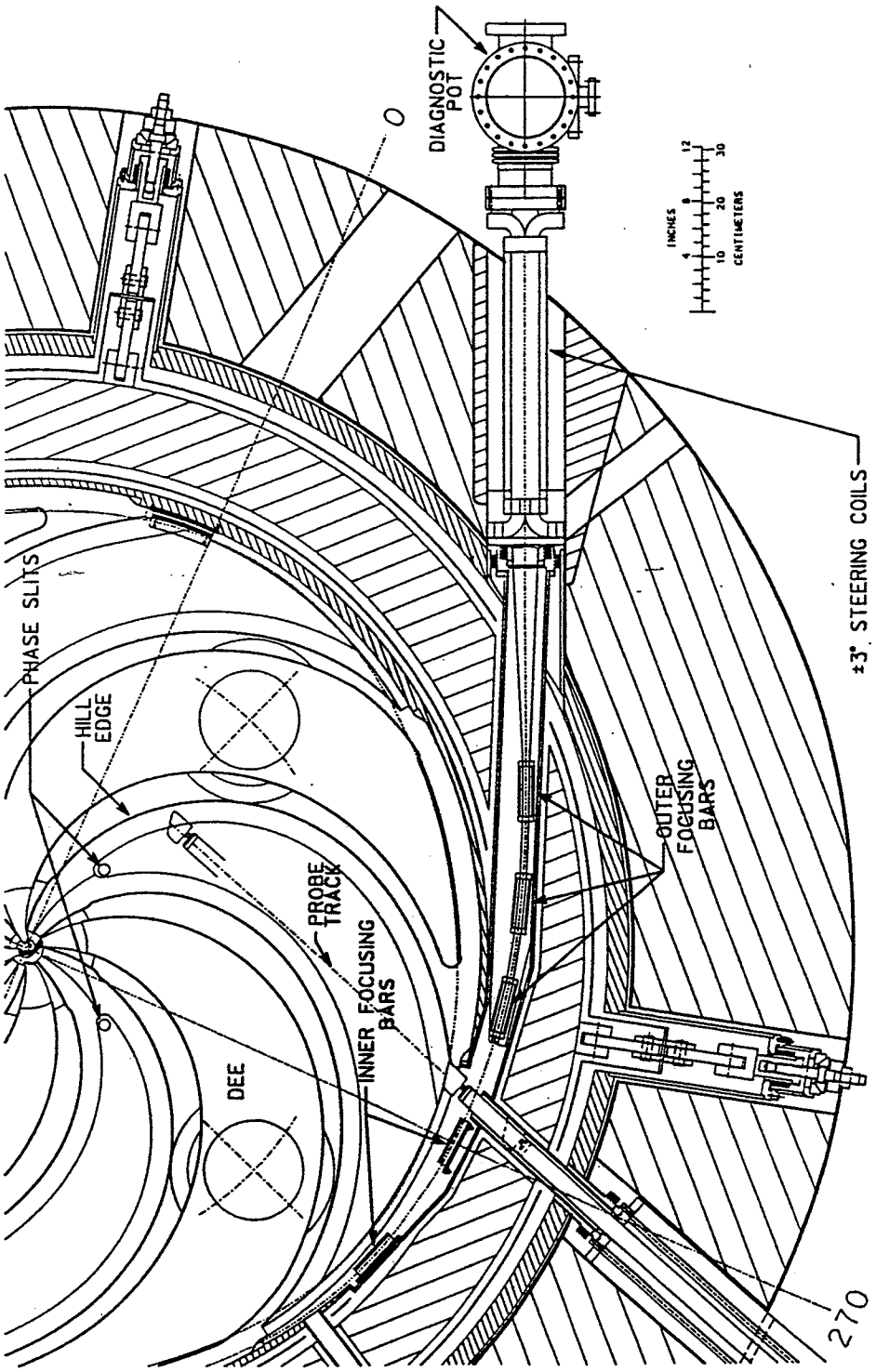

Figure III.16: Expanded plan view of the cyclotron in the vicinity of the extraction orbit showing mounting details for the outer most focussing bars, the +/- 3 degree steering coils and the final beam diagnostic pot.

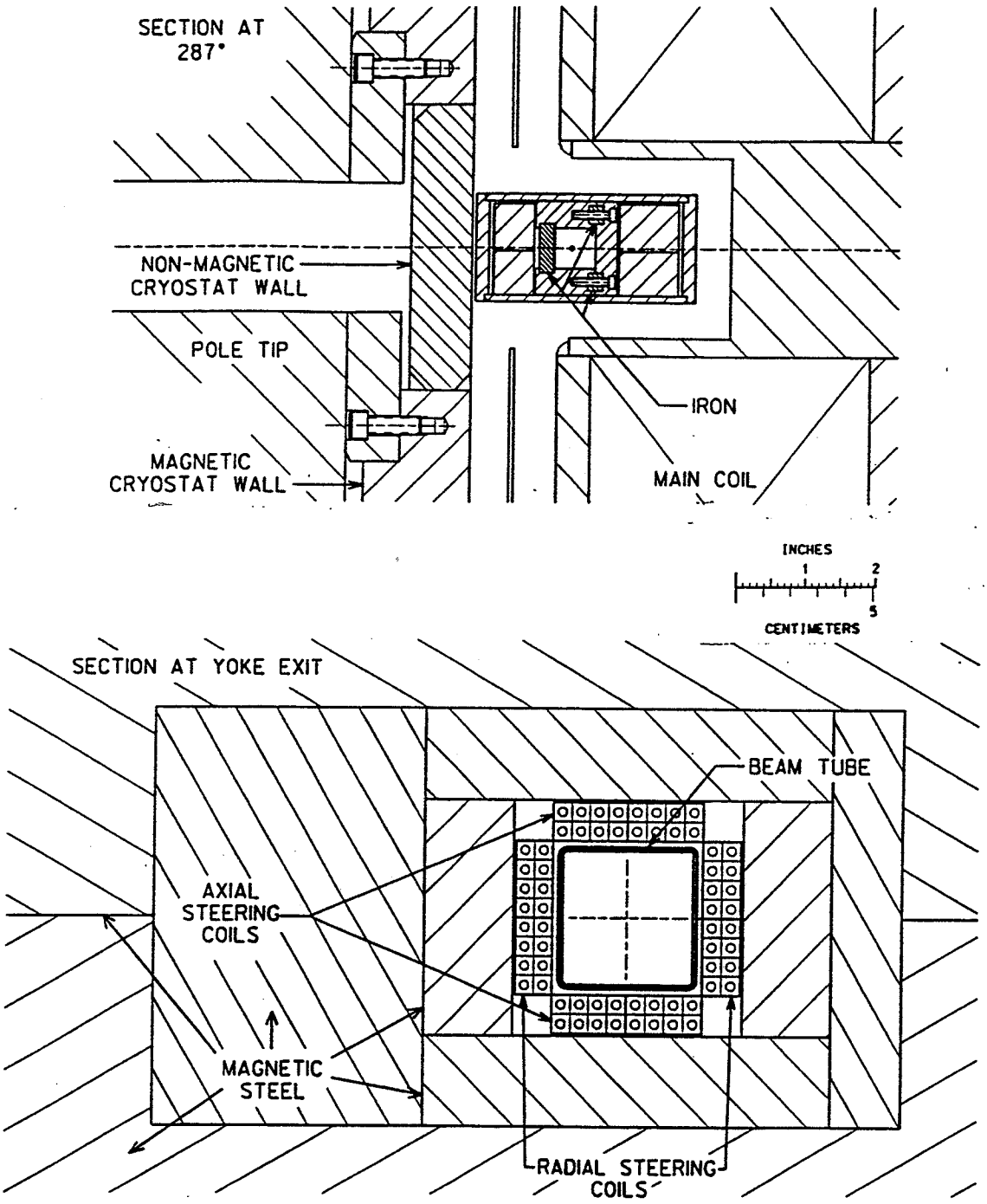

Figure III.17: Section views at azimuth 287 degrees and at yoke exit showing details of the focussing bar mounting system inside the cryostat and the +/- 3 degree steering magnet.

III.2 Yoke, Main Coil, Cryostat and Helium Supply System

The main steel components of the magnet are usually the most expensive single component of a superconducting cyclotron. The steel cost relative to room temperature cyclotrons is never-the-less low, due to the smaller size of the cyclotron and to the fact that the importance of permeability is reduced in high field magnets relative to normal magnets. The magnet can then be constructed from a basic low carbon steel - 1020 steel - which is an inexpensive, broadly available steel grade. Forging to reduce the cross section of the steel will be specified for the main top and bottom disks of the magnet, since voids near the median plane would give unwanted error components in the magnetic field. Also cracks sometimes occur in large castings but not in forgings; significant cracks would give difficulty in the aspect of using the upper and lower caps as part of the vacuum system as is planned in the K250 design.

Since the magnet is a major element of the cyclotron cost, we have contacted several manufactures in the process of preparing the cost estimate. One regrettable factor which has come to light in these discussions is that facilities to forge parts of the size required by our initial design no longer exist in the United States even though excellent facilities continue to be available in Europe and Japan. Before proceeding with procurement of the upper and lower caps we will then invite American manufactures to participate in a design discussion to explore the feasibility of modifying the design to fit the capabilities of American facilities. In any case the outer yoke sections can be castings, and manufacturing facilities for these are available in the US.

The steel for the cyclotron magnet involves a large amount of precision machining as shown in detail in Figs. III.18 and III.19. The cost of these machining operations will match or moderately exceed the cost of the raw steel; we will explore the possibility of buying forgings from Europe or Japan and having these forgings machined in the United States, including by the NSCL shop which has equipment with the necessary capabilities. (The cost estimate in chapter V is based on this later option.)

Figure III.20 shows a cross section of the main superconducting coil and details of its helium vessel, nitrogen shield, and outer vacuum vessel (or 'cryostat'). Major design parameters for the main coil are given in Table III.1.

The coil will be of the 'intrinsically stable' type as used in the Detroit medical cyclotron[39] and also in the Agor cyclotron in France[40]. (The later is still under construction at present but the magnet is complete and has operated properly at full design field.) The intrinsically stable, or potted, coil design reduces fabrication costs and speeds construction and is the standard style of fabrication for small magnets. Very large magnets, including both the K500 and the K1200, have, on the other hand, traditionally adopted a 'cryogenically stable' coil design in which liquid helium passages penetrate the coil so that every turn is in contact with liquid. The helium passages in the cryogenically stable coil open the possibility of short circuits caused by small metal chips, a difficulty which was experienced in the MSU K500 coil. The chief concern with a large, intrinsically stable coil structure is the 'hot spot' temperature in the event of a quench. This temperature depends on the rate of heat transfer from one part of the coil to another, on

Coil	
Type:	Wet wound, epoxy potted
Stored energy:	3.6MJ
Inductance:	169H
Operating current:	206A
Central field:	4T
Peak field coil	2.7T
Coil size(each):	5" axial by 4" radial
Banding:	304SS, 1/2" thick
Overall current density:	3.87 kA/cm
Number of turns per layer:	43
Number of layers:	55
Hot spot temperature in a quench:	140K
Peak internal volts in a single coil:	400

Conductor	
Type:	NbTi with copper stabilizer
Copper-to-superconductor ratio:	20:1
Bare wire size:	0.106" x 0.054"
Insulation:	Dacron, 0.005" on each side
Short sample limit:	550A at 4T (660A at 2.7T)

Table III.1: Major parameters of the main superconducting coil for the K250 medical cyclotron

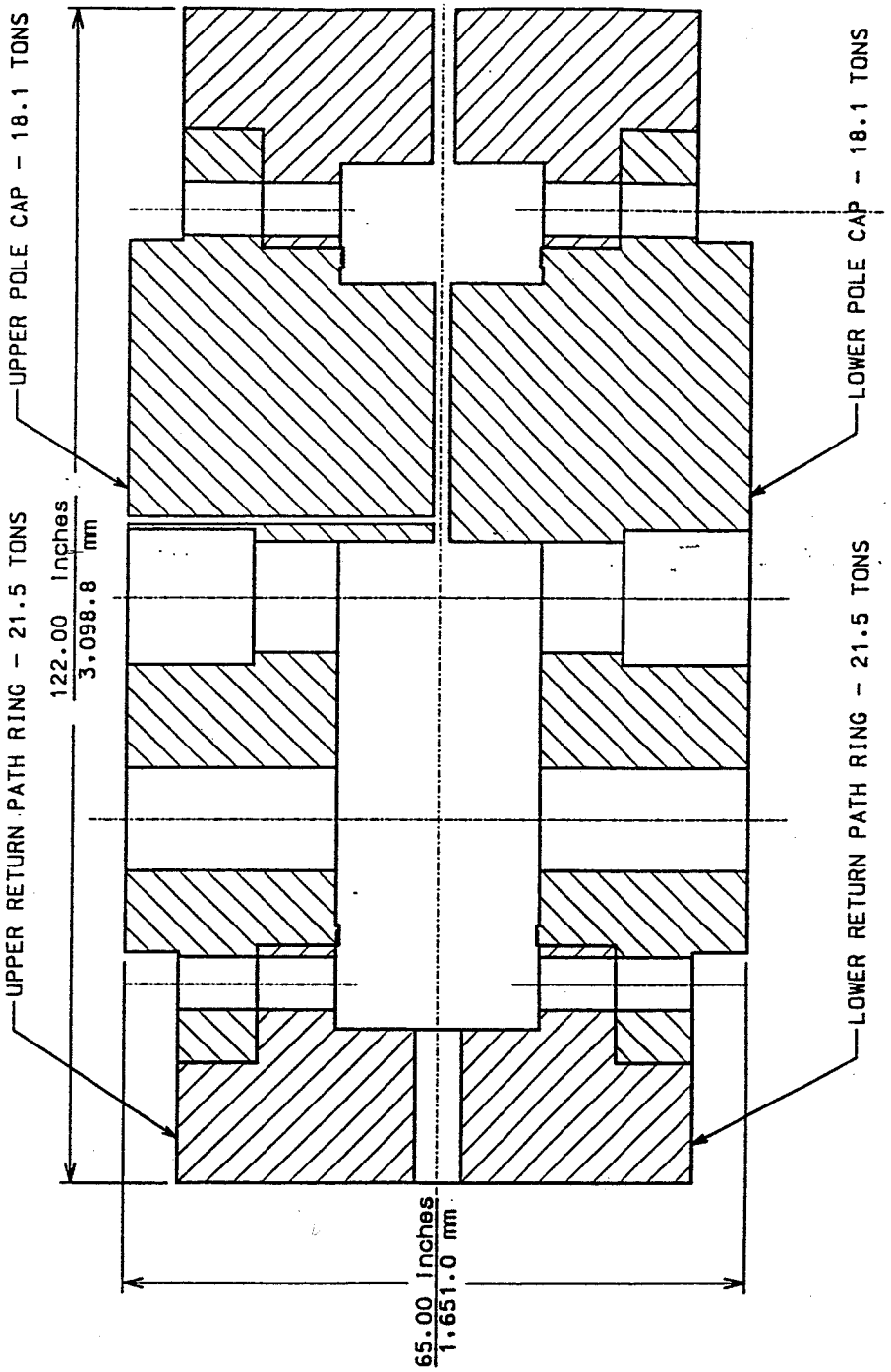

Figure III.18: Section view through the main magnet yoke showing the four primary steel elements which make up the magnet yoke.

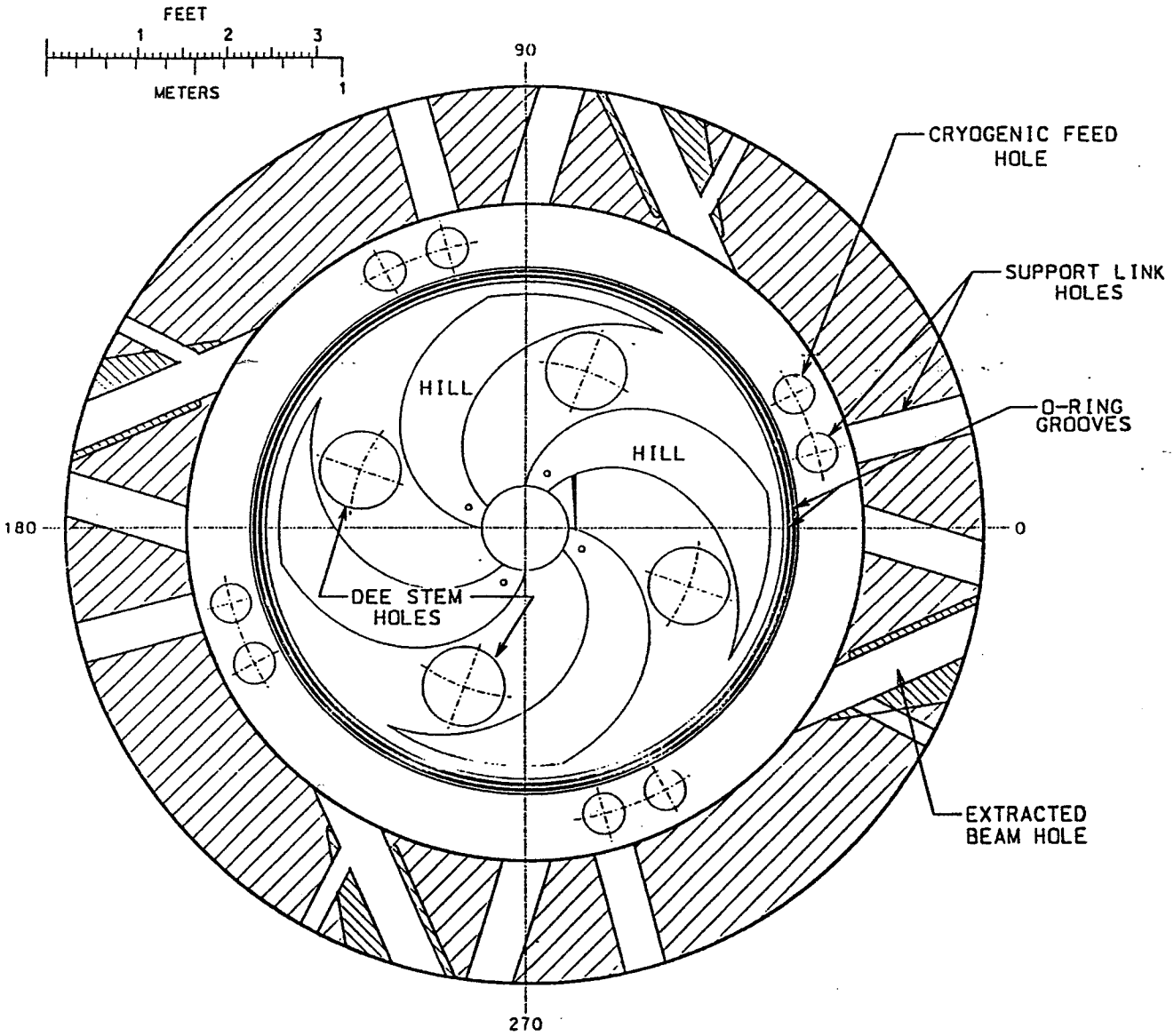

Figure III.19: Plan view showing the many median plane penetrations through the outer yoke rings, the large holes penetrating the cap, and the basic hill layout.

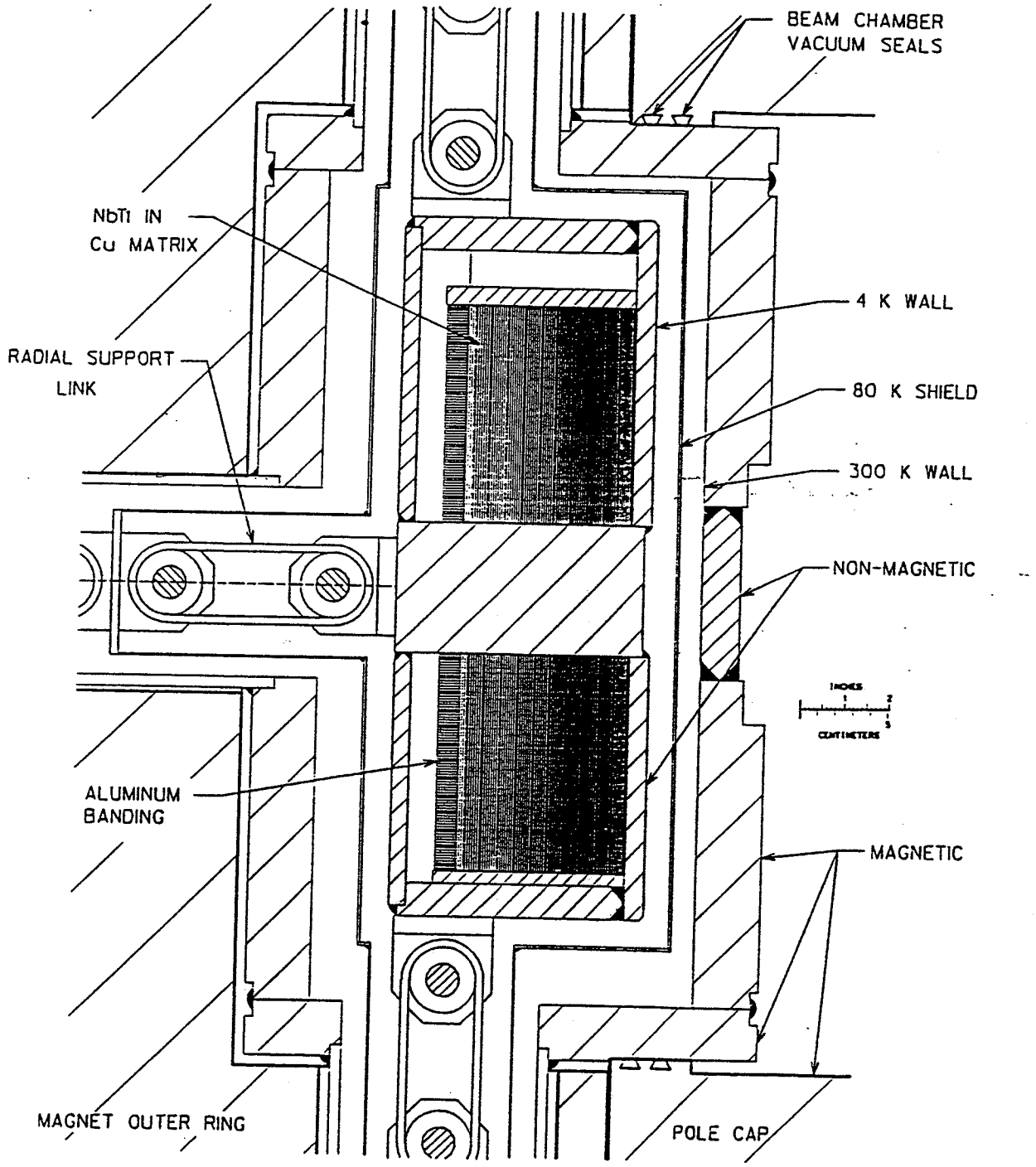

Figure III.20: Expanded vertical section through the main coil in the the vicinity of a radial support link.

the energy stored in the magnetic field, and on the inductance of the magnet (the later determines the time constant with which magnetic energy is dumped into a developing resistive region).

Figure III.21 shows the results of calculations of these phenomena using the code Quench[41]. The calculations are a worst case scenario in which no effort is made to remove magnetic energy by switching an external 'dump' resistor into the circuit. The non-superconducting, or 'normal', volume is seen to spread through the coil before an appreciable fraction of the magnetic energy begins to dump into the coil. This is the desirable condition leading to harmless dissipation throughout the whole coil volume rather than a concentration in a small volume near the original quench. If only one half of the coil quenches (a situation which is not unlikely due to the median plane barrier between the two coil halves), a voltage to ground will appear at the median plane connection between the two coil halves, equal to one half the product of current and resistance in the half coil which has quenched. Calculations indicate a peak IR drop of 400 volts, a moderate level compared to the 4000 Volt IR drop for the medical cyclotron in Detroit. This voltage is nevertheless at a level such that insulation on the coil-to-coil connecting lead will need to be carefully arranged in order to prevent an arc from the connection lead to ground in the event of a quench.

The potted coil halves will be enclosed in a stainless steel helium vessel as shown in Fig. III.20. This vessel is welded shut and suspended on a network of twelve fiberglass links (4 up, 4 down, 4 horizontal) as can been seen from various prospectives in Figs. III.1, III.2 and III.20. Construction details of one link assembly are shown in Figure III.22. Composite high- strength, S-glass links will be used since these provide a much higher ratio of strength to heat leak than can be obtained with pure metallic supports. Such links are a standard component of many large superconducting magnets.) Each of the links will include a strain bolt at the room temperature end to allow balancing of the load in the over-constrained twelve link system; these strain bolts also allow tracking of magnetic forces on the coil as the magnet is first energized to correct for alignment errors in assembly. The use of two links in series, with a metallic coupling between, provides a solid temperature intercept on the link system which greatly reduces the total heat leak to the 4 K vessel. The links shown in the drawings are a copy of links recently fabricated at NSCL for a large superconducting spectrograph and have a breaking strength of 20,000 pounds at room temperature; this is more than is needed in the proton therapy cyclotron application, and has the advantage of using existing tooling.

Fig. III.23 shows the liquid helium supply system for the medical cyclotron facility and Figure III.24 the warm helium gas handling system. Liquid helium storage dewars are provided at the refrigerator and on the top of the cyclotron. (This design feature assumes that a relatively long transfer line would be needed at most actual medical sites to carry liquid helium from the refrigerator production dewar to the cyclotron storage volume – the average total heat load on the system would then be greatly reduced by using the long line in a batch fill mode.) The auxiliary vessel, labeled '80 to 300K', is provided to allow an easy piping change from a boil-off gas cooled intermediate temperature shield

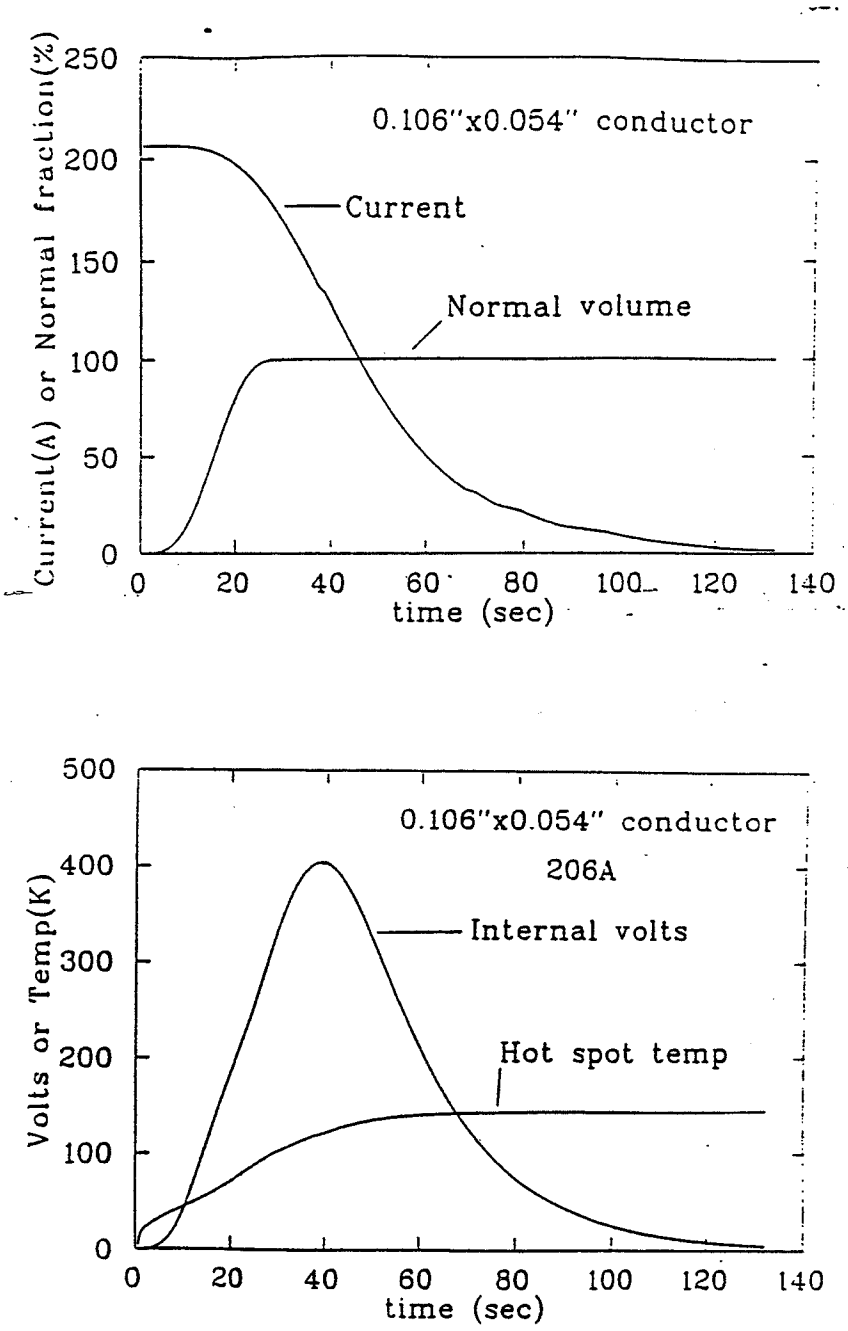

Figure III.21: Calculations of the behavior of the main coil in the event of a quench. The normal volume first spreads through the coil with a relatively low build up of coil resistance (due to the large mass of copper). At about 40 seconds the product of current and resistance reaches a peak and by approximately 60 seconds the hot spot temperature has reached its steady state value.

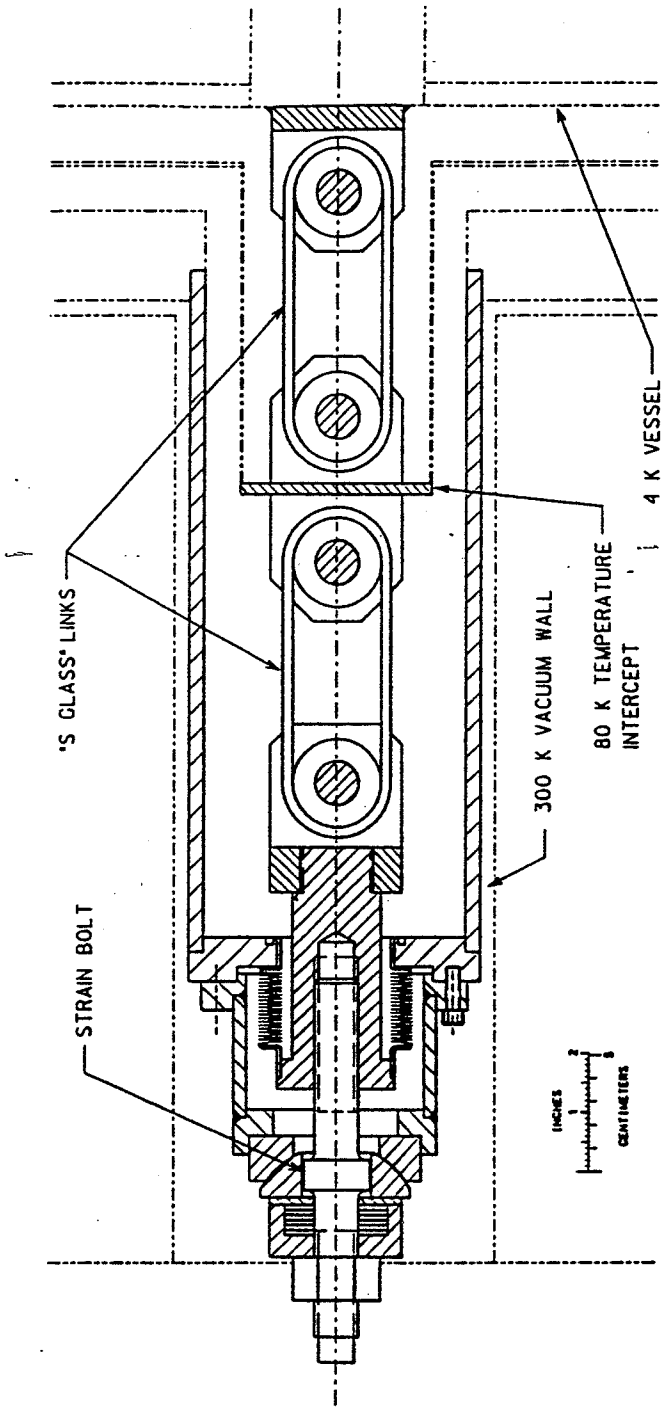

Figure III.22: Expanded vertical section view showing the elements which make up a radial main coil support.

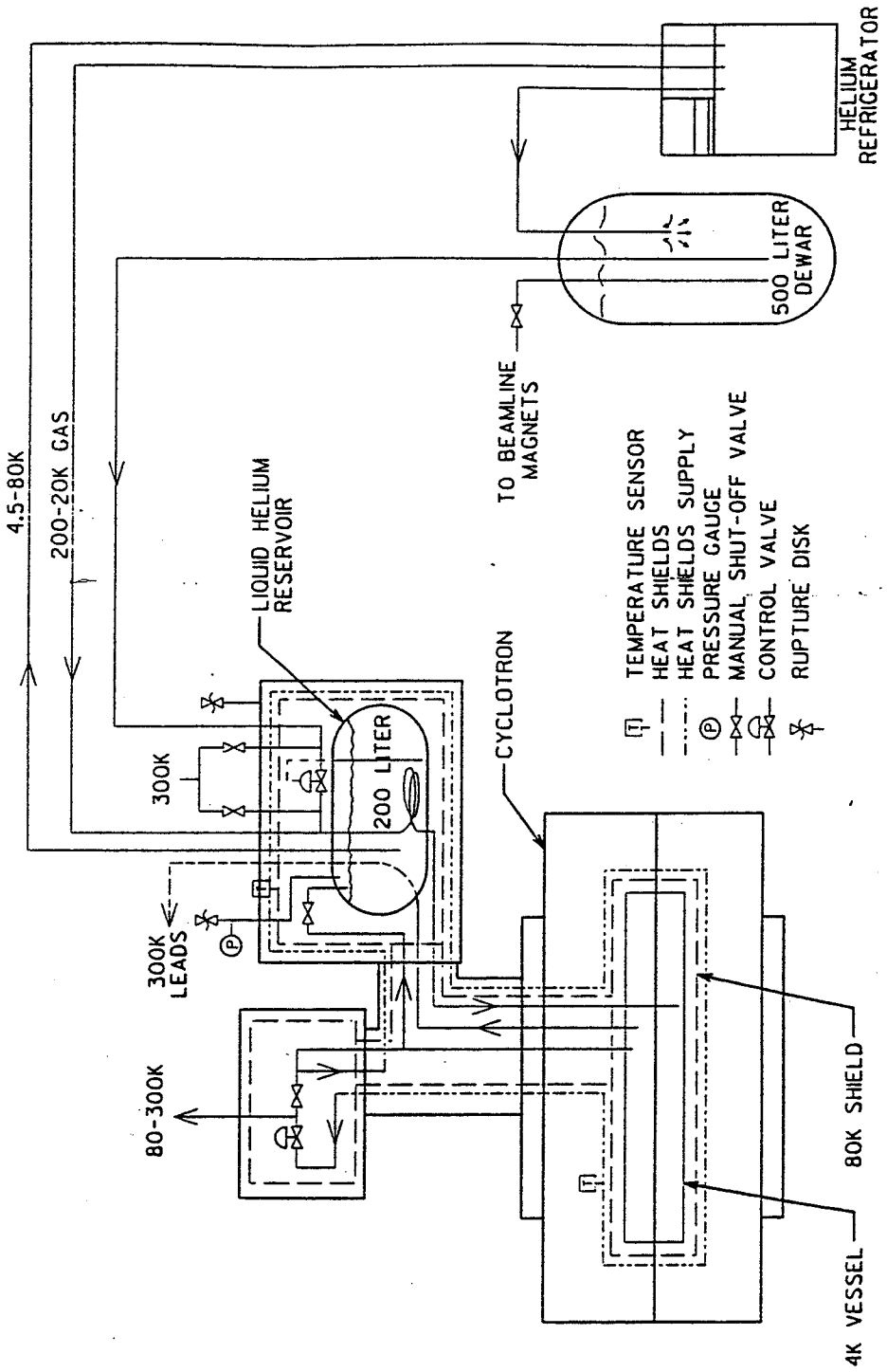

Figure III.23: Schematic drawing of the liquid helium system showing piping details in the 200 liter local reservoir mounted on the cyclotron yoke and the shield cooling interconnect box at the left of the 200 liter reservoir.

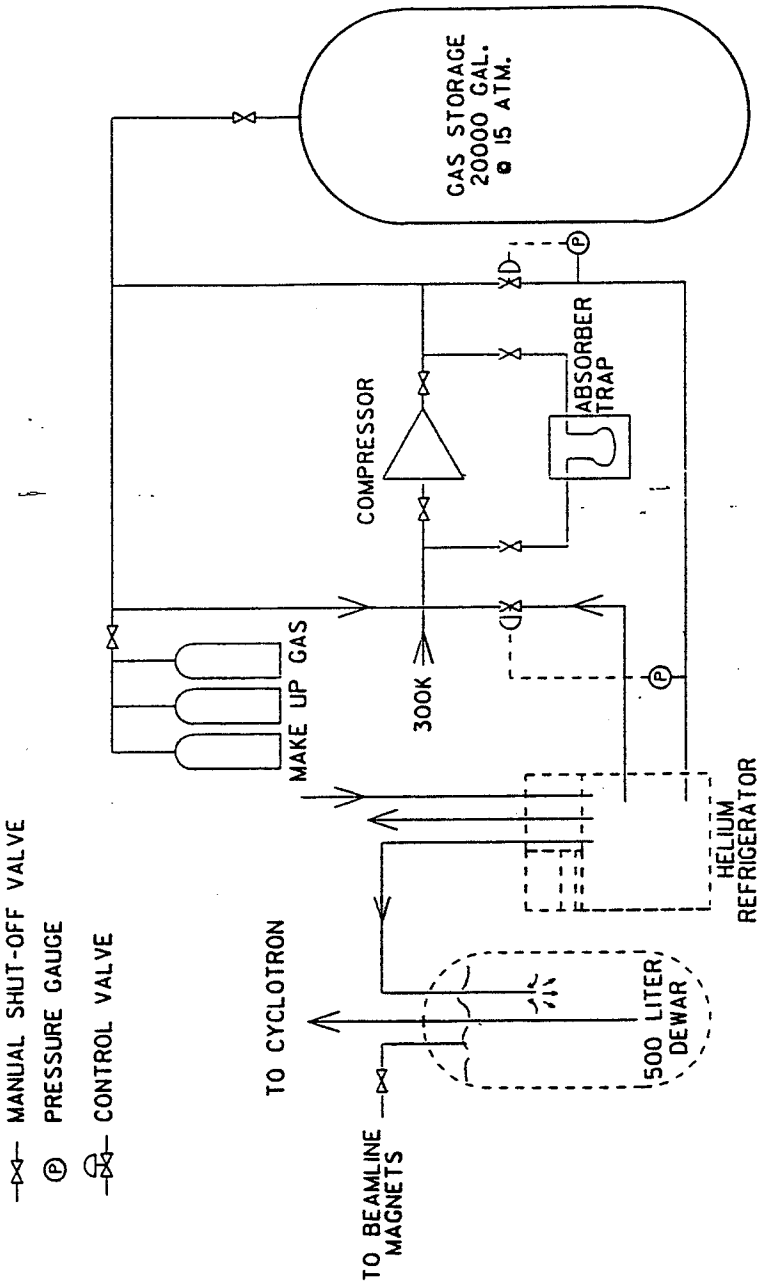

Figure III.24: Schematic drawing of the warm helium storage system and piping including the main compressor and warm gas storage tank.

to a liquid nitrogen cooled shield. (Using liquid nitrogen in a cryogenic facility greatly increases the production capacity of the refrigerator by direct use of liquid nitrogen in the refrigerator, and by nitrogen cooling of heat shields which thereby makes 4K boiloff gas available to be returned to the refrigerator.)

Complete optimization of the liquid helium system will differ from site to site depending on the distance between the refrigerator and the cyclotron, the actual heat load on the complete system, and the degree to which other cryogenic equipment is to be attached to the same refrigerator. The dewar, included as part of the cyclotron, and the 4K valves, provide a versatile ability to adapt to remote refrigerator feed, to close-by refrigerator feed, or to feed from purchased helium dewars. The refrigerator system included in the project cost schedule will provide 25 to 50 liters per hour of liquid helium depending on whether liquid nitrogen is, or is not, used. The refrigerator is a standard model which is in wide commercial use and even though the capacity is considerably higher than will be needed for the cyclotron alone, the next smaller standard model would be border-line in capacity. (A customized intermediate model would be more expensive than the larger standard model.)

The warm helium handling system shown in Fig. III.24 provides a large, 15 atmosphere gas storage vessel adequate to store the full (and valuable) helium inventory during a prolonged shutdown. A special absorber trap can be valved in for recirculation of the gas in the event of accidental contamination of the system. A full purification system provided as part of the helium refrigerator manufacturer's package will be included along with instruments for measuring microscopic impurity levels in the gas stream.

III.3 Radio Frequency Acceleration System

As indicated previously, the 250 MeV proton cyclotron will use a 4 dee, second harmonic acceleration system operating in a pulsed CW mode. Each of the 4 dees will be located in a valley of the magnet as shown in earlier Figures. This dee configuration greatly lowers the capacitive load on the rf system in comparison with the 180 degree dees used in the rf systems of early isochronous cyclotrons and hence the operating power. Effective acceleration gaps in the system proposed are separated spatially by 45 degrees. On second harmonic, this corresponds to 90 rf degrees. The voltage on the gaps at the rf phase corresponding to peak energy gain is then 71% of peak voltage. Taking the nominal dee voltage as 100 kV to ground, the eight gaps give a peak energy-gain-per-turn of 566 kev; approximately 500 turns will therefore be required to reach the peak energy of 250 MeV. The product of turn number and harmonic number, nh, is then approximately 1000 which is somewhat greater, than the nh product of 800 used in the Detroit medical cyclotron (and both numbers are small compared with the nh product of 15,000 used in the TRIUMF cyclotron). The required isochronism will be achieved by adjustments in the iron, since the single main coil leaves no electrically adjustable field shaping parameters. To facilitate fine adjustment of the iron, the magnet design will include a slot in the center of each hill where incremental iron can easily be added or subtracted to quickly achieve the required

field shape in the magnet mapping process.

Principle mechanical features of the rf system are shown in an expanded view in Fig. III.25. Each dee has stems on both top and bottom as in the K500 and K1200 so that top to bottom voltages inside the dees can be nulled by appropriate positioning of the shorts on upper and lower stems. Figure III.26 is a schematic diagram of the complete rf system. East and west dees are galvanically coupled in the central region and thus are forced to be at the same rf phase (see Figs. III.8 and III.9). Power is coupled to one stem of this pair of dees and the other three stems of this pair are preset, using mechanically actuated positioning screws on the shorting planes of each stem to balance the voltage distribution top to bottom and between the two dees. One stem of the four will also be used as the fine tuner to match the resonator to the amplifier – a phase servo compares the rf phase with the phase of the drive power and a motor drive positions the shorting plane to give the correct phase shift, thereby minimizing reflected power and "tuning" the system from the perspective of the rf amplifier.

North and south dees are capacitively coupled to the east/west dees by the central region electrodes and each of these dees can operate in either the 'in-phase',or 'push/push' mode relative to the driving east-west pair, or in the 'opposite-phase' or 'push/pull' mode relative to the east/west driven pair. This coupling configuration was used with great success in the radiofrequency system of the MSU K50 cyclotron. The tuning of the north and south dees selects the desired mode which will be well separated, as indicated quantitatively in a following paragraph, and a final adjustment of this tuning fixes the relative voltage between each of the satellites and the driven east- west pair. A motorized drive on the shorting plane of one of the stems of each satellite dee is servoed to maintain the 'dee balance' (i.e. the voltage on the satellite relative to that on the driven dee) at the required accuracy, again copying the arrangement used with great success on the K50 cyclotron.

Techniques for designing resonators of the type to be used in the proton cyclotron have advanced greatly from the time of the K50, and calculations now typically predict resonant frequencies to a few percent. The important steps of the process are shown in Figures III.27 and III.28. The resonator is first divided into assumed transmission line sections as shown by the dashed lines with alphabetical labels which run across the dee in Figure III.27. Each such section is then modeled as a section of transmission line of length corresponding to the dashed line running along the central spine of the dee in the Figure. Electric equi-potentials of each transmission line section are assumed to be those of an infinitely long line of that cross section and these are calculated numerically with a two dimensional relaxation code.

An example of results from such a calculation is shown in Figure III.28 for one of the transmission line sections. The surface electric fields from the relaxation calculation determine the surface charge, which is also the current distribution on a long uniform line. The surface charge per unit length is used to compute the capacity per unit length and hence the characteristic impedance of the line. Each finite section of line, and similar sections comprising the dee stems, are then placed in a circuit diagram corresponding to

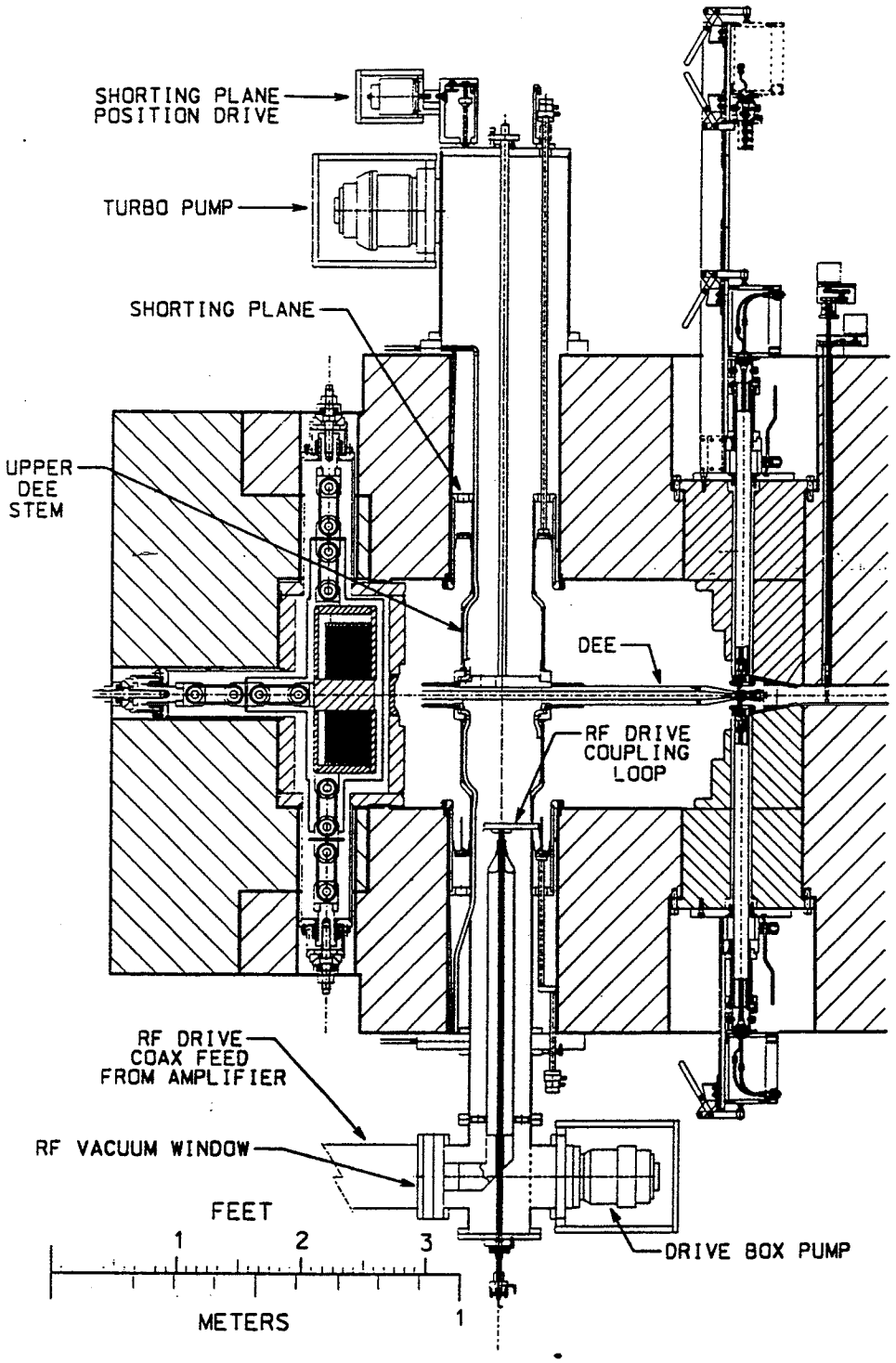

Figure III.25: Expanded vertical section view showing details of the rf drive coupling loop on the lower stem and of a standard stem at the top.

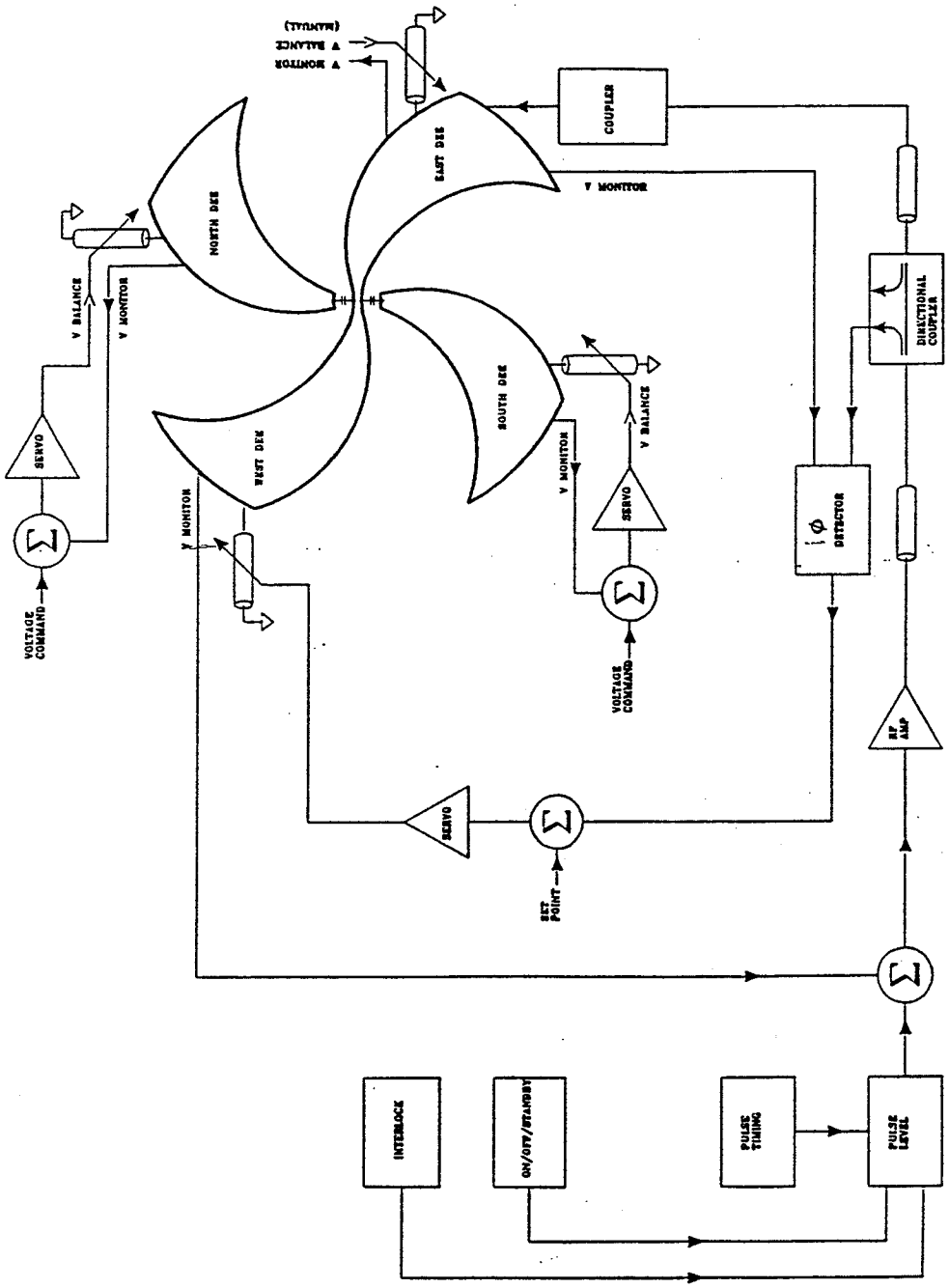

K250 VOLTAGE/PHASE REGULATION BLOCK DIAGRAM

Figure III.26: Schematic diagram of the radio frequency system for the 250 MeV medical cyclotron. The Figure shows details of the rf drive system and of the three servo loops which will tune the resonator to match the 72.4 Mhz drive frequency supplied by the rf amplifier. The voltage balance between satellite dees on the north and south and the driven east/west pair is set by shorting plane servos on the satellite dees.

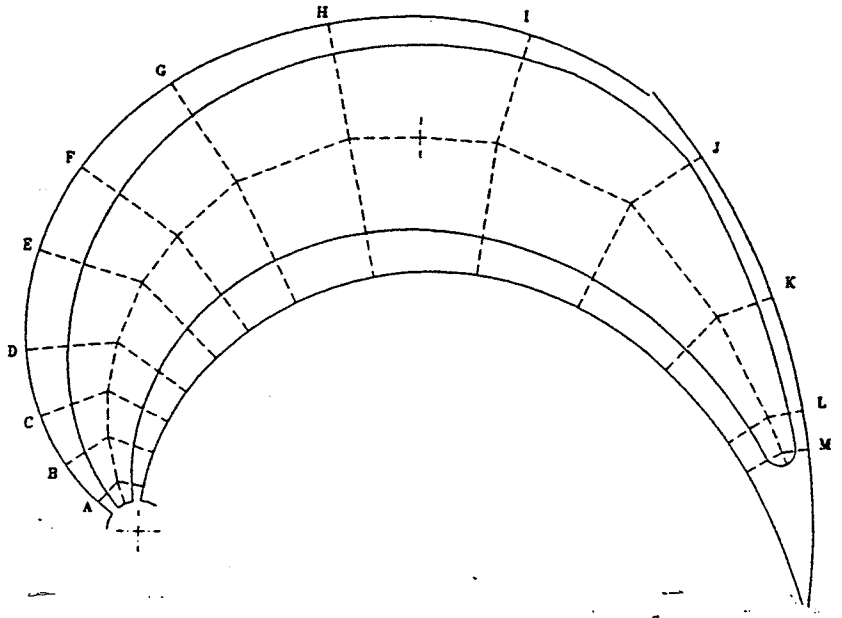

Figure III.27: Plan view of a typical valley and dee with section cuts at the lettered dashed lines denoting points where relaxation calculations of the field distribution were made.

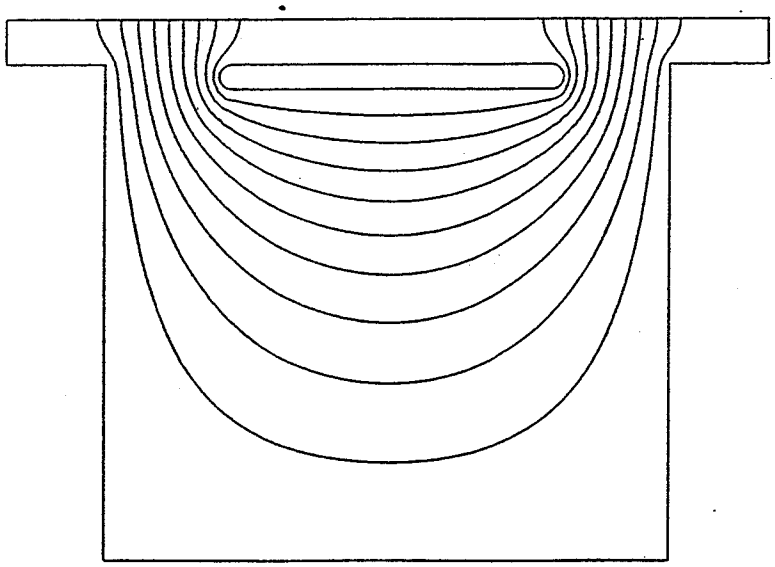

Figure III.28: Calculated equal potential lines at section F of fig. III.27. Perpendicular boundary condition is applied at the medium plane at the top of the figure and dee and liner are set to be equipotential surfaces.

the complete dee, or to the complete resonator, and the array is fed to an AC circuit analysis code which solves for currents and voltages at all element nodes. Capacitive elements in the central region can also be included in the circuit analysis as a lumped element.

Using this model, the dee stem length is adjusted to give the desired resonant frequency, and the currents in each element, together with the current distribution from the relaxation calculation for each section of line, determine the system power. Another feature which the transmission model immediately produces is a prediction of the voltage gradient along the dee. This voltage is different at the entrance and exit point of each dee and Figure III.29 shows these curves for the case calculated here. The lowest dee voltage for both entry and exit occurs at the point nearest the dee stem with higher values at the central region and at the outer tip of the dee.

The effect of changing various tuning elements of the system can also be computed using the circuit model, so that tuning strategies can be evaluated for either individual dees or for the complete system. Figure III.30 shows for example the shift in resonant frequency as the shorting plane on a dee stem is moved in or out; this result shows that resonator tuning can easily be accomplished by a low backlash mechanical drive adjusting the short position (this is also the system used in the Detroit medical cyclotron).

Figure III.31 shows the calculated separation of the push-push and push- pull modes if a North or South satellite is capacitively coupled to the East- West driven pair with 0.5 picofarads. In the push/pull mode the dee-to-dee coupling capacity carries current and is therefore equivalent to an added capacity to ground which lowers the resonant frequency, whereas in the push/push mode, no current flows in the coupling capacitor and so a scan of the drive frequency for such a resonator produces the two modes shown in Fig. III.31. The lower mode corresponds to the push/pull mode, the higher to the push/push mode. The 0.5 picofarad coupling (which is approximately the coupling capacitance which will be provided by the central region electrodes) separates the two modes quite distinctly, making it easy to set the frequency at the value corresponding to the desired mode. (Alternatively, if the frequency is fixed, the cavity can be easily tuned to the resonance corresponding to the desired mode.)

In the K50 and in the Chalk River cyclotron both push/push and push/pull modes were (or are) used for accelerating beams. The appropriate mode was (or is) selected by presetting the resonator to the desired mode and switching the sign of the feedback in the dee balance servo. In the proton therapy cyclotron, only one particle will be accelerated and that will occur on the push/pull mode so the switch to the push/push mode will not be needed.

It should be noted that a problem which occurred with the push/pull mode in the Chalk River cyclotron, namely high currents flowing across the hills from valley to valley, is a phenomenon associated with the median plane asymmetry of the dee stems in that cyclotron. This difficulty will not occur in the proton therapy cyclotron if the top and bottom dee stems are tuned to give a reasonably nulled top to bottom voltage within the dee. Small currents corresponding to the drive power will of course flow across the hills,

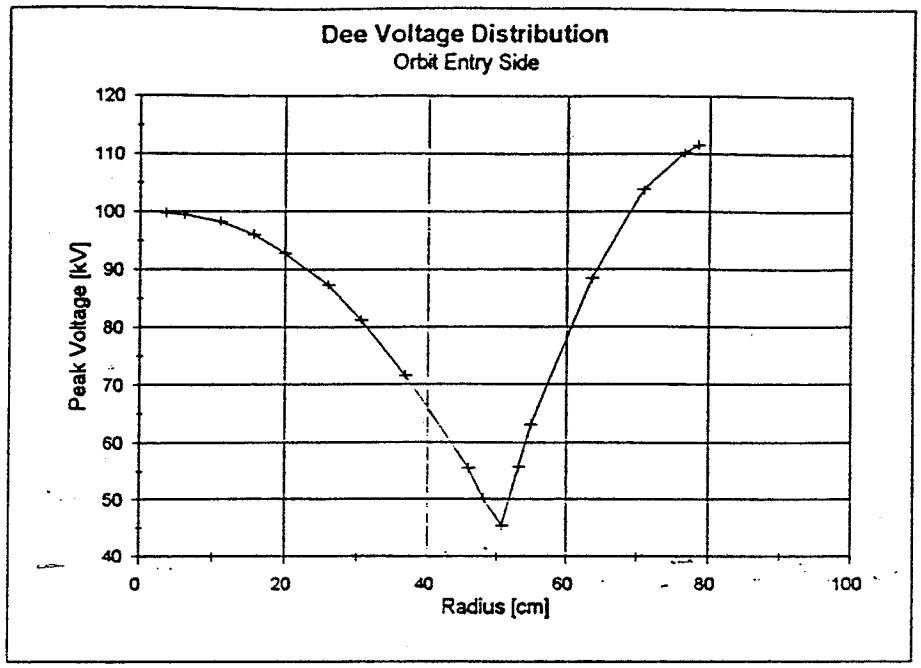

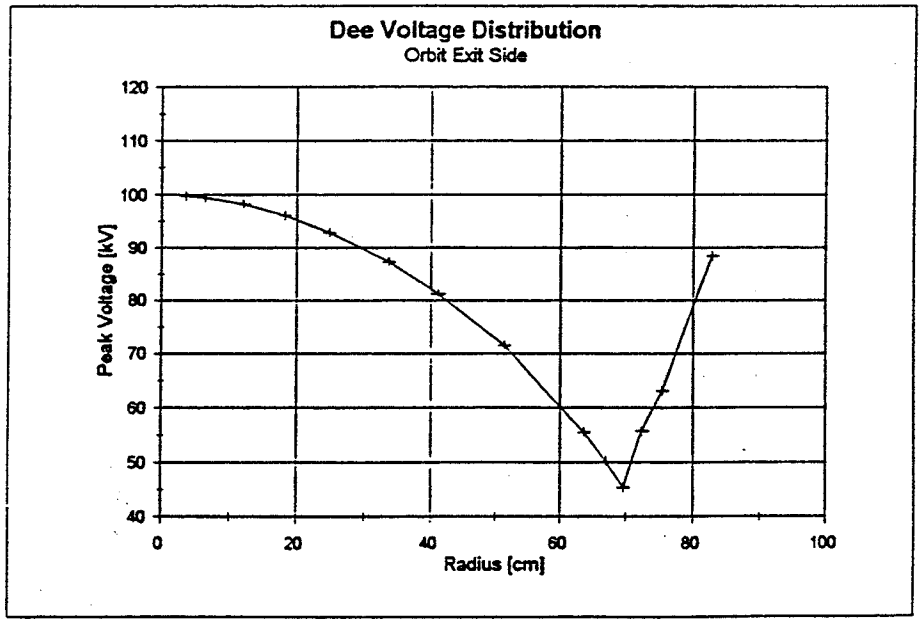

Figure III.29: Calculated voltage distributions at the dee entry and exit plotted vs. radius. The cusp at the minimum voltage point is an artifact of the calculation model which connects the dee stem to the dee at a point. Distributed dee stem connection will give higher minimum voltage and a smooth transition between falling and rising voltage regions.

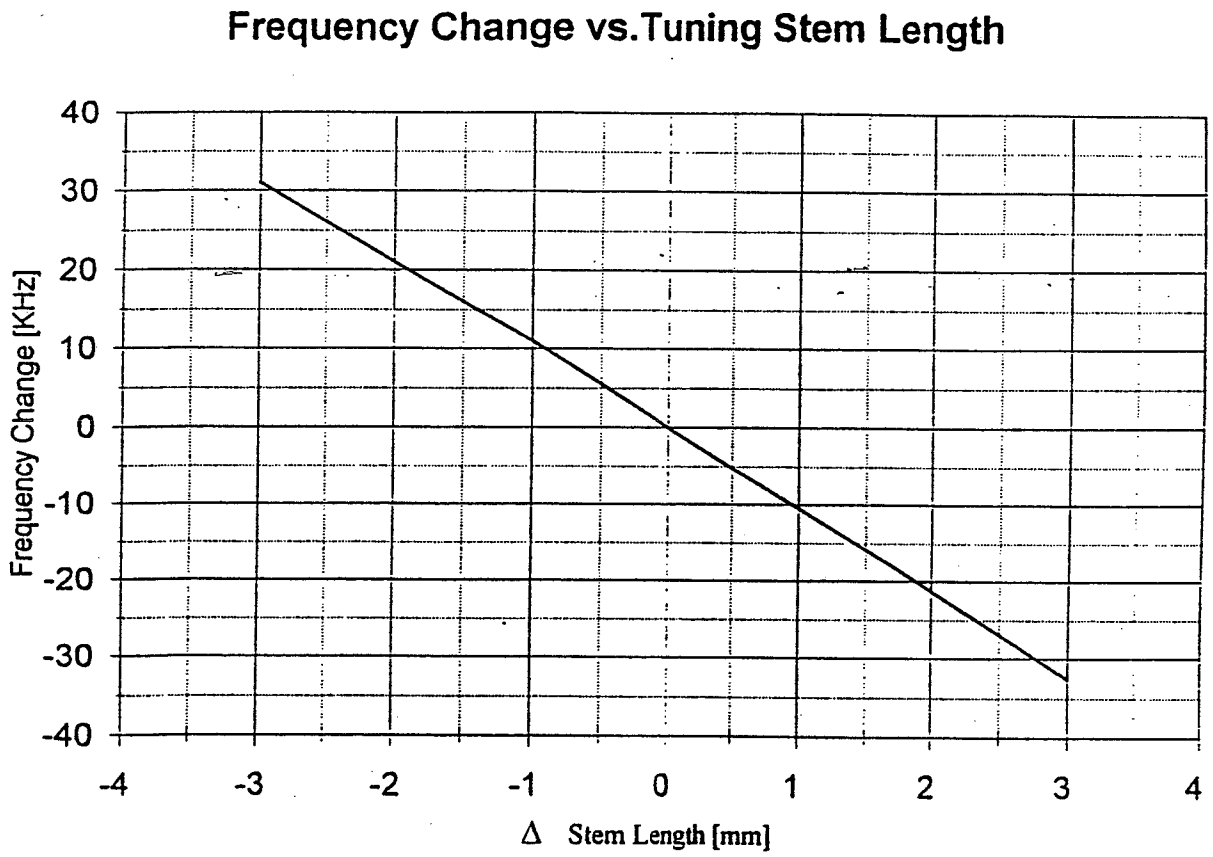

Figure III.30: Illustration of use of the resonator tuning circuit to calculate the dependence of the resonate frequency on the stem length tuning parameter.

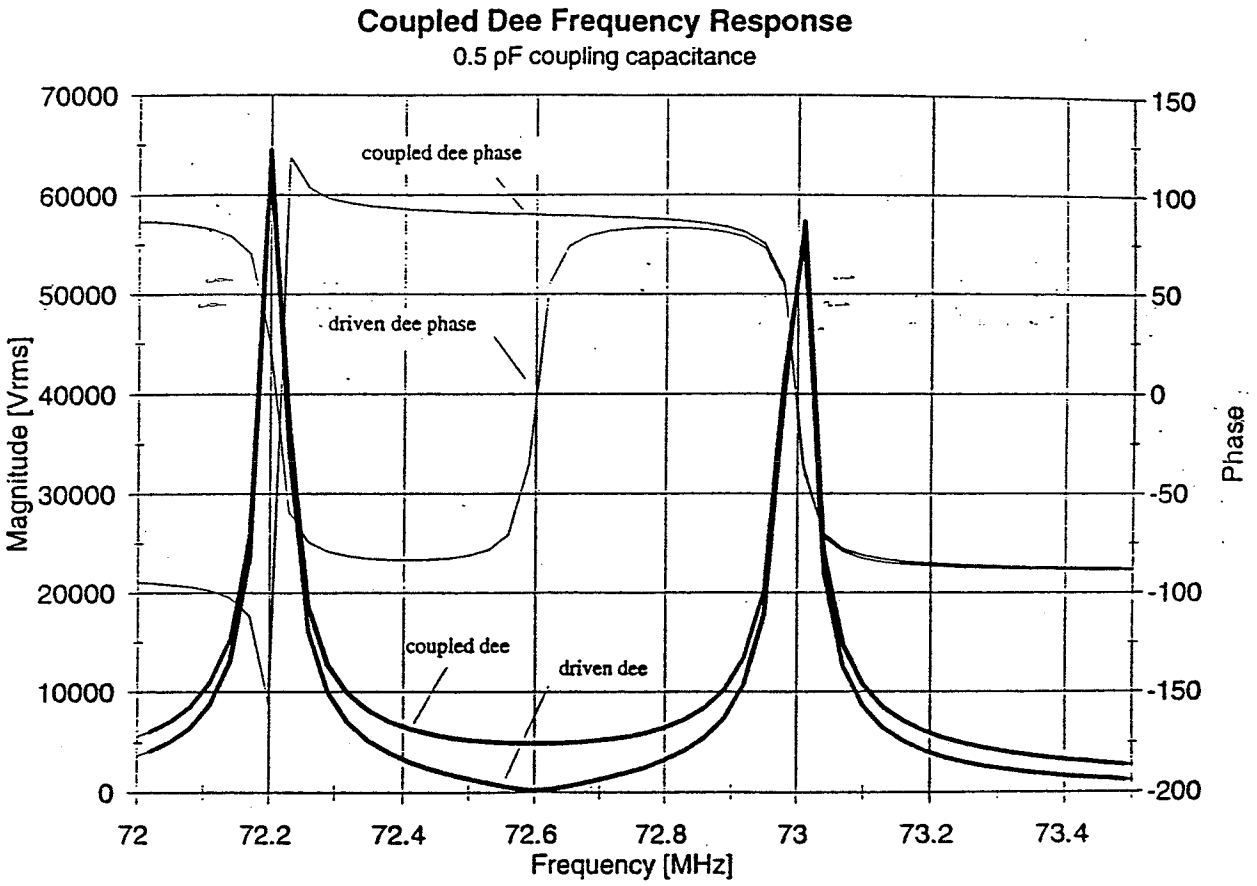

Figure III.31: Response of the complete 4 dee system as the drive frequency is varied from 72 Mhz to 73.5 Mhz, showing push/pull and push/push resonances.

and this will mainly occur near the center of the cyclotron which is the shortest path; appropriate copper covers are provided in the design to carry these currents.

Figure III.32 shows the mechanical layout of the amplifier which will be used to drive the dee system. At this point in the design, a Thompson TH555 tube is assumed as the final stage tetrode since this is the tube in use on the K1200, and tube characteristics are already available in our computer programs. As the proton therapy cyclotron project gets underway, the advantages and disadvantages of other tubes, particularly tubes manufactured in the US, will be carefully checked. (Tubes manufactured in the US will be preferred if reasonably equivalent performance can be obtained.)

The power dissipated in the rf system will be reduced relative to true CW levels by using the pulsed CW technique pioneered in the medical cyclotron in Detroit[32]. In that cyclotron a 2 millisecond 'on', 8 millisecond 'off', pulse pattern reduces the average power to 28% of the full CW level. At this average power, thermal frequency shifts in the resonator are reduced to a level
where operation with servo loops 'off' is easy (and is often used), and system disturbances due to rf sparks are no longer observed. In the proton therapy cyclotron a much lower duty cycle seems desirable, since the slit system which will accomplish the phase selection should transmit currents of approximately 5 microamps at full cw whereas 1 to 10 nanoamps is the current desired for the therapy application (in order to provide adequate time for reaction to unexpected patient movement or other disturbances). At this point 1% has been selected as the likely duty cycle of the system (with 50 hz repetition); much lower duty cycles may well be employed in actual patient treatment situations. The rf power and cooling systems are set up to allow duty cycles up to 10% to be employed, if unforeseen needs for larger currents should develop.

We plan to explore a tuning strategy in which the rf is actually 'on' but at low voltage during the nominal 'off' periods of the pulse with total power in the 'off' period matching total power in the pulse. With this system, turning off the beam between treatments would be accompanied by turning up the 'off' voltage by 40% to maintain the same average total power in the system. This should then maintain thermal effects at a nearly constant level whether beam is 'on' or 'off'.

Table III.2 gives principal numerical parameters of the rf system.

III.4 Other Cyclotron Subsystems

This section briefly reviews characteristics of the more routine subsystems of the proton therapy cyclotron including 1) the beam monitoring system, 2) the vacuum system, 3) the pole cap lifting/lowering system, 4) utilities interconnections and 5) temporary facilities at the testing site in the NSCL Laboratory.

Figure III.33 shows major features of the diagnostic probe which will be provided as a part of the cyclotron. The drive mechanism for this probe is identical to that of one of the probes on the K1200 cyclotron, whereas the beam intercept block, shown at the lower right in the Figure, is specially adapted to the long range of 250 MeV protons. The main

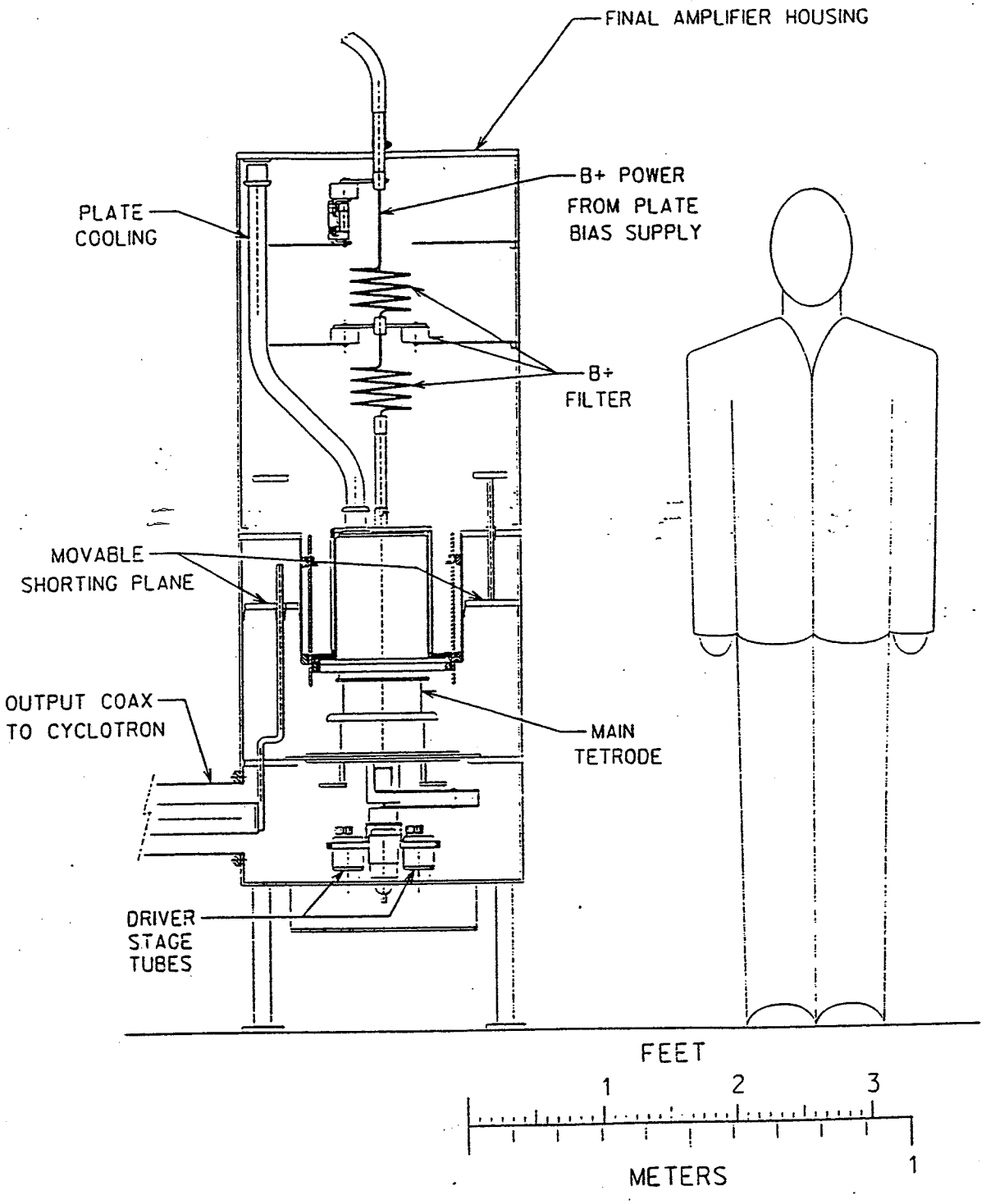

Figure III.32: Schematic layout drawing of the main rf amplifier. The coupling line to the cyclotron exits at the lower left.

Parameter	Value	Units
Frequency	72.4	MHz
Voltage (at injection)	100	kV peaks
Current (at stem short)	1740	A rms
Power Dissipation	152	kW
Q	2730	
Stored Energy	415	MVA
Tuning Stem Length	10	cm
Equivalent shunt circuit(1)		
R	32.9	kOhms
L	26.3	nH
C	180.8	pF

Table III.2: Major parameters of the radio-frequency system for the K250 medical cyclotron. (1) Equivalent circuit measured at injection.

probe head will be tungsten either as a solid block or as a tungsten insert brazed into a copper block, but with tungsten in either case serving as the stopping element for the full energy beam, so that most protons will be stopped in the probe rather than escaping to generate misleading secondaries. The probe will also include a differential wire extending in front of the main probe block to sense current density. The differential wire will be either a fine tungsten wire or a carbon fiber. Such a wire will of course not provide a true current, since the beam will pass through and out, but the wire never-the-less provides a signal proportional to current which can be used to sense turn locations and check centering of the main accelerated beam. In contrast with heavy ions, where the lifetime of such a wire would be low, the experience of many laboratories with tungsten wire septums leads us to expect an indefinite life for a tungsten wire or carbon filament in this situation.

Figure III.34 shows the system which will be provided to insert or remove the ion source. Anodes in the ion source will occasionally need to be cleaned (monthly or bi-monthly), and it is therefore marginally useful to provide a vacuum lock; a manually actuated lock system has therefore been included in the design. The Figure shows the source in both fully inserted and fully withdrawn positions.

Figure III.35 shows the network of jacks which will be used to raise the upper pole or lower the lower pole. Each jack has a 20 ton load rating and an electric motor is included to drive the system. A 4 to 1 ratio of jack lifting capacity to pole cap weight is provided since the jack screws also serve as the support column for the cap when it is in the raised position. The system is modeled on systems in use on other MSU cyclotrons except that 4 jacks are used rather than 3 in order to maintain the basic 4 sector symmetry

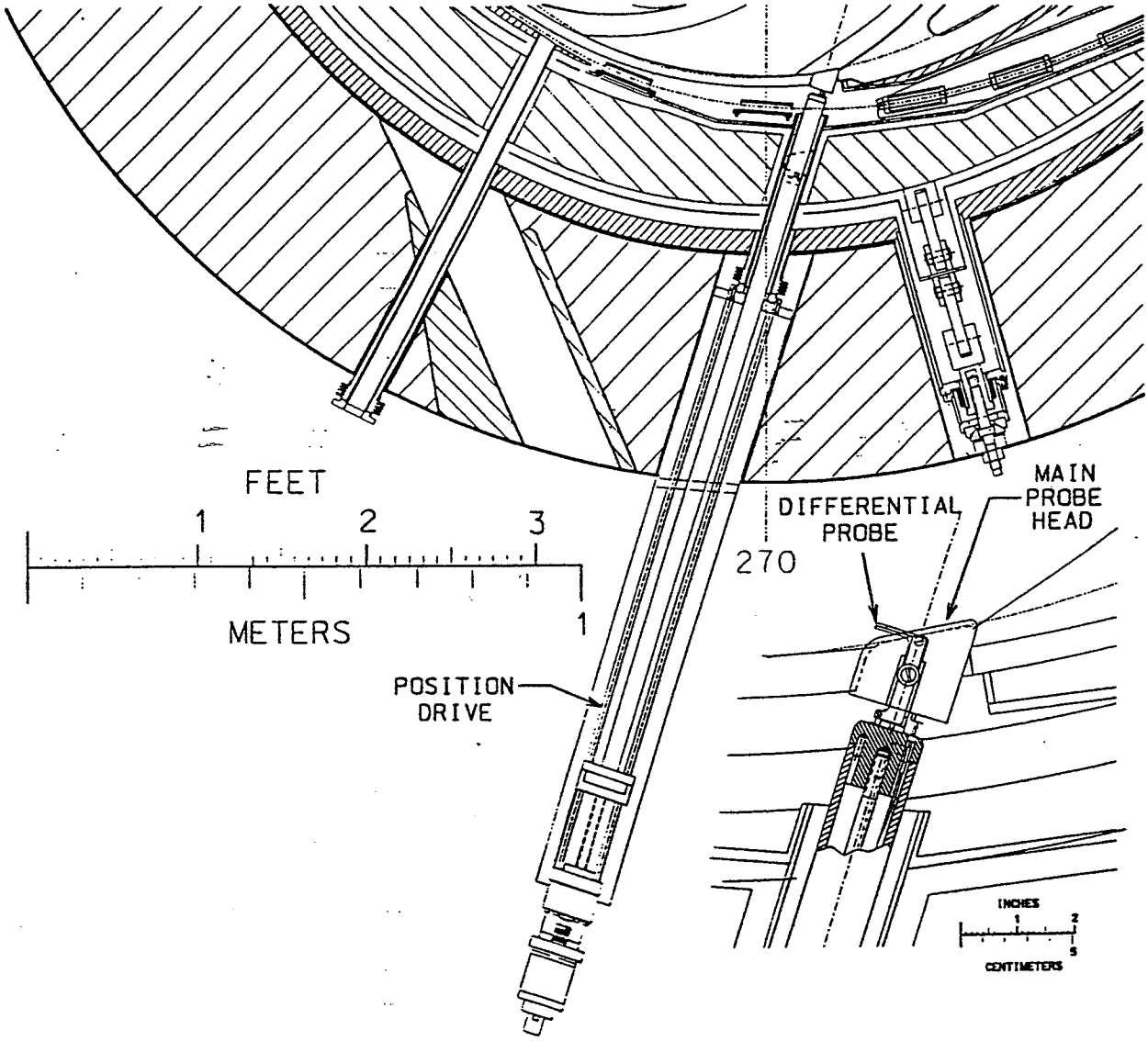

Figure III.33: Mechanical drawing of the diagnostic probe showing the drive motor and screw system which moves the probe in radius (copied from K1200 cyclotron) and, in the insert at lower right, details of the probe head. The beam stopping element will be tungsten in order to provide needed gm/cm^2 of material needed for stopping 250 MeV protons within the available space.

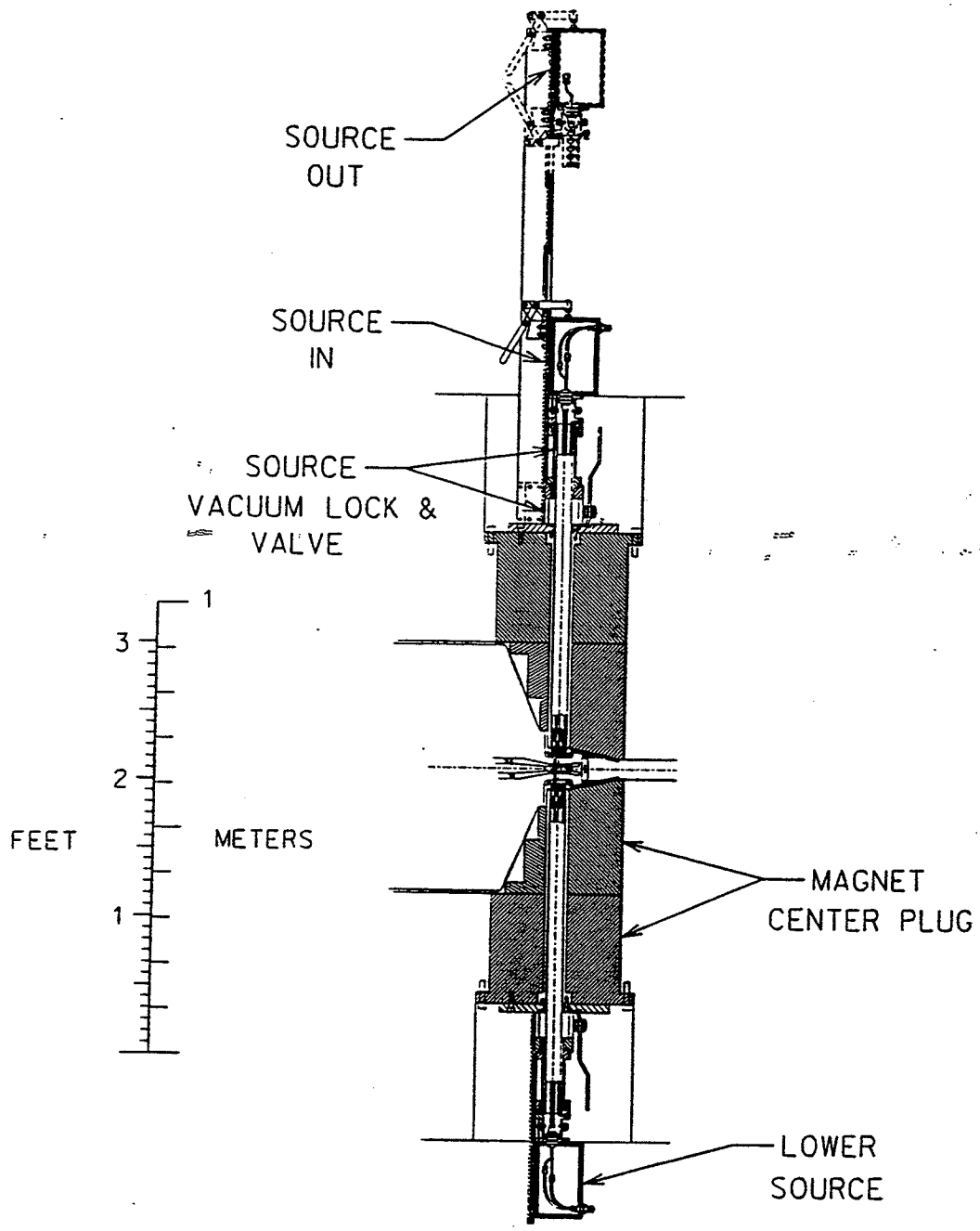

Figure III.34: Expanded section view of the ion source system. Mirror image cathode/anode assemblies insert from top and bottom of the magnet. The source chimney mounts on the upper anode and mates with a matching recess on the lower anode (as shown in Figure III.8). Vacuum locks provide for source servicing without disturbing main accelerator vacuum.

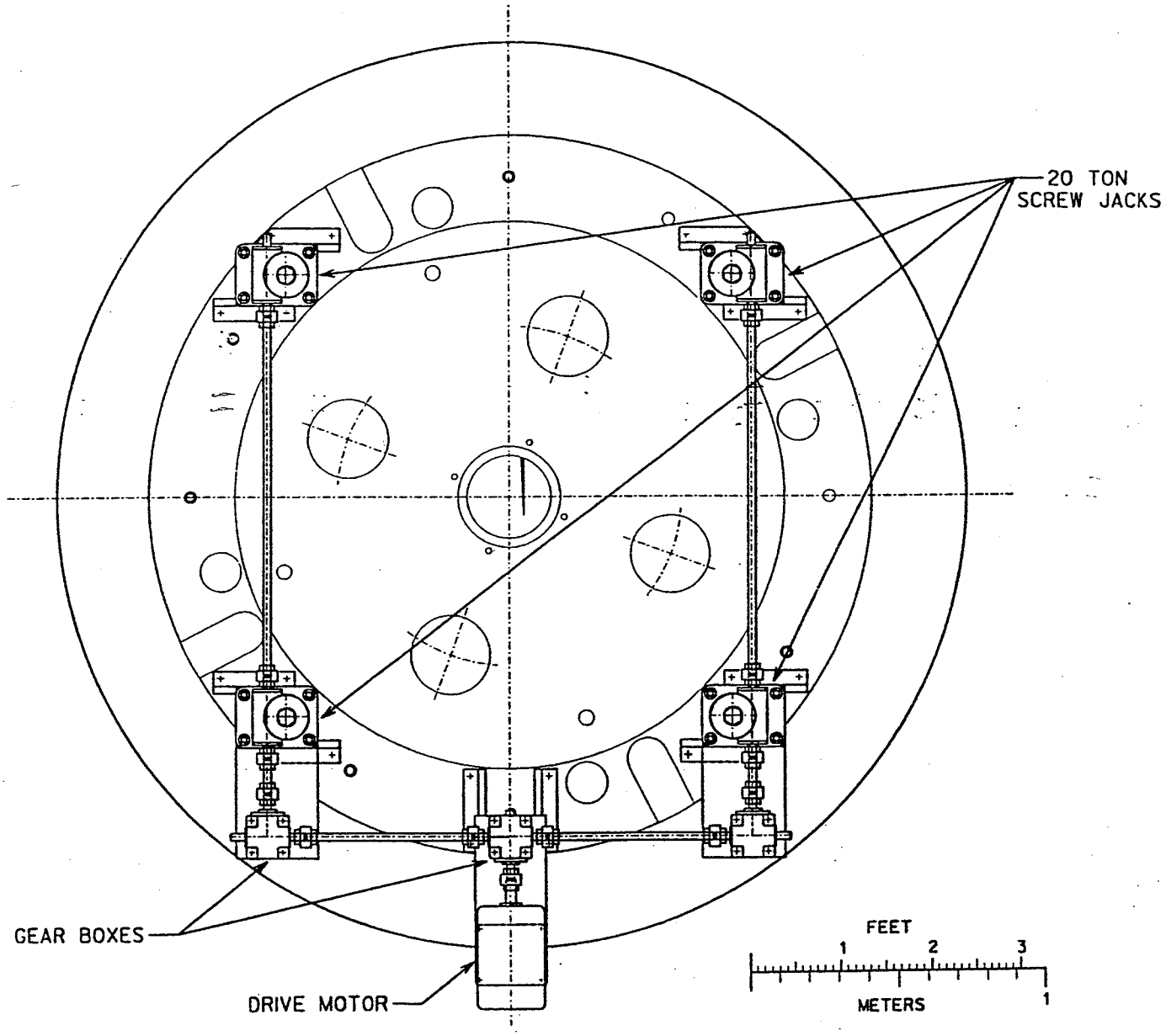

Figure III.35: Plan view of the system of screw jacks which will raise and lower the upper and lower magnet caps to provide access to internal components of the cyclotron.

of the cyclotron magnet. Four jacks can misshare the load and work against each other; the system will be carefully adjusted as it is installed in order to assure that the load is appropriately shared. Strain gauges on each jack screw will be provided to ascertain that this has been adequately achieved.

Figure III.36 is schematic drawing of the vacuum system for the cyclotron. As in other superconducting cyclotrons, the superconducting coil is housed in a completely separate insulation vacuum so that the coil can remain at cryogenic temperatures even when the beam chamber is opened. This is an important operating feature since cooling or warming the coil takes approximately one week, whereas operations which require access to the beam changer are typically a few minutes to a few hours in length. The system should pump to operating vacuum and be operable in a few hours after a tank opening, which would not be the case if the coil was in the same vacuum envelope. The vacuum system is based on turbo pumps which are more expensive than oil diffusion pumps, but which have the advantage of providing a very clean pumping system. The easiest pumping access is through the dee stem holes at the top and bottom of the magnet. The system of mounting an individual pump on each dee stem is approximately comparable in cost to a system of manifolding stems together and connecting to a smaller number of larger pumps, and has the advantage of almost certain ability to operate with one or two pumps not in service.

Each pumping station is a standard vacuum configuration expect that gate valves are not provided between the beam chamber and the turbo pumps. If a turbo should drop off during a cyclotron operating period, the foreline valve on that station will close so that cyclotron operation should be undisturbed. Since most medical facilities do not operate in the evening hours, a pump which is out of service could be removed by breaking the vacuum at the end of a working day, installing a blank off flange, and resuming pumping so that the system would again be in a functional configuration on the following morning.

The operating vacuum which will actually be required is somewhat uncertain, and, for the prototype cyclotron, we have elected to err on the conservative side by providing a pump on every dee stem. Operation of the Detroit cyclotron, and of proton beams in the earlier K50, is/was very insensitive to vacuum and a part of the testing program for the prototype cyclotron will consist of valving off successive turbos to determine how many pumps are really needed. Future copies of the cyclotron can then use an optimized, possibly less costly, system.

Utilities are included in the prototype project to the point of normally available systems in a standard hospital. This includes the electrical equipment to the point where the unit would connect to a disconnect switch on a normal building primary system, and a low-conductivity water system to the point where it would connect to a normal building chilled water system, or to a process water system in the case of the refrigeration system compressor. Cost of utilities equipment to the point of these interfaces with standard building systems is included in project cost schedule.

Our tentative plan for testing the prototype superconducting cyclotron is to locate the unit in vault 'N4' of the NSCL building, as shown in Figures III.37 and III.38. The

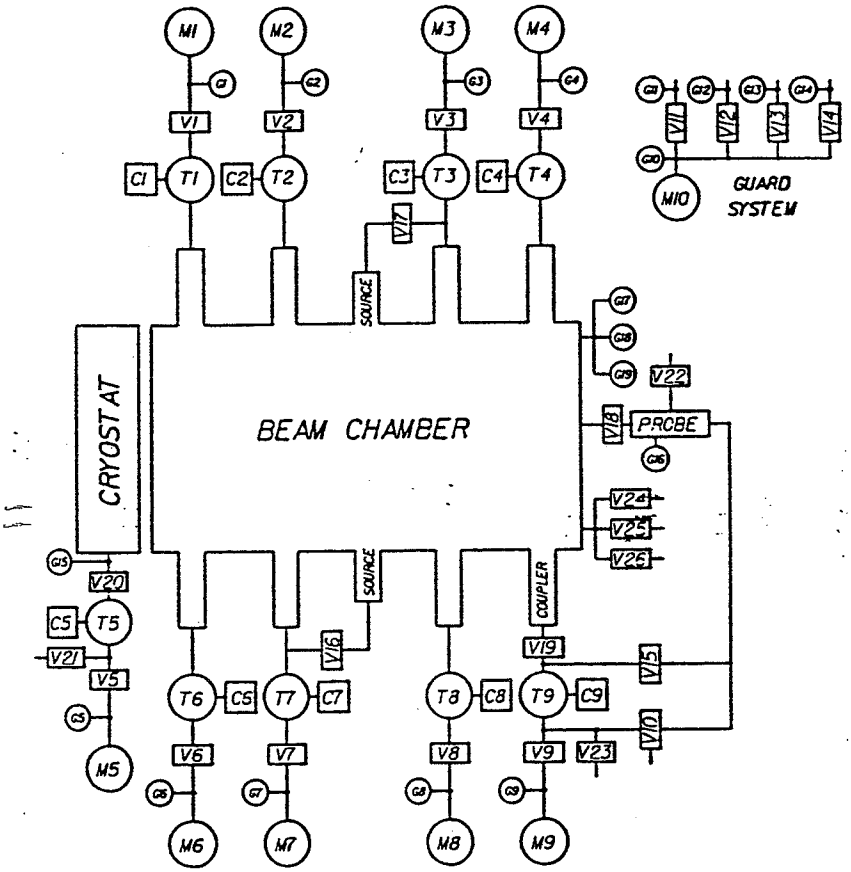

KEY

M1-M10.....MECH. PUMP 7CFM	G19.....MANOMETER
T1-T4,T6-T8....TURBO PUMP 400L/S	V1-V14....VALVE, 1 INCH
T5,T9.....TURBO PUMP 140L/S	V15-V17...VALVE, 2 INCH
C1-C9.....TURBO CONTROL	V18-V20...GATE VALVE
G1-G14,G16,G18.THERMOCOUPLE GAUGE	V21-V26...VALVE, 1/4-1/2 INCH
G15-G17.....IONIZATION GAUGE	

Figure III.36: Schematic drawing of the vacuum system for the 250 MeV proton therapy cyclotron. The main beam chamber will be pumped by seven 400 liter/second turbos and one 140 liter/second turbo. The main coil cryostat is separately pumped by a 140 liter/second turbo and is equipped with a gate valve to close the pumping connection automatically in the event of a power failure.

N4 vault is presently occupied by a large superconducting solenoid as is shown in Figure III.38, but there is room for both the cyclotron and the solenoid. The two devices could in fact share this space rather comfortably were it not for the sensitivity of the unshielded solenoid to large masses of iron. Possibly the effect of this iron mass can be compensated by placing an off-setting smaller iron mass closer to the solenoid on the opposite side. This possibility will be evaluated in detail as the time for operating tests approaches and compared with a scheduling option in which the cyclotron is installed in the vault for a relatively short period (4 to 6 months) for operating tests and not scheduling operation of the solenoid during this period. Initial assembly of the cyclotron, mapping of the cyclotron's magnetic field, and initial rf testing would take place in an unshielded section of the high bay, after which the cyclotron would be moved into the N4 vault, or some other available vault, for beam testing. Firm planning of the testing site at this far advanced point in time is of course not reasonable. Site preparation will involve no more than one to two months of work and the beam testing site therefore does not need to be fixed until the cyclotron is nearly ready to test, at which time current information as to the likely research needs for various vaults will be available. For the present it is then adequate to exhibit that at least one testing site is available, and to note that several other choices would be workable; the testing site will then be finalized at the time needed based on minimizing the disturbance to the NSCL nuclear experimental program.

III.5 Controls

The proton therapy cyclotron will be computer controlled using a system similar in concept to that used in the Detroit medical cyclotron, but with a more modern computer and with a programmable controller for handling the interlock and power switching aspects of the control system. The number of parameters which need to be controlled or adjusted from the console is relatively small and are listed in Table III.3.

Analog signals from some rapidly changing devices will be hard-wired to control room meters in order to avoid misleading time delays due to the computer control loop reaction time. These include:

- Ion Source Voltage
- Ion Source Current
- 4 Dee Voltage amplitude signals

Signals which will be available for advanced diagnostics in the control room

- rf signals from eight dee stem sampling loops

The Operator Console (OC) will be based on an ISA (Industry Standard Architecture) computer and associated software. Much of the needed software is commercially available including:

- equipment control and status displays

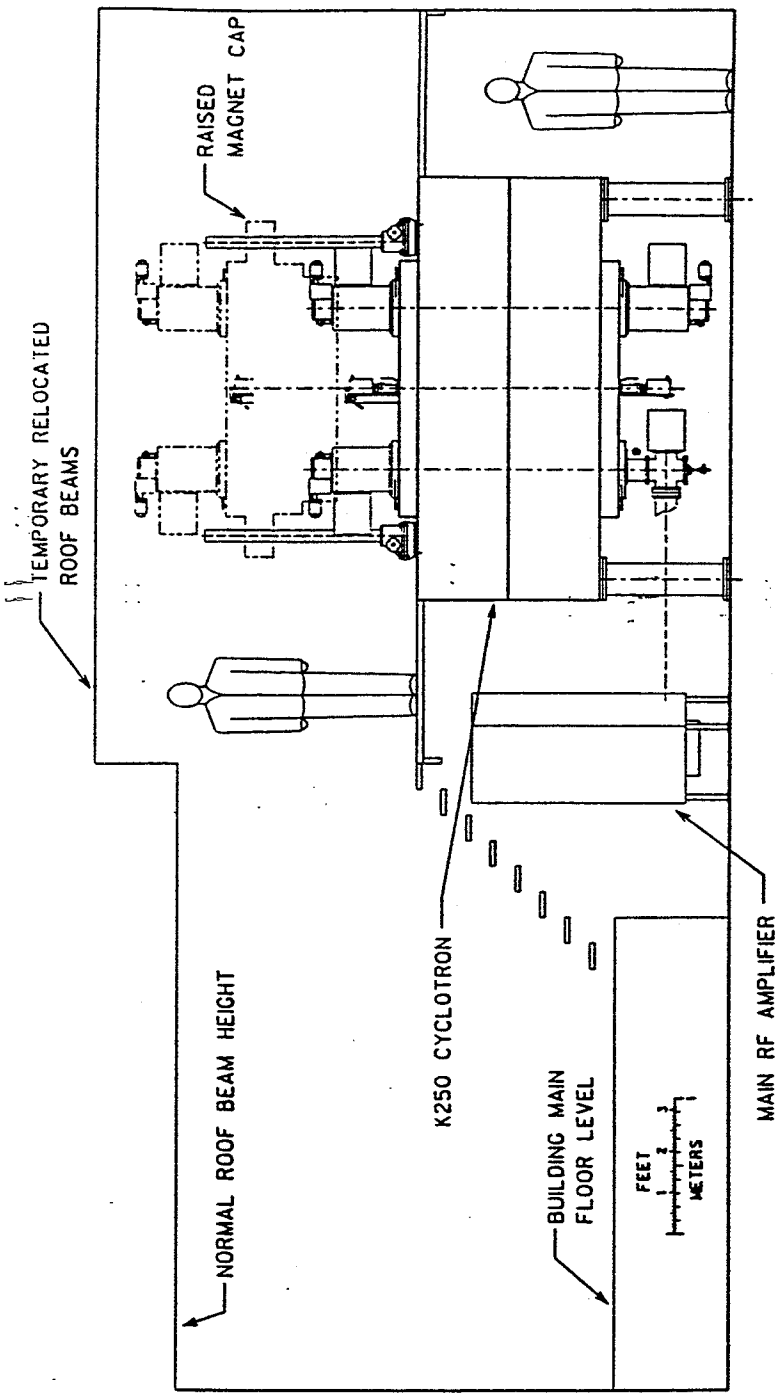

Figure III.37: Vertical section view showing the medical cyclotron set up in one of the possible testing locations in the NSCL 'N4 vault'. Temporary relocation of roof beams, as needed in this location, is a routine process.

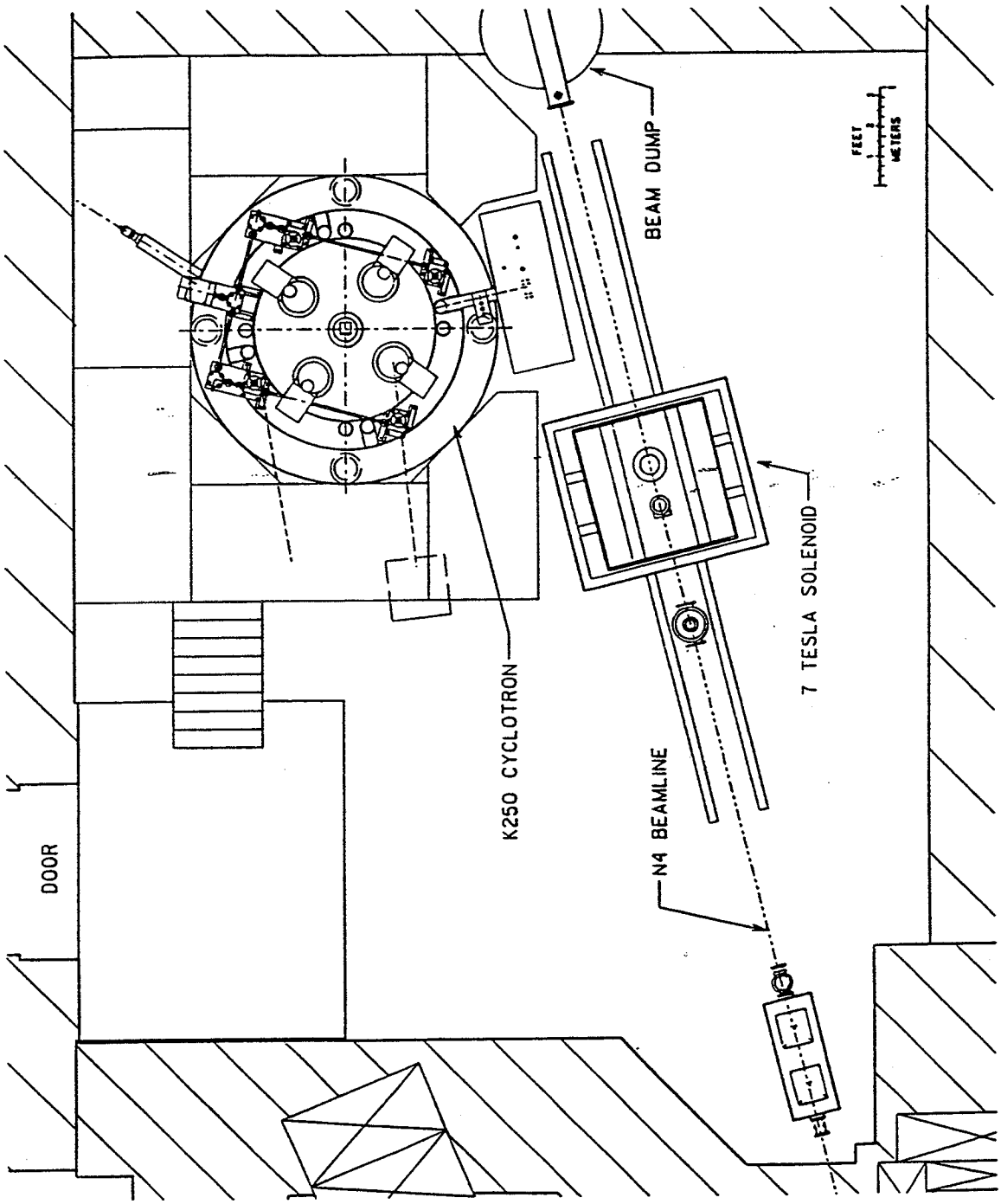

Figure III.38: Plan view showing the 250 MeV medical cyclotron set up in the N4 vault. The beam line to the 7 tesla solenoid is left undisturbed.

Parameter	Monitored	Controlled
Ion Source Voltage	1	
Ion Source Current		1
RF Dee Voltages		4
Electrostatic Deflector Voltages		2
Electrostatic Deflector Currents	2	
Phase Slit positions		4
Centering Coil Currents		2
Extraction Coil Currents		2
Vacuum gauges	2	
Exit Dipole Currents		2
Beam Probe position		1
Beam Probe Currents	2	
Main Coil Current		1
Main Coil Voltage	1	
Main Coil lead voltages	2	
Main Coil level sensor	2	
Dewar level sensor	2	
Main Coil Helium pressure sensor	1	
Main Coil Cryostat vacuum gauge	1	
Temperature sensors	10	

Table III.3: List of elements to be monitored/controlled by the K250 control system.

- chart recorders
- data logging
- probe traces
- automatic
- optimization procedures

State controls (such as on/off Commands to power supplies, open/close commands to valves, etc) and interlock conditions will be handled by an Industry Standard PLC (Programable Logic Controller). The PLC will communicate to the OC via an RS-232 serial data link.

The OC will communicate to a yet to be determined analog I/O controller via some serial data link to acquaire and set continuos quantities. These quatities include servo positioning, probe positioning, magnet current, dee voltage level, ion source arc current level, vacuum levels, etc.

The control system may include several moderately sophisticated subsystems, such as:

- A centering program which would automatically center the beam using data from the differential probe taken over a pre-defined radius interval and adjusting the centering coils to produce a centered beam condition.
- A phase selection program which would insert the phase slits and observe the turn pattern on the differential probe and the time distribution of radiation emitted from the probe. The time distribution would be measured with standard nuclear electronics, processing data picked up from a gamma ray counter located outside the cyclotron. The slits would then be adjusted to optimize the phase selection.

A somewhat simpler program than the two above may also be provided for lining up the beam through the extraction channel of the cyclotron. The need for automated procedures in all these areas is hard to sense in advance, the key unknown being the degree to which the cyclotron beam characteristics reproduce from one operating day to the next. With modern control circuits, and with a one energy cyclotron, it may well be that the operating conditions will reproduce in all aspects from day to day, in which case programming of automated centering, automated phase selection, etc. would not be worthwhile. In this circumstance, optimized operating values for controlled quantities would be initially determined with adhoc equipment assembled for the purpose and thereafter the desired conditions would need only to be reset. In view of this uncertain requirement, work on high-level software is not explicitly included in the project costs estimates at this time. If the operation of the cyclotron shows that such a program will be of effective value, the effort will be accomplished at a later time using contingency funds, and probably as part of a graduate student thesis study.

Chapter V

COST ANALYSIS AND SCHEDULE

The design studies described in Chapter III of this proposal give a thorough conceptual picture of the planned cyclotron. From this picture a list of subsystems has been assembled and a person(s)has been assigned to each subsystem to estimate costs. In this study, procurement is subdivided into the categories, 'standard catalogue items' and 'materials for fabrication'; NSCL manhours are subdivided into four categories, 'design', 'fabrication', 'assembly', and 'startup'. The four manhour categories are defined by the guidelines: 1) design and startup are categories for professional hours, whereas fabrication and assembly are categories for hourly employee hours, 2) design includes all activities which would not have been to be repeated in constructing a second cyclotron, whereas startup includes the activities of professional personnel throughout the project in assisting hourly employees with fabrication, assembly, and debugging of project subsystems, and 3) fabrication and assembly are distinguished by the basic nature of the technical activity in question.

With these definitions, and with the project divided into subsystems according to functional behavior or areas of technical expertise, an overall procurement and manpower estimate was assembled. The cost reports for individual subsystems were then reduced to a one line summary showing the cost and effort in the categories defined above, and these summaries were then assembled into the overall cost summary shown in Table V.1.

In this Table the column heading abbreviations correlate with the cost category definitions given above, and the first entry in each row gives the name of the subsystem. Conversion of manhours to dollars is done at the bottom of the Table using 1) an 18% factor for supervision (the average rate for the Laboratory based on total personnel versus supervisory personnel costs), 2) a factor of 34% for fringe benefits applied to both basic and supervisory charges, and 3) an indirect cost charge on all items except Equipment (or materials to be fabricated into equipment) of 45%. The cumulative effect of these factors is to multiply basic manhour costs by a factor of 2.29274. Basic manhour costs are calculated by dividing the annual salary by the average net hours worked per year by an average employee, i.e. with vacations, holidays, and average sick leave deducted from the 52 times 40 nominal working hours per year. The two columns on the right of Table

1	K250 COSTS /17 FEB 93				MANUFACTURING EFFORT				ITEM	
2	SUBSYSTEM	LEADER(S)	Catalog	Material		Manhours			TOTAL	
3	MECHANICAL ITEMS		k$	k$	design	fabric	assem	startu	k$	
4	Magnet Yoke w/pole tips	Lawton/Hilbert		142.00	200	3,200	500	100	359.23	3
5	Exit Channel & Dipole	Swanson/Zeller	1.00	2.20	360	800	140	100	81.58	13
6	Pole Cap Jacking System	Stork/Snow	17.00	0.60	160	220	120	60	49.19	25
7	rf Liner	Lawton/Bricker		3.90	220	210	120	600	71.20	20
8	Ion Source	Stork	0.48	0.20	180	180	160	40	32.27	32
9	Phase-Slits	Kuchar/Marti	1.50	0.40	250	180	40	20	30.05	34
10	Deflectors	Snow/Antaya	0.30	2.90	500	520	100	180	77.65	15
11	Mag Channels	Stork/Snow		1.65	240	480	70	80	50.58	24
12	Vacuum Pumps	Kuchar/Blue	135.00	3.70	40	80	120	40	154.30	8
13	Beam Probe	Kuchar/Marti	1.52	0.28	230	165	40	10	27.33	36
14	rf amplifier -- mech fabrica	Ottarson/Vincent	2.50	2.50	600	560	280	320	105.79	11
15	Magnet support system	Lawton		5.00	160	60	260		31.89	33
16	Main coil supports	Moskalik/DeKamp		9.70	250	375	160	40	56.01	22
17	Main coil	DeKamp/Wag./Zeller	1.50	68.50	400	1,700	400	250	222.28	6
18	Coil heat shield	DeKamp/Wagner	1.10	6.30	100	200	350	50	46.06	27
19	Cryostat	DeKamp/Wag./Laum.		14.70	140	830	250	40	83.69	12
20	Bump coils & centering coils	Stork		0.40	200	430	60	30	40.66	28
21	Dees & Resonator	Ottarson/Vincent	16.50	36.00	650	940	580	200	185.65	7
22	Central Region & Center Plug	Morris/Marti		2.40	270	860	80	80	74.13	16
23	Cryogenic system	Fontus/Laumer	8.00	16.00	300	50	80	30	50.93	23
24	LCW system	Easley/Hilbert	20.00		70		130	20	32.43	31
25	Steel Plating including Cryo	Hilbert	10.00	17.00	100	500	200	50	73.73	17
26	Field Mapper	Zeller	5.00	10.00	400	200	400	1,200	143.96	9
27	Plumbing	Hilbert	15.00		100	100	400		47.95	26
28	AC Power	Hilbert	30.00		100	60	400		60.80	21
29	He-Liquefier	Laumer	351.90	3.00	40	80	300	40	380.18	2
30										
31	ELECTRONIC ITEMS									
32	Ion Source	Vincent	10.75		160	16	160		29.89	37
33	Centr Cl, Bump, Defl, &Steer	Pwr	20.60				40		22.75	18
34	Magnet	Vincent	18.70		320	56	600		73.34	19
35	Beam Diagnostics	Vincent	6.00				320		23.22	35
36	Interlock Controller & I/O	Vincent	19.40		960		320	20	95.83	10
37	RF Amplifier	Vincent	147.50		800	480	960	200	285.41	5
38	RF Electronics	Vincent	17.00		2,700	160	3,360		369.55	4
39	Control Computer & Console	Antaya	12.00	0.50	560	160	200	240	80.21	29
40										
41	R & D SUPPORT									
42	Accelerator Physics Analysis	Blosser/Marti	0.00	0.00	6,000			1,500	453.15	1
43	Central Region Tests -- K500	Blosser/Vincent	0.00	0.50	300	240	40	60	37.32	30
44	rf Resonator Model	Ottarson/Vinc./Pigee.	0.00	10.00	80	480	560	160	80.47	14
45										
46	Column Totals		870.25	360.33	18,140	14,572	12,300	5,760	4,120.66	
47	NSCL avg salary/year				44.80	39.90	39.90	44.80		
48	work hours/year				1,700	1,700	1,700	1,700		
49	cost				478.04	342.01	288.69	151.79		
50	Manpower subtotal		1,260.54							
51	With Supervison (*1.18)		1,487.43		Second Copy Cost					
52	Fringe Benefits @ 34%		505.73		4367.2	1,281	203	2,883		
53	Indust Partn Com ($15k) + Sal	Mismatch (.5 * $250k)	140.00							
54	Inspection Travel		30.00							
55	Indirect at 45% of above		973.42		Funding -- Year of Expend. k$'s					
56	Procurement		1,230.58		year	93 k$	Inflat	Then Yr		
57	Total estimate		4,367.16		1993	1,200	1	1,200		
58	contingency @10%		436.72		1994	1,850	1.045	1,933		
59		OVERALL TOTAL (93 k$)	4,803.88		1995	1,754	1.08	1,894		
60					Sum then yr k$			5,027		
61										

Table V.1: Spreadsheet showing procurement and manpower estimates for individual K250 subsystems, and, at the bottom, total cost computation and proposed funding schedule.

V.1 give the item total in kilodollars and a numerical ordering of the individual items by dollar value.

After the individual item estimates were complete, the composite summary was reviewed in a meeting of the group of all estimators, so that the overall experience of the full NSCL accelerator staff was focussed on each entry in the Table. After this the summary and all related worksheets were reviewed by Robert Powers of Robert Powers Associates, a firm which has been extensively involved in cost studies for the Department of Energy (including a major role in establishing budgetary figures for the SSC accelerator). A report from Powers Associates is given in Appendix D, along with a brief review of the firm's qualifications. The Powers report supports the estimating procedure used in preparing the Table as well as the overall result.

A general factor to consider in evaluating the probability of significant errors in cost estimates is the probability of unforeseen technical difficulties, since this is usually the main factor leading to significant underestimation of costs. The probability of unforeseen technical difficulties depends most sensitively on the degree to which the project rests on established technology versus requiring development of new technology, or requires skills not previously used by the group undertaking the project. Considering the specific project proposed here – the NSCL has in the past built superconducting cyclotrons both larger and smaller than the one proposed, and these projects, and the earlier K50 cyclotron project, have involved all of the technical elements needed for the proposed K250 cyclotron. This body of directly related experience implies a very low probability of technical difficulties not foreseen in the extensive planning effort which has gone into the K250 design study. This, and the very extensive studies which underlie the cost estimates for individual subsystems, are then the basis for choosing 10% as the contingency level appropriate for this estimate. The report of the cost consultant comments specifically on this judgement, and categorizes the 10% contingency as "fair and appropriate".

As indicated in Chapter IV, $250,000 of salary funds will be made available to the Industrial Partner to pay personnel for hours worked at the NSCL. An effectiveness factor of 0.5 has been assigned to this effort, i.e. the assumption has been made that 50% of the cost of the effort will benefit the project goals with the same efficiency as NSCL effort, and can therefore be considered as covered under the direct estimates for the individual subsystems. The remaining 50% of payments for Industrial Partner services will offset anticipated higher hourly rates for the Industrial Partner's personnel as well as hours which these persons spend in a pupil role, learning about various details of the project rather than directly contributing to progress on the cyclotron. For these reasons $125,000 of the $250,000 is assigned in the budget as an added expenditure not included in the subsystem manufacturing part of Table V.1, and is set up in the budget as an additional special expenditure for the purpose of facilitating a maximumally effective industrial spinoff from the project. This $125,000 plus $15,000 allocated for travel and service reimbursements for the Industrial Partner Selection Committee are then the $140,000 budget item on line 53 of Table V.1.

Table V.2 is a work planning chart showing the work schedule for the project. The

manhour totals from Table V.1 plus supervision add to approximately 37 man years of effort. A principal goal of the schedule plan is to determine whether NSCL staff effort can realistically be assigned to this project at a level such that completion can be achieved in a time frame which will preserve the competitive posture of the project relative to other technologies. From this later perspective, completing the project in three years is a highly desirable project objective. The work plan has been laid out on this basis and manpower levels required to achieve this schedule then flow from the planning program. The results of this study have been carefully reviewed by NSCL project leaders and department heads, and have been accepted and endorsed as a realistically achievable plan, compatible with other ongoing Laboratory programs.

Assuming funding availability on the schedule shown in Table V.1, it is feasible to achieve project goals on the schedule anticipated in Figure V.1, and bring the ensuing benefits to US cancer patients and to the US economy into effect at an early date.

TABLE V.2: K-250 CYCLOTRON - TASK TIMELINE

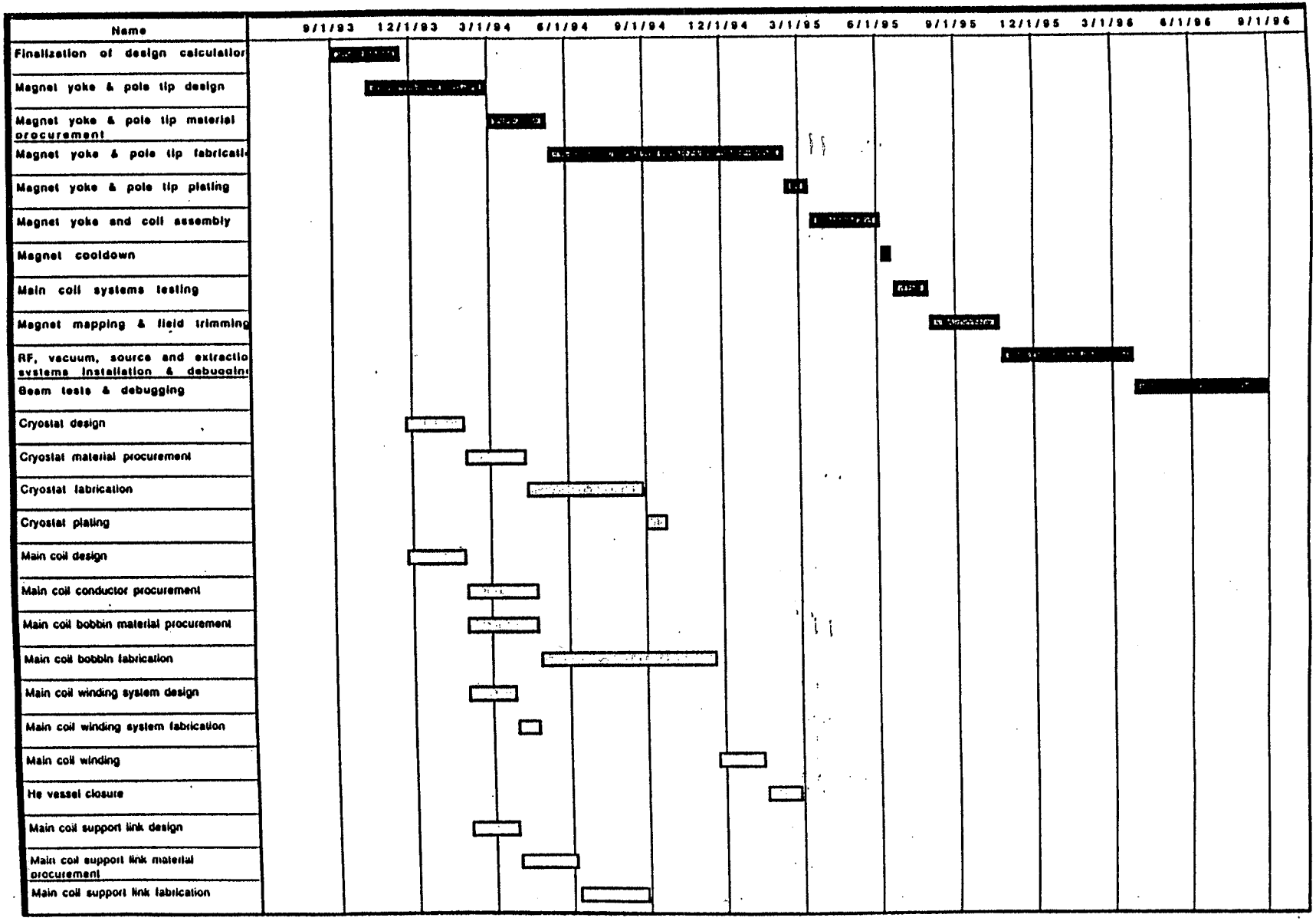

TABLE V.2: K-250 CYCLOTRON - TASK TIMELINE

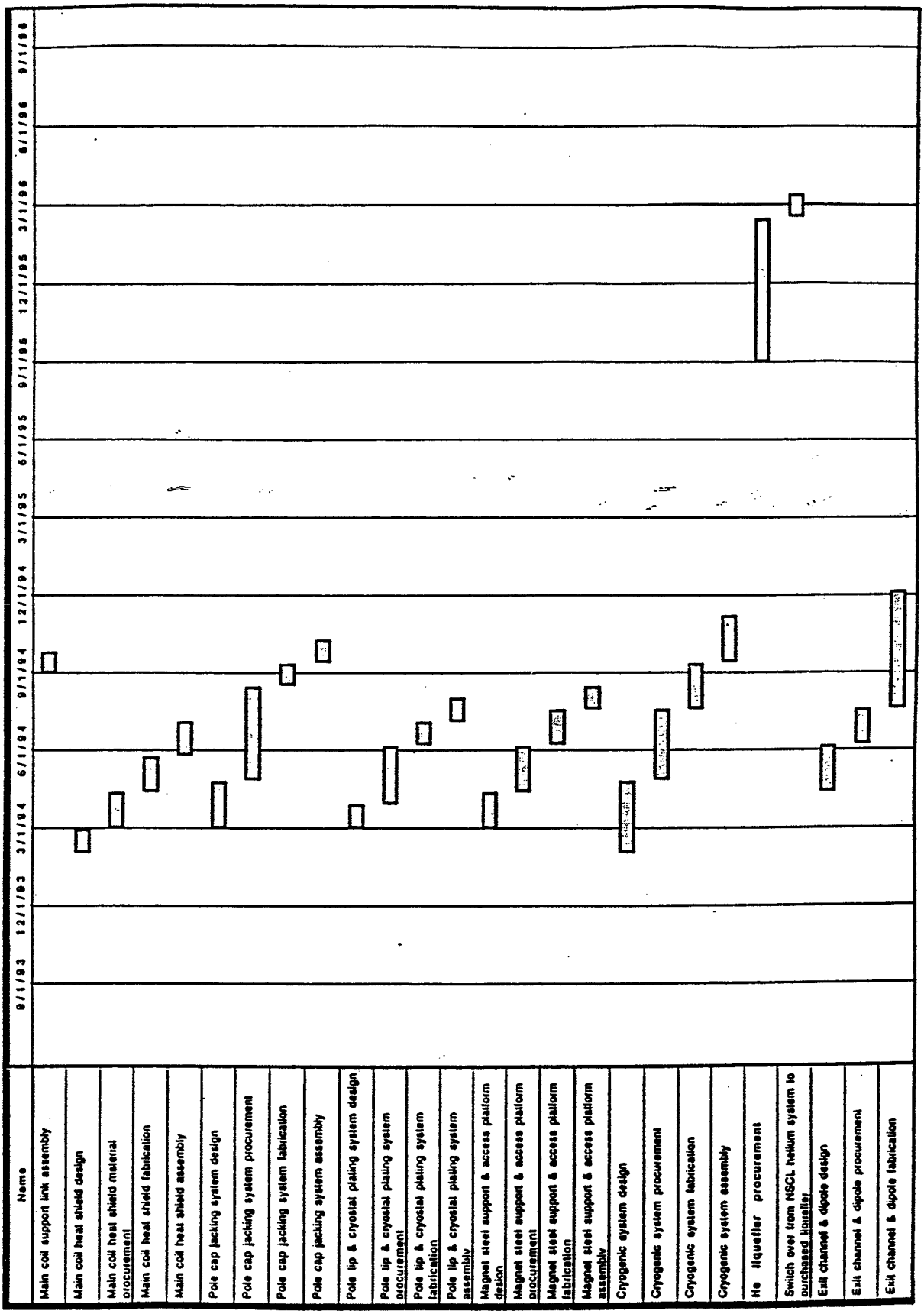

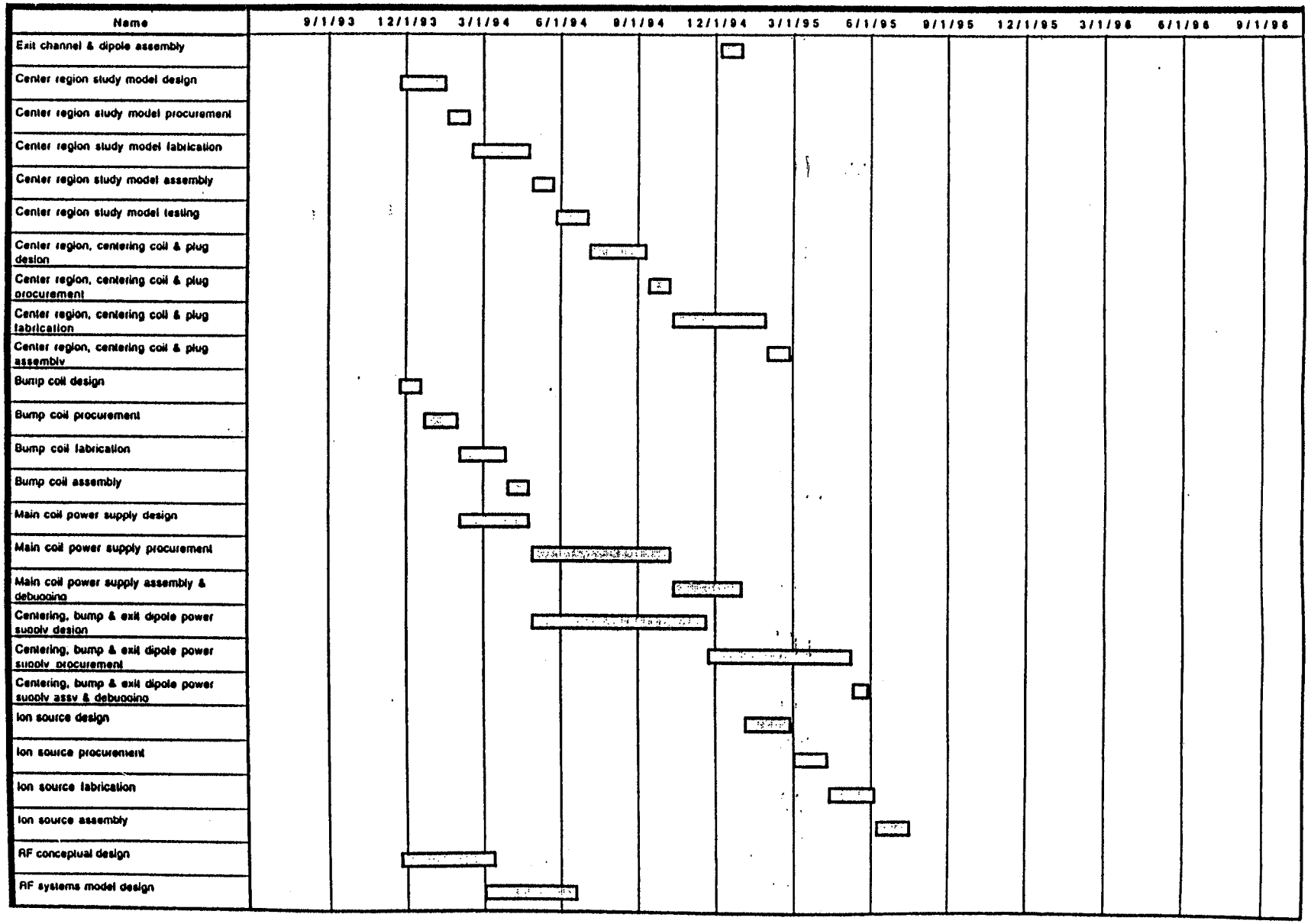
Name
9/1/93
12/1/93
3/1/94
6/1/94
9/1/94
12/1/94
3/1/95
6/1/95
9/1/95
12/1/95
3/1/96
6/1/96
9/1/96
Exit channel & dipole assembly
Center region study model design
Center region study model procurement
Center region study model fabrication
Center region study model assembly
Center region study model testing
Center region, centering coil & plug design
Center region, centering coil & plug procurement
Center region, centering coil & plug fabrication
Center region, centering coil & plug assembly
Bump coil design
Bump coil procurement
Bump coil fabrication
Bump coil assembly
Main coil power supply design
Main coil power supply procurement
Main coil power supply assembly & debugging
Centering, bump & exit dipole power supply design
Centering, bump & exit dipole power supply procurement
Centering, bump & exit dipole power supply assy & debugging
Ion source design
Ion source procurement
Ion source fabrication
Ion source assembly
RF conceptual design
RF systems model design

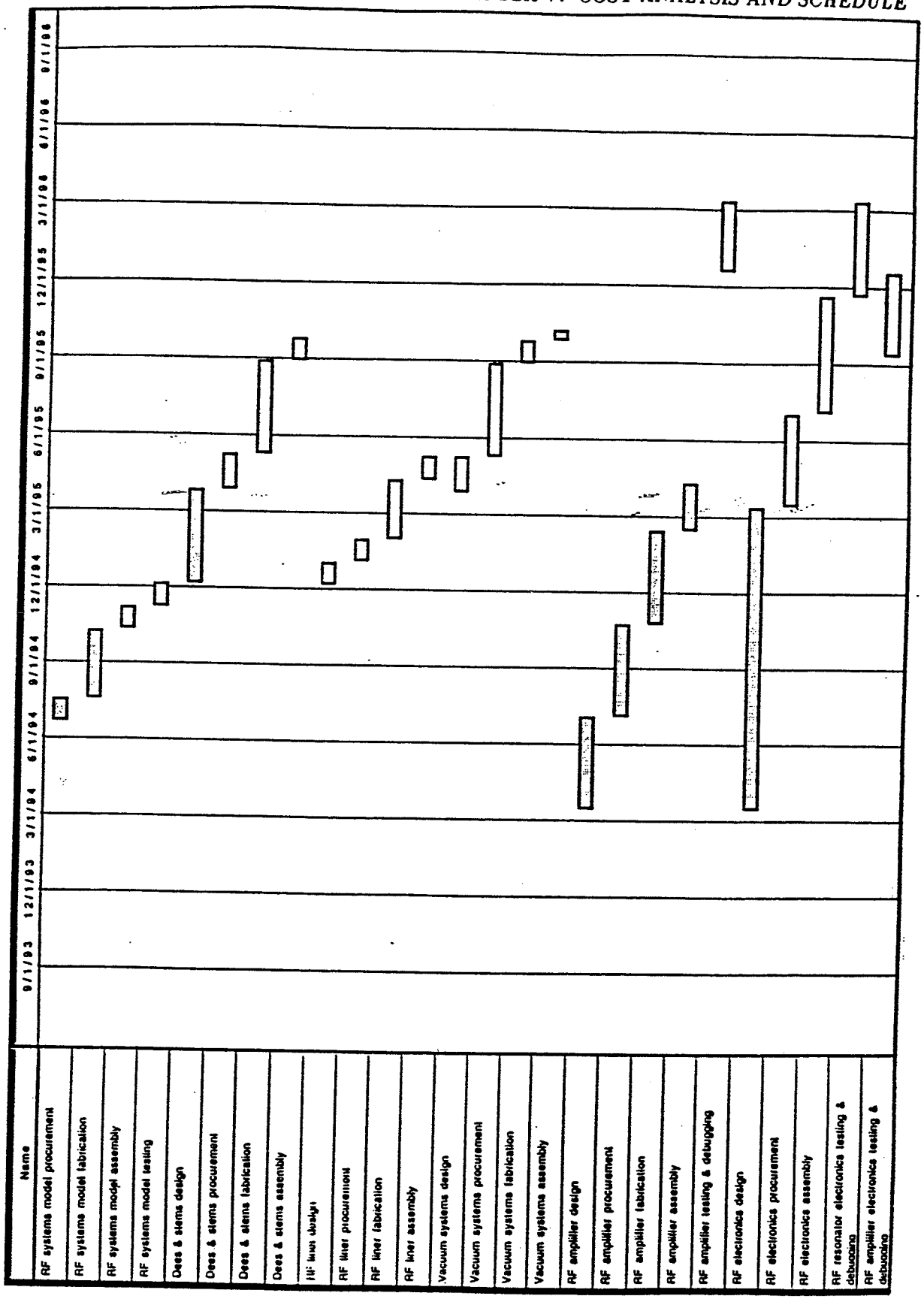

TABLE V.2: K-250 CYCLOTRON - TASK TIMELINE

TABLE V.2: K-250 CYCLOTRON - TASK TIMELINE

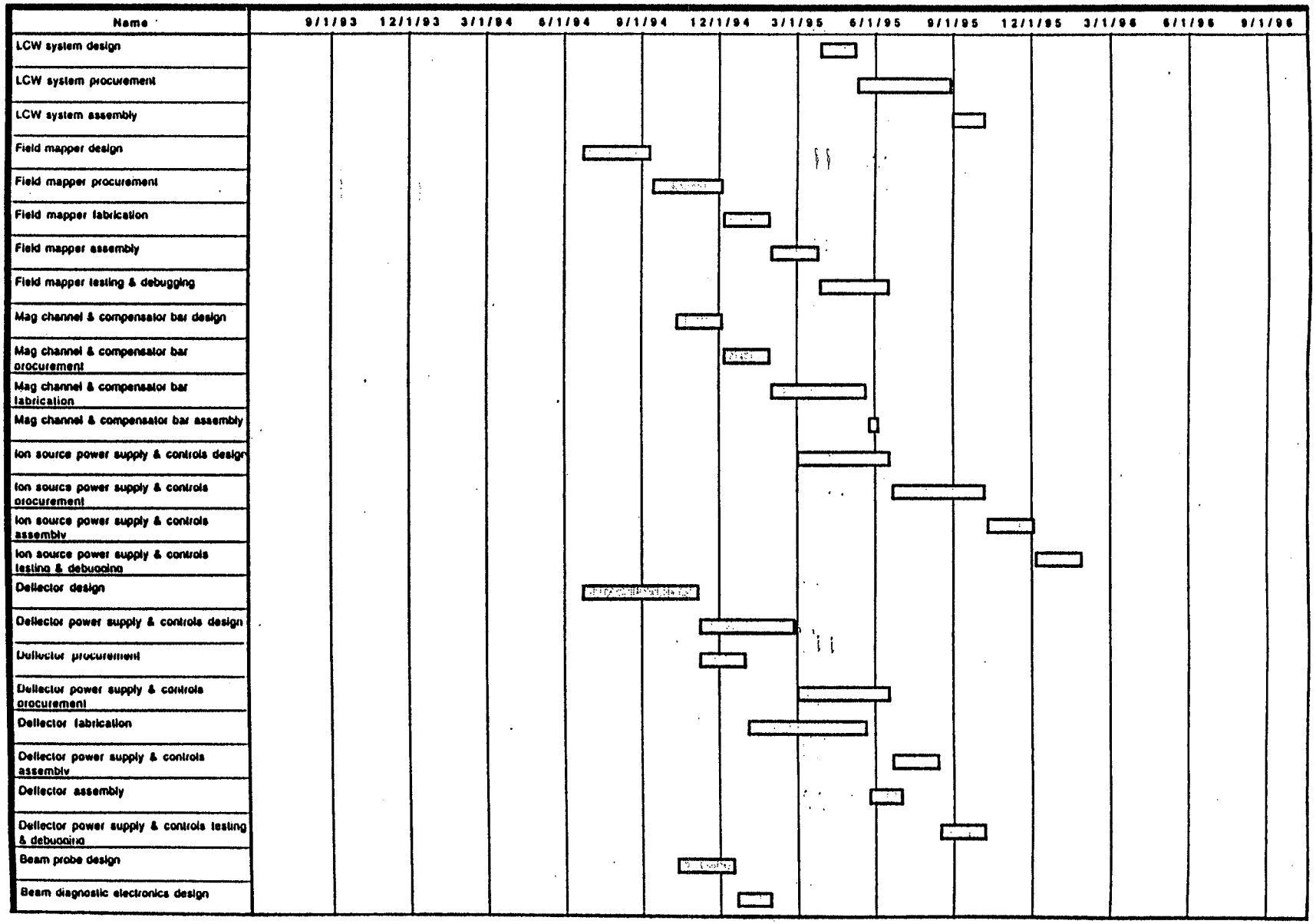

TABLE V.2: K-250 CYCLOTRON - TASK TIMELINE